On-Chip Blood Count

Thesis by

Siyang Zheng

In Partial Fulfillment of the Requirements
for the Degree of

Doctor of Philosophy

California Institute of Technology

Pasadena, California

2007

(Defended May 21, 2007)

To my parents, wife, and daughter

Acknowledgements

There are so many people giving me help and support, which makes this thesis possible and my five years at Caltech an instructive and enjoyable journey.

I would like to thank my advisor, Dr. Yu-Chong Tai, who gave me the opportunity to become a member of Caltech Microfabrication Lab and led me to this wonderful world of micro science and technology. Without his guidance and valuable advice, my goals would not be accomplished in five years. I will always remember his persistence to the underlying fundamental theories, his efficiency for personal time management, and his effective leadership for the lab.

Members of Caltech Micromachining Lab helped me tremendously during my time at Caltech. I would like to thank our lab manager Trevor Roper for his hard work on keeping the cleanroom well functioning. Also Ms. Tanya Owens and Ms. Christine Matsuki provided all administrative support. I am grateful to many previous members of the Caltech Micromachining group: Dr. Yong Xu, Dr. Ellis Meng, Dr. Jun Xie, Dr. Matthieu Liger, Dr. Justin Boland, Dr. Qing He, Mr. Ted Harder, and Dr. Chi-Yuan Shih. They helped me to start my research and taught me numerous lessons from their own experiences. I am also thankful to all the current members in our group: Scott Miserendino, Angela Tooker, Changlin Pang, Damien Rodger, Jason Shih, Quoc “Brandon” Quach, Po-Jiu “PJ” Chen, Nick Lo, Wen Li, and Mike Liu, Ray Huang, Monty Nandra, Luca Giacchino, Chun-Hui “Jeffrey” Lin, Juhwan Yoo, and Young-Hyun “Justin” Kim.

My research is funded by NASA National Space Biomedical Research Institute (NSBRI) through NCC 9-58. I'd like to thank my collaborators of the on-chip blood count project. The progress of the project wouldn't have gone so smoothly without the knowledge and guidance from Dr. Harvey Kasdan, the chief scientist from Iris Diagnostics, Inc. The efforts of Prof. Chih-Ming Ho, Nancy Li, and Charlotte Kwong from UCLA were indispensable for the success of the project.

I would like to thank my Ph.D. candidacy and defense committee members: Prof. Demetri Psaltis, Prof. Changhuei Yang, Prof. Morteza Gharib at Caltech and Dr. Harvey Kasdan from Iris Diagnostics Inc., for their insightful guidance and suggestions on my Ph.D. research.

Finally I would like to express my deepest thanks for my family and dedicate this thesis to them. My parents have motivated my interests in science and technology since I was a kid. They shared their dream with me, provided me with the best resources they could with a lot of their personal sacrifices, and never lost faith in me during my hard times. Their love will always be the best treasure in my life. Also the deepest thanks and appreciation goes to my wife, Ming, who takes cares of me and shares my joy and pain everyday. Without her unconditional support and hard work, I couldn't achieve my goals. The birth of our daughter, Claire, gave us a lot of extra work, but also a lot of laughter and enjoyable moments. I also would like to thank my parents-in-law who helped us taking care of the baby, and my uncle and aunt, who took care of me during my first two years in the US and persistently supported me in later years.

Abstract

On-Chip Blood Count

Thesis by

Siyang Zheng

Doctor of Philosophy in Electrical Engineering

California Institute of Technology

Blood count is one of the most common medical laboratory tests performed today. It provides information on patient's oxygen carrying capacity, immune system functionality, and the overall hemapoiesis process for disease diagnosis and drug side-effect monitoring. Traditionally blood count is performed either manually or by conventional automated blood analyzers. With the advance of microfabrication, on-chip blood count has become a target for miniaturization aiming at providing cost-effective, functional, capable point-of-care devices and systems that use less than 100 nL of blood sample and generate measurement results within minutes. The focus of this thesis is on investigation of erythrocyte/leukocyte counting and leukocyte differential, which are the two key components in blood count, in microdevices.

Due to the large number ratio of erythrocytes to leukocytes and their property overlap, conventional automated blood analyzers accomplish blood count in several

different channels by measuring different parameters. Similarly, in microdevices, it is desirable that erythrocytes and leukocytes can be separated before further analysis. Two types of hydrodynamic separation devices were investigated to continuously separate erythrocytes and leukocytes based on size. The principle of the device exploits the laminar flow in microdevices and design of streamlines which particles follow. Pillar-shaped devices with single geometrical design demonstrate a binary separation profile. With proper design, separation efficiency over 90% can be achieved. Channel-shaped devices, an improved design, can achieve similar separation efficiency with the added benefits of a smaller footprint, fewer requirements on flow control, and easier integration with downstream components.

Erythrocyte and leukocyte count is accomplished with electrical impedance sensing, which is one of the most accurate ways to measure particle volume. The well-known problem of small double-layer capacitance inherent to micro impedance sensors is solved by two methods: platinum black electroplating on the electrode surface and inductor-induced resonance sensing. In the first method, platinum black is electroplated in situ on the electrode surfaces, which increases the effective surface area by two orders of magnitude and thus increases the double-layer capacitance significantly. The other innovative way, inductor-induced resonance sensing, nullifies the capacitive components in the system at the resonance frequency by connecting a parallel inductor to the system. In this way the sensitivity can be greatly improved and the optimal sensing frequency can be chosen from the inductance value. For both methods, polystyrene

beads of different diameters were used for validation, while diluted blood samples and leukocyte-rich plasma were used to successfully demonstrate the feasibility.

Two-part leukocyte differential is demonstrated in microflow cytometers with fluorescence sensing. Unlike methods used in conventional blood analyzers, undiluted blood samples are stained with nucleic acid stain acridine orange. Lymphocytes and granulocytes emit fluorescent light at different peak frequency after interaction with the dye due to the difference in cellular composition. Using the undiluted sample greatly minimizes sample preparation procedure, and reduces the overall measurement time, the reagent, and the waste volume. These benefits make it a practical method for implementation in microdevices. A throughput of one thousand leukocytes per second was demonstrated, which means the leukocyte differential could be accomplished in a couple of seconds.

Table of Contents

List of Figures

List of Tables

CHAPTER 1

INTRODUCTION

1.1 Complete blood count

1.1.1 Complete blood count and its clinical significance

On average, an adult human male weighing 70 kg contains a blood volume of approximately 5 liters [1, 2]. Remarkably, this entire volume of blood circulates the body once every minute and serves a wide variety of important functions. [3]. Some of these functions include: delivering oxygen and nutrients to every cell of the body, transporting intermediate metabolites and wastes from and toward various tissues, and transporting cells of the immune system throughout the body to perform specific immuno-surveillance functions. Thus, a great deal of information about a given person's body can be inferred by examination of their blood.

As a result, there have been many laboratory tests devised to assist in medical diagnoses; the most ubiquitous of these tests is the complete blood count (CBC). The CBC test determines, as a proportion or absolute number, the quantity of two or more of the following cells present in whole blood: erythrocytes (red blood cell, RBC), leukocytes (white blood cell, WBC), platelets (thrombocytes), and hemoglobin. In addition, the CBC determines the hematocrit (volume ratio of erythrocytes in whole blood), as well as performing what is known as a leukocyte differential. There are many different types of leukocytes. A leukocyte differential further determines, as a ratio or absolute number, the quantity of various types of leukocytes. Leukocyte differential tests come in several types differing in number and types of cells compared. Examples of these tests include; 2-part (lymphocytes versus granulocytes), 3-part (lymphocytes, monocytes, and granulocytes), and 5-part (lymphocytes, monocytes, neutrophils, eosinophils, and basophils) comparisons. Modern automated blood analyzers can provide 5-part absolute leukocyte differentials. Depending on the instrument manufacturer, these modern instruments can measure over 20 parameters, including reticulocyte count. Tables 1-1 and 1-2 list the most common parameters for CBC tests as well as their recommended normal range [4, 5].

Table 1-1 Complete blood count and the normal ranges

WBC	4,500 to 11,000 /μL
Differential white cell count	See Table 2
RBC	4.0 to 6.2 million /μL
Hematocrit	
Women	35% to 47%
Men 8 to 64 yr	39% to 50%
Men 65 to 74 yr	37% to 51%
Hemoglobin concentration	
Women	12 to 16 g/dL
Men	14 to 18 g/dL
RBC indices	
Mean corpuscular volume (MCV)	82 to 93 μm^3
Mean corpuscular Hgb (MCH)	26 to 34 pg
Mean corpuscular Hgb concentration (MCHC)	31% to 38%
Platelet count	150,000 to 400,000 /μL

Table 1-2 Leukocyte differential and the normal ranges

Cell Type	**Absolute (/μL)**	**Differential (%)**
Total WBC	4,500–11,000	100
Granulocytes		
Neutrophils	3,000–7,000	60–70
Segmented	2,800–5,600	54–68
Bands	150–600	3–5
Eosinophils	50–400	1–5
Basophils	25–100	0–0.75
Nongranulocyte		
Monocytes	100–800	3–7
Lymphocytes (Immunocytes)	1,000–4,000	25–33
T cells	800–3,200	80*
B cells	100–600	10–15*
Natural killer	50–400	5–10*

*Percent of total lymphocyte count

It turns out that the wealth of data provided by the CBC is extremely useful in diagnosing the presence, severity, and/or type of the following: anemia, certain cancers, infection, acute hemorrhagic states, various allergies, immunodeficiency, and certain drugs that cause blood dyscrasias [4]. The following sections go into more detail about how CBC data, specifically from leukocyte differential tests, is used to assist in the diagnoses of previously mentioned conditions.

Abnormal leukocyte (WBC) differential results are indicatives of disease processes and toxic challenges to the body [4–6]. Leukocyte abnormalities can be broadly classified into five categories: neutrophilia, eosinophilia, basophilia, monocytosis, and lymphocytosis.

Neutrophilia is an increase in the total neutrophil count (both segmented and band form). Neutrophilia may also be referred to as granulocytosis because neutrophils account for greater than 96% of all granulocytes. It is the most common cause of elevated WBC count and is most commonly caused by an acute bacterial infection and less commonly caused by a Myeloproliferative disorder. An elevation in segmented neutrophils is referred to as a "shift to the right" and is often observed during tissue breakdown from injuries such as burns, arthritis, myocardial infarction, hemorrhage, or electric shock. The correlation between a shift to the right and tissue breakdown is intuitively satisfying because neutrophils are called in to clean up the damaged or dead cells. An elevation in the band form of neutrophils is referred to as a, "*shift to the left*," which means that an increased number of immature neutrophils have been released from the bone marrow and are circulating in the blood. This condition occurs in response to overwhelming infection when mature neutrophil reserves have been depleted. In general,

a shift to the right can be considered a result of tissue damage or necrosis, whereas a shift to the left can be considered a result of an overwhelming infection.

Eosinophilia is an increase in the eosinophil count. Eosinophilia has been found to increase in the presence of parasitic infections, bronchoallergic reactions (i.e., asthma), allergic rhinitis, hay fever, and skin rashes.

Basophila is an increase in the basophil count. It is also the most uncommon cause of an elevated WBC count. Basophil increases have been known to occur in some hypersensitivity reactions, excessive radiation exposure, myeloproliferative disorders, (including polycythemia vera), myelofibrosis with myeloid metaplasia, and chronic granulocytic leukemia (CGL).

Monocytosis, as one can probably infer by now, is an increase in the monocyte count. Monocytosis occurs late during either the acute phase of infection or with chronic infections such as tuberculosis and subacute bacterial endocarditis (SBE).

Lymphocytosis occurs in acute viral infections such as mononucleosis, cytomegalovirus, measles, mumps, and rubella. Elevated lymphocyte counts will also be noted in patients during with a history of chronic infections and may be noted early in patients carrying the human immunodeficiency virus (HIV) disease. Severely elevated levels are seen in chronic lymphocytic leukemia (CLL).

1.1.2 Technology development for complete blood count

Like many other fields of scientific inquiry, our knowledge of blood has evolved in parallel and in proportion with the technology developed for blood analysis [7]. Although blood has been considered the essence of life for centuries, the cellular composition of blood was not recognized until the invention of the microscope by

Leeuwenhoek in the 17th century. In 1852, Karl Vierordt published the first quantitative results of blood cell analysis based on a tedious and lengthy procedure [8]. Later in the 19th century, the improvement of tissue-staining techniques enabled the first manual blood count by means of a combination of hemacytomers and blood smear. Eosin was the first of these tissue-staining dyes discovered in 1856, followed by hematoxylin (discovered in 1865), and later by the metachromatic Romanowsky dyes. Amazingly, modern manual blood count methods are not significantly different from those used over a century ago and those are still the traditional reference method used for calibration of automated blood analyzers. Belonging to the Romanowsky dye family, Wright or Wright-Giemsa staining is the dye most commonly used for blood smear in North America, while May-Grunwald-Giemsa type staining is more popular in Europe and elsewhere [6].

The technological evolution for automated blood count began in mid-1950s. When researchers embarked on the development of automated blood analysis, the ultimate goal of their efforts was to build a device which could provide fast, reliable, and automated 5-part leukocyte differential analysis. Thus far, two different approaches/platforms have been explored. One approach is to build a system based on microscope image analysis. The other approach is to adapt flow-cytometer-based sensing. Attempts to automate WBC differential counting by image analysis using computer-based algorithms [9, 10] are in general not very successful in real clinic patients. These systems are slower and require large amounts of operator interaction [6]. Microscope-based image analysis is primarily constrained by available computing power and algorithm development. However, given the rapid pace of technological advancement in

the fields of computing power and algorithm design this situation might change and present constraints on this method may be alleviated [11]. The flow cytometer platform for blood count is achieved by letting blood cells flow through a restricted sensing zone one by one. Normally, sheath flow and small aperture or capillary tubes are used to achieve this [12]. Classification and enumeration is achieved by combining sensor signals of, for example, DC/AC impedance, forward and side light scattering and/or fluorescence [13]. The first generation of flow cytometer based systems achieved 3-part leukocyte differential separations [14−16]. Although these instruments have their own flagging systems and review criteria, such rule-based systems were surprisingly good at predicting abnormalities in patient specimens requiring manual review or enumeration [6]. The next development came with the introduction of enzyme cytochemical treatments for leukocytes, which enabled 5-part leukocyte differential. The first automated blood analyzer with 5-part differential capability was introduced in the mid 1970s [17, 18]. Since then, bivariate scatterplots have replaced single parameter histograms for data representation. Also, adaptable cluster analysis algorithms have replaced earlier criteria of fixed discriminators. Modern automated blood analyzers rely more on multi-parameter light scattering and DC/AC impedance sensing, and less on cytochemical or immuno staining in order to reduce cost, human interaction, and reagent use. More parameters are added into blood count, and a task force initiated by the International Society for Laboratory Hematology has formulated an approach to achieve extended differential count (EDC), which includes immature granulocytes, reticulocytes (immature erythrocytes without nucleus), nucleated erythrocytes, blasts, atypical lymphocytes, and hematopoietic progenitor cells [6]. New monoclonal antibody-based flow cytometry

methods have been proposed as a new reference method for blood count to replace the error-prone and statistically insufficient manual blood count reference method [19, 20].

1.2 BioMEMS for cell analysis

BioMEMS (Bio Micro Electro-Mechanical Systems) is a subset of MEMS technology, which generally refers to devices that have at least one dimension in the range of ~100 nm to 200 μm [21]. Concisely stated, BioMEMS is the application of MEMS fabrication technology to biological and biomedical fields. The origins of the field lie in microfabricated devices for molecular analysis, e.g., capillary electrophoresis (CE), gas-phase chromatography (GPC), and high-pressure liquid chromatography (HPLC) [22]. After the mid-1990s, polymer plastics, especially poly(dimethylsiloxane) (PDMS), replaced silicon and glass as the most popular materials. Fundamental and unique flow properties in microdomains, such as laminar flow without turbulence [23, 24] and electro-osmotic driven plugged flow [25], have been exploited. Just as integrated circuits have basic building blocks such as resistors, capacitors, and transistors, an analogous set of components, such as valves [26], pumps [27, 28], and mixers[29–31], have been demonstrated for microfluidic systems. Application of bioMEMS systems to resolve problems has emerged in areas such as screening conditions for protein crystallization [32, 33], high-throughput screening in drug development [34, 35], single cell manipulation and analysis [36–39], single molecule analysis [40, 41], and microreactor chemical synthesis [42, 43].

Cell analysis has been an active area in bioMEMS since its inception. Recently it has been reviewed by several authors [36, 37, 44–46]. In microdevices, the spatial and temporal clues for cells can be reproducibly controlled and the heterogeneity of cell

population can be studied with single cell analysis. These new tools create new opportunities for research areas, such as cell biology, developmental biology, and tissue engineering.

Microfabricated cell culture devices can mimic in vivo environments by patterning the extracellular matrix in 3D and providing nutrients and oxygen gradients by microfluidic networks. Live-cell culture and the study of hepatotoxicity for drugs have been of special interest for their potential application in drug discovery [47–49]. Shear stress and mechanical loading are important factors to be controlled locally for bone cell culture [50]. Adherent cells can be stimulated in microdevices by on-chip gradient generators [51–53], while cells in suspension can be stimulated after trapping [54, 55] or by using flow segmentation techniques [56]. Cell sorting has been demonstrated based on dielectrophoresis (DEP) [57], fluorescence (FACS) [58, 59], or affinity [60, 61]. Sample preparation for molecular analysis requires cell lysis, which has been demonstrated effectively on-chip by several approaches, i.e., chemically with surfactant or local hydrogen peroxide generation [62, 63], mechanically by forcing cells through nanoscale barbs [64], and electrically by irreversible destruction of plasma membrane [65]. PCR or reverse transcription PCR (RT-PCR) are applied to amplify cellular DNA or RNA in either flow-through or thermal cycle fashion [66]. Protein and DNA fractionation has been achieved with the use of nano-filters [67], but electrokinetic separation techniques — such as capillary electrophoresis (CE), gel electrophoresis, electrochromatography, and isoelectric focusing (IEF) — are more popular [68, 69].

1.3 Fabrication technologies

In this subsection, two microfabrication technologies used in later chapters are introduced. One is soft lithography. The other is integrated parylene technology.

1.3.1 Soft lithography

Soft lithography is a set of non-photolithographic microfabrication techniques that use a patterned elastomer as the stamp, mold, or mask (rather than a rigid photomask) to generate micropatterns and microstructures [70]. The pattern transfer process generally contains three steps: (1) fabricating a patterned master, (2) molding the master to generate a patterned stamp, (3) generating a replica of the original template in a functional material by applying the stamp [71]. Soft lithography can be categorized into replica molding, embossing, and microcontact printing. The fabrication technique used in this thesis is replica molding, which refers to transferring topographical features from a rigid or elastomeric mold into another material by solidifying a liquid in contact with the original pattern.

The common master material is either made using silicon or SU8 (a UV patternable epoxy) on silicon. Silicon masters can be precisely micromachined using DRIE and are widely used in the research community, while SU8 masters are typically lower cost and require less-specialized equipment to create. The elastomer most commonly used is poly(dimethylsiloxane) (PDMS), which is silicone rubber. PDMS has a number of useful properties: it is inert to many chemicals (including most inorganic solvents), has a low surface energy (γ = 21.6 dyn/cm^2) which facilitates its release from the master after curing, it is thermally stable below ~ 150 ℃, optically transparent down to ~ 300 nm, mechanically tough (tensile modulus of 4.77 MPa), flexible (elastic

modulus of 1.8 MPa and elongation up to ~ 160%), and gas permeable. PDMS is considered to be a suitable reference material for the evaluation of the in vitro and in vivo biocompatibility of biomaterials [72]. The gas permeable property of PDMS makes it a desirable material for applications where gas transport is preferred (e.g., on-chip cell culture).

The general fabrication process used in this thesis is shown in Fig. 1-1. The first step in the process: the master (mold) is generated with photolithography on silicon wafer using deep reactive ion etching (DRIE). Then PDMS prepolymers (e.g., Sylgard 184, Dow Corning, Midland, MI, USA) are mixed vigorously, degassed, poured over the master, and cured in a oven. After thermal curing, the PDMS is peeled off the mold, and cut into individual devices. The fluidic vias are punched through the material with a stainless steel tube. Finally, the devices are bonded to a clean glass slide or glass wafer die. This procedure can be modified to include multiple layers of PDMS through PDMS/PDMS bonding. Multilayer PDMS structures make the integration of valves and pumps relatively simple [73]. The surface of PDMS can be modified physically by corona, plasma, or laser treatment, or chemically by surface grafting. The bulk property of PDMS can be modified by blending, copolymerization, interpenetrating polymer networks, and functionalization [74].

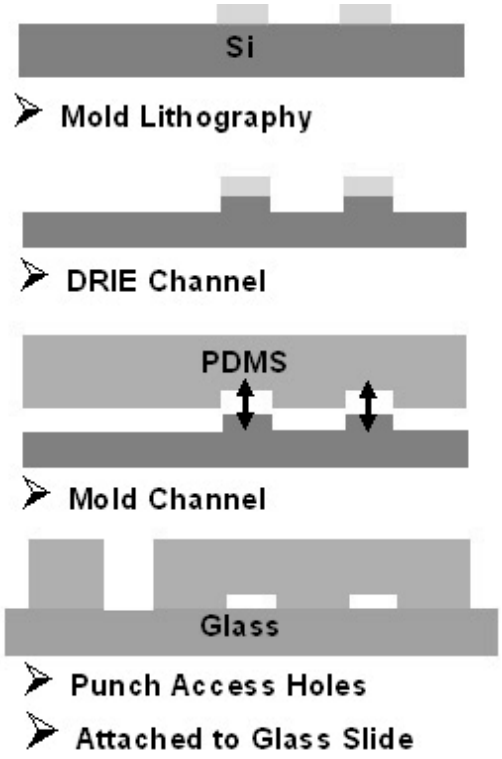

Figure 1-1 *PDMS device fabrication process*

The relative ease of processing, biocompatibility, low material and fabrication cost, and the previously enumerated properties of PDMS have made the PDMS-based soft lithography the most widely used fabrication technology in bioMEMS so far. Useful microfluidic components, such as pneumatic valves and pumps, can be integrated easily and reliably, which makes PDMS the key material for exploratory research [75]. Large scale fluidics integration has been demonstrated [76, 77].

1.3.2 Integrated parylene technology

Parylene (poly-para-xylylene) was discovered in 1947 and commercialized by Union Carbide Corporation in 1965 [78]. Fig. 1-2 shows the chemical structures of the most commonly used parylene: parylenes N, C and D. Ever since its discovery, the

number of applications for parylene has grown dramatically in electronics, medical devices, the automobile industry, and the military.

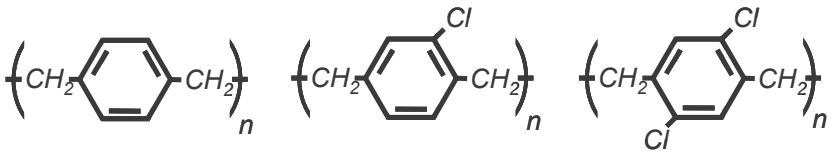

Parylene N Parylene C Parylene D

Figure 1-2 *Chemical structures of parylene N, C, and D*

The wide application of parylene is due to its rather unique properties (Table 1-3). Parylene films are mechanically strong and flexible. Parylene C has an elongation break of 200%, which makes it a good building material for MEMS applications requiring high pressure. Parylene is also an excellent electrical insulator: The electrical breakdown voltage of a one micron thick parylene layer is over 200 volts. It is also an excellent thermal insulator: the room temperature thermal conductivity of parylene C is only three times as large as static air (0.30 mW/cm-K). The electrical and physical properties of parylene are unchanged when it cycles between room temperature and 2 ^{o}K. In terms of optical properties, parylene is transparent in the visible light range. However, parylene absorbs strongly for wavelengths shorter than 280 nm, which limits some of its UV applications. Parylene is an excellent barrier for gas and moisture: the gas permeability of parylene is more than four orders of magnitude smaller and the moisture permeability is ten times smaller than PDMS. Parylene is completely inert to most chemicals and solvents used in chemical or biological laboratories. Swelling caused by solvents is minor on parylene N, C, and D, with a 3% maximum increase in film thickness, and is completely reversible after the solvents are removed by vacuum drying. Furthermore,

parylene is biocompatible (USP Class VI), which makes it one of the few materials best suited for long-term human implants. Parylene thin films are deposited using a room-temperature CVD process which makes parylene deposition a post-CMOS compatible process. Parylene thin films can be processed by conventional lithography processes and oxygen plasma etching in RIE (reactive ion etching) instrument. The newest commercially available parylene, parylene HT from Specialty Coating Systems (SCS), provides the highest temperature and UV stability and lowest dielectric and friction coefficients.

Table 1-3 Properties for parylene N, C, D, HT, and PDMS [79, 80].

Property	Parylene-N	Parylene-C	Parylene-D	Parylene HT	PDMS [80]
Dielectric Strength (V/mil), 1 mil film	7,000	5,600	5,500	5,400	610 [81] (1 mm film)
Dielectric Constant					2.3–2.8
60 Hz	2.65	3.15	2.84	2.21	
1 kHz	2.65	3.10	2.82	2.20	
1 MHz	2.65	2.95	2.80	2.17	
Young's Modulus (psi)	350,000	400,000	380,000	—	52–126
Index of Refraction	1.661	1.639	1.669	—	1.4
Yield Strength (psi)	6,100	8,000	9,000	—	325
Elongation to Break (%)	20–250	200	10	—	210–310 [81]
Coefficient of Friction					
Static	0.25	0.29	0.33	0.145	—
Dynamic	0.25	0.29	0.31	0.130	0.43–0.51 [82]
Density (g/cm^3)	1.10–1.12	1.289	1.418	—	$9.7*10^{-4}$
Melting Point (℃)	420	290	380	> 450	-49.9–40
Thermal Conductivity at 25 ℃ (10^{-4} cal/(cm*s*℃))	3.0	2.0	—	—	3.6
Specific Heat at 20 ℃ (cal/g*℃)	0.20	0.17	—	—	0.35

Fig. 1-3 shows the parylene deposition procedures, the involved chemical processes, and the instrument. The process includes vaporization, pyrolysis, and deposition. Beginning with the stable granular parylene dimmer (di-para-xylylene), the material is vaporized under vacuum (8−10 mTorr) and heated to 170 ℃ to form dimeric gas. The gas is then pyrolized to cleave the dimer to its monomeric form at 690 ℃. In the room-temperature deposition chamber, the monomer gas deposits on all exposed surfaces as a transparent polymer film (poly-para-xylylene). Although parylene N structure is used in Fig. 1-3, the deposition process is almost identical for all three common types of parylene, except for some slight differences in pyrolysis temperature and deposition pressure. The thickness of the parylene coating is controlled by the amount of the dimer used. Typical parylene coating thicknesses in a single deposition ranges from 0.1 to 20 μm. The normal deposition rate of parylene C under a deposition vapor pressure of 23 mTorr is about 5 μm per hour. The deposition rate is directly proportional to the square of the monomer concentration in the chamber and inversely proportional to the absolute temperature of the substrate on which parylene will be coated [83].

The room-temperature conformal deposition, the pin-hole-free high film quality, the excellent physical and chemical properties and the easiness of processing make parylene a good material for MEMS surface micromachining. Parylene microfluidic devices such as channels, pumps/valves, filters, pressure and flow sensors, mass flow controllers, electrospray nozzles, and liquid chromatography columns have been

successfully demonstrated (Fig. 1-4) [84–89]. The bio-compatibility of parylene makes it a perfect material for implantable or bioprocessing devices [90].

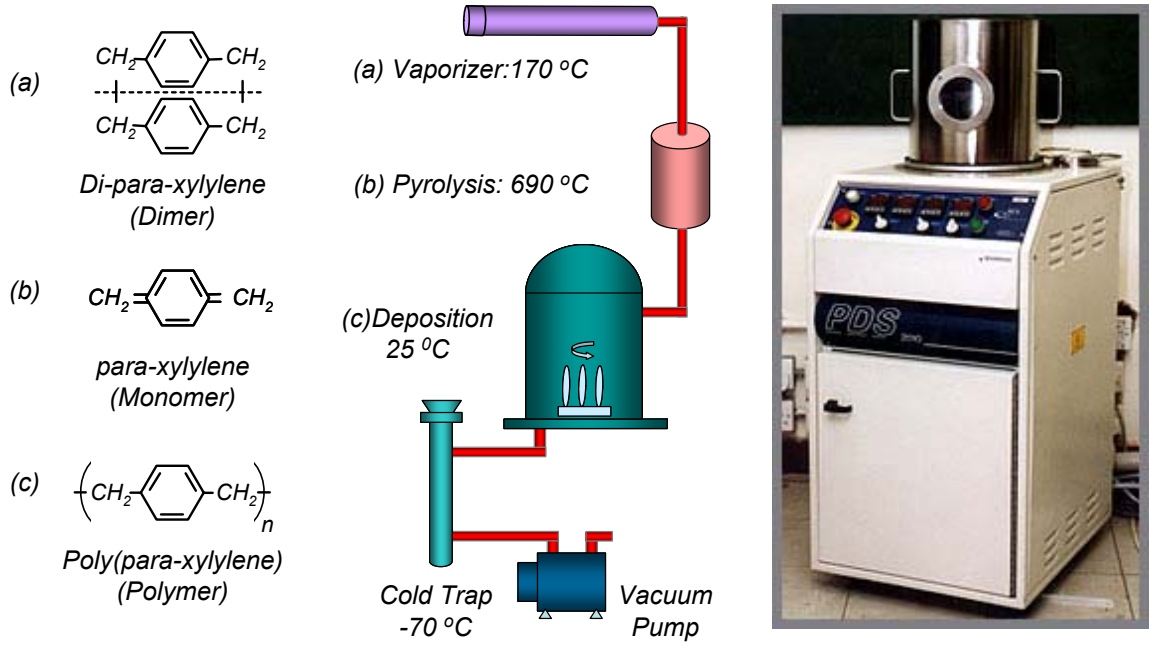

Figure 1-3 *Parylene deposition system and the involved chemical processes*

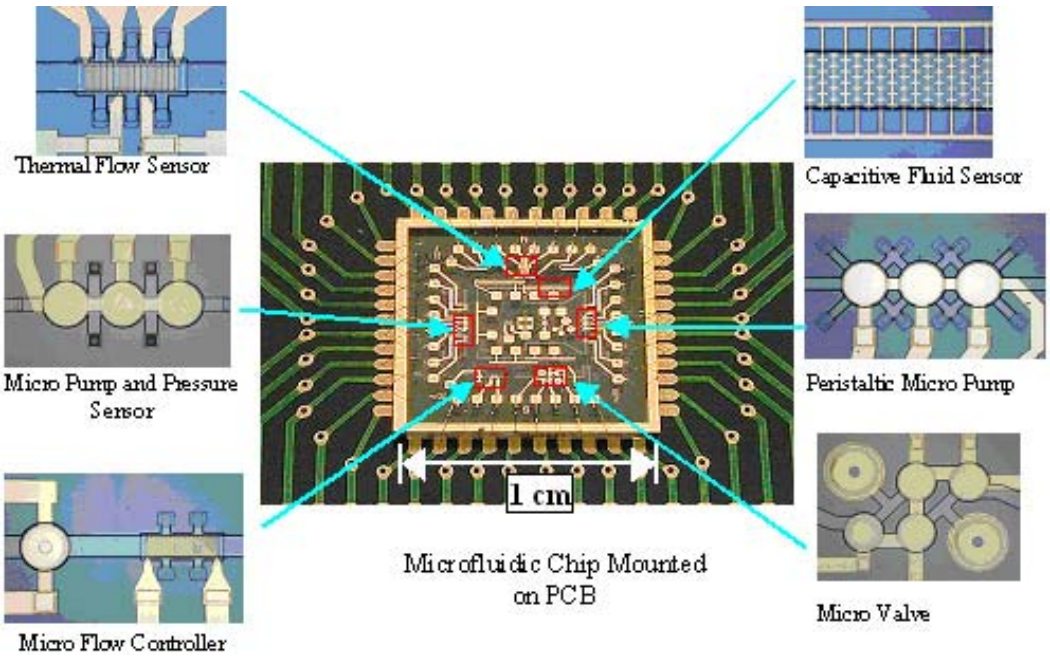

Figure 1-4 *Parylene microfluidic devices. (Courtesy Dr. Yu-Chong Tai)*

1.4 Bibliography

[1] "Blood," in *Encyclopedia Britannica*. Chicago: Encyclopedia Britannica, 1973.

[2] C. Starr and R. Taggart, *Biology: The Unity and Diversity of Life, 10th ed.* California: Brooks Cole, 2003.

[3] A. L. Komaroff, *Harvard Medical School Family Health Guide, 1st ed.*. Free Press, 1999.

[4] B. George-Gay and K. Parker, "Understanding the complete blood count with differential," *Journal Of PeriAnesthesia Nursing*, vol. 18, pp. 96−117, 2003.

[5] S. B. McKenzie, *Clinical Laboratory Hematology*. Prentice Hall, 2004.

[6] B. Houwen, "The differential cell count," *Laboratory Hematology*, vol. 7, pp. 89−100, 2001.

[7] M. M. Wintrobe, *Blood, pure and eloquent: a story of discovery, of people, and of ideas*. New York: McGraw-Hill, 1980.

[8] K. Vierordt, "Zahlungen der blutkorperchen des menschen," *Arch Physiol Heilk*, vol. 11, 327, 1852.

[9] G. Mahouy, P. R. Lund, S. Chinn, and R. D. Barnes, "The use of automated image analysis in differential white cell counting," *Scandinavian Journal Of Haematology*, vol. 10, pp. 315−318., 1973.

[10] J. K. Mui, K. S. Fu, and J. W. Bacus, "Automated classification of blood cell neutrophils," *Journal Of Histochemistry and Cytochemistry*, vol. 25, pp. 633−640, 1977.

[11] H. M. Shapiro and N. G. Perlmutter, "Personal cytometers: Slow flow or no flow?" *Cytometry Part A*, vol. 69A, pp. 620−630, 2006.

[12] P. J. Crossland-Taylor, "A device for counting small particles suspended in fluid through a tube," *Nature*, vol. 171, 37, 1953.

[13] H. M. Shapiro, *Practical flow cytometry*, *4th ed.* Hoboken, New Jersey: John Wiley & Sons, Inc., 2003.

[14] C. L. Johnston, "Leukocyte screening using the ELT-800WS," *Blood Cells*, vol. 11, pp. 241−255, 1985.

[15] C. J. Cox, T. M. Habermann, B. A. Payne, G. G. Klee, and R. V. Pierre, "Evaluation of the Coulter counter model S-Plus IV," *American Journal Clinical Pathology*, vol. 84, pp. 297−306, 1985.

[16] W. Burgi and H. R. Marti, "Automated blood count analysis by trimodal size distribution with the Sysmex E-5000," *Journal Of Clinical Chemistry And Clinical Biochemistry*, vol. 27, 365−368, 1989.

[17] A. M. Saunders, "Development of automation of differential leukocyte counts by the use of cytochemistry," *Clinical Chemistry*, vol. 18, 783−788, 1972.

[18] H. P. Mansberg, A. M. Saunders, and W. Groner, "The Hemalog-D white cell differential system," *Journal Of Histochemistry and Cytochemistry*, vol. 22, 711−724, 1974.

[19] W. Hubl, S. Andert, A. Erath, A. Lapin, and P. M. Bayer, "Peripheral-Blood Monocyte Counting — Towards A New Reference Method," *European Journal Of Clinical Chemistry And Clinical Biochemistry*, vol. 33, pp. 839−845, 1995.

[20] W. Hubl, G. Wolfbauer, S. Andert, G. Thum, J. Streicher, C. Hubner, A. Lapin, and P. M. Bayer, "Toward a new reference method, for the leukocyte five-part differential," *Cytometry*, vol. 30, 72−84, 1997.

[21] S. S. Saliterman, *Fundamentals of BioMEMS and Medical Microdevices*. SPIE, 2006.

[22] G. M. Whitesides, "The origins and the future of microfluidics," *Nature*, vol. 442, pp. 368−373, 2006.

[23] J. P. Brody, P. Yager, R. E. Goldstein, and R. H. Austin, "Biotechnology at low Reynolds numbers," *Biophysical Journal*, vol. 71, pp. 3430−3441, 1996.

[24] T. M. Squires and S. R. Quake, "Microfluidics: Fluid physics at the nanoliter scale," *Reviews Of Modern Physics*, vol. 77, pp. 977−1026, 2005.

[25] J. G. Santiago, "Electroosmotic flows in microchannels with finite inertial and pressure forces," *Analytical Chemistry*, vol. 73, pp. 2353−2365, 2001.

[26] K. W. Oh and C. H. Ahn, "A review of microvalves," *Journal Of Micromechanics And Microengineering*, vol. 16, pp. R13−R39, 2006.

[27] D. J. Laser and J. G. Santiago, "A review of micropumps," *Journal Of Micromechanics And Microengineering*, vol. 14, pp. R35−R64, 2004.

[28] N. T. Nguyen, X. Y. Huang, and T. K. Chuan, "MEMS-micropumps: A review," *Journal Of Fluids Engineering—Transactions Of The ASME*, vol. 124, pp. 384−392, 2002.

[29] S. Jayaraj, S. M. Kang, and Y. K. Suh, "A review on the analysis and experiment of fluid flow and mixing in micro-channels," *Journal Of Mechanical Science And Technology*, vol. 21, pp. 536−548, 2007.

[30] V. Hessel, H. Lowe, and F. Schonfeld, "Micromixers—a review on passive and active mixing principles," *Chemical Engineering Science*, vol. 60, pp. 2479–2501, 2005.

[31] N. T. Nguyen and Z. G. Wu, "Micromixers—a review," *Journal Of Micromechanics And Microengineering*, vol. 15, pp. R1–R16, 2005.

[32] C. L. Hansen, E. Skordalakes, J. M. Berger, and S. R. Quake, "A robust and scalable microfluidic metering method that allows protein crystal growth by free interface diffusion," *Proceedings Of The National Academy Of Sciences Of The United States Of America*, vol. 99, pp. 16531–16536, 2002.

[33] B. Zheng, J. D. Tice, L. S. Roach, and R. F. Ismagilov, "A droplet-based, composite PDMS/glass capillary microfluidic system for evaluating protein crystallization conditions by microbatch and vapor-diffusion methods with on-chip X-ray diffraction," *Angewandte Chemie-International Edition*, vol. 43, pp. 2508–2511, 2004.

[34] P. S. Dittrich and A. Manz, "Lab-on-a-chip: microfluidics in drug discovery," *Nature Reviews Drug Discovery*, vol. 5, pp. 210–218, 2006.

[35] J. Pihl, M. Karlsson, and D. T. Chiu, "Microfluidic technologies in drug discovery," *Drug Discovery Today*, vol. 10, pp. 1377–1383, 2005.

[36] J. Voldman, "Engineered systems for the physical manipulation of single cells," *Current Opinion In Biotechnology*, vol. 17, 532, 2006.

[37] H. Andersson and A. van den Berg, "Microtechnologies and nanotechnologies for single-cell analysis," *Current Opinion in Biotechnology*, vol. 15, 44, 2004.

[38] A. R. Wheeler, W. R. Throndset, R. J. Whelan, A. M. Leach, R. N. Zare, Y. H. Liao, K. Farrell, I. D. Manger, and A. Daridon, "Microfluidic device for single-cell analysis," *Analytical Chemistry*, vol. 75, pp. 3581−3586, 2003.

[39] A. A. Werdich, E. A. Lima, B. Ivanov, I. Ges, M. E. Anderson, J. P. Wikswo, and F. J. Baudenbacher, "A microfluidic device to confine a single cardiac myocyte in a sub-nanoliter volume on planar microelectrodes for extracellular potential recordings," *Lab On A Chip*, vol. 4, pp. 357−362, 2004.

[40] S. M. Stavis, J. B. Edel, K. T. Samiee, and H. G. Craighead, "Single molecule studies of quantum dot conjugates in a submicrometer fluidic channel," *Lab On A Chip*, vol. 5, pp. 337−343, 2005.

[41] P. S. Dittrich and A. Manz, "Single-molecule fluorescence detection in microfluidic channels—the Holy Grail in mu TAS?" *Analytical And Bioanalytical Chemistry*, vol. 382, pp. 1771−1782, 2005.

[42] A. J. deMello, "Control and detection of chemical reactions in microfluidic systems," *Nature*, vol. 442, pp. 394−402, 2006.

[43] V. Hessel and H. Lowe, "Chemical microprocess engineering: Current trends and issues to be resolved," in *Microreactor Technology And Process Intensification*, *Acs Symposium Series*, vol. 914, pp. 23−46 2005.

[44] J. El-Ali, P. K. Sorger, and K. F. Jensen, "Cells on chips," *Nature*, vol. 442, pp. 403−411, 2006.

[45] C. E. Sims and N. L. Allbritton, "Analysis of single mammalian cells on-chip," *Lab On A Chip*, vol. 7, pp. 423−440, 2007.

[46] H. Andersson and A. van den Berg, "Microfluidic devices for cellomics: a review," *Sensors And Actuators B—Chemical*, vol. 92, pp. 315−325, 2003.

[47] S. N. Bhatia, M. L. Yarmush, and M. Toner, "Controlling cell interactions by micropatterning in co-cultures: Hepatocytes and 3T3 fibroblasts," *Journal Of Biomedical Materials Research*, vol. 34, pp. 189−199, 1997.

[48] A. Sivaraman, J. K. Leach, S. Townsend, T. Iida, B. J. Hogan, D. B. Stolz, R. Fry, L. D. Samson, S. R. Tannenbaum, and L. G. Griffith, "A microscale in vitro physiological model of the liver: Predictive screens for drug metabolism and enzyme induction," *Current Drug Metabolism*, vol. 6, pp. 569−591, 2005.

[49] M. J. Powers, K. Domansky, M. R. Kaazempur-Mofrad, A. Kalezi, A. Capitano, A. Upadhyaya, P. Kurzawski, K. E. Wack, D. B. Stolz, R. Kamm, and L. G. Griffith, "A microfabricated array bioreactor for perfused 3D liver culture," *Biotechnology And Bioengineering*, vol. 78, pp. 257−269, 2002.

[50] E. Leclerc, B. David, L. Griscom, B. Lepioufle, T. Fujii, P. Layrolle, and C. Legallaisa, "Study of osteoblastic cells in a microfluidic environment," *Biomaterials*, vol. 27, pp. 586−595, 2006.

[51] G. M. Walker, J. Q. Sai, A. Richmond, M. Stremler, C. Y. Chung, and J. P. Wikswo, "Effects of flow and diffusion on chemotaxis studies in a microfabricated gradient generator," *Lab On A Chip*, vol. 5, pp. 611−618, 2005.

[52] N. L. Jeon, H. Baskaran, S. K. W. Dertinger, G. M. Whitesides, L. Van de Water, and M. Toner, "Neutrophil chemotaxis in linear and complex gradients of interleukin-8 formed in a microfabricated device," *Nature Biotechnology*, vol. 20, pp. 826−830, 2002.

[53] V. V. Abhyankar, M. A. Lokuta, A. Huttenlocher, and D. J. Beebe, "Characterization of a membrane-based gradient generator for use in cell-signaling studies," *Lab On A Chip*, vol. 6, pp. 389–393, 2006.

[54] P. J. Lee, P. J. Hung, R. Shaw, L. Jan, and L. P. Lee, "Microfluidic application-specific integrated device for monitoring direct cell-cell communication via gap junctions between individual cell pairs," *Applied Physics Letters*, vol. 86, 2005.

[55] M. S. Yang, C. W. Li, and J. Yang, "Cell docking and on-chip monitoring of cellular reactions with a controlled concentration gradient on a microfluidic device," *Analytical Chemistry*, vol. 74, pp. 3991–4001, 2002.

[56] J. El-Ali, S. Gaudet, A. Gunther, P. K. Sorger, and K. F. Jensen, "Cell stimulus and lysis in a microfluidic device with segmented gas-liquid flow," *Analytical Chemistry*, vol. 77, pp. 3629–3636, 2005.

[57] X. Y. Hu, P. H. Bessette, J. R. Qian, C. D. Meinhart, P. S. Daugherty, and H. T. Soh, "Marker-specific sorting of rare cells using dielectrophoresis," *Proceedings Of The National Academy Of Sciences Of The United States Of America*, vol. 102, pp. 15757–15761, 2005.

[58] A. Y. Fu, C. Spence, A. Scherer, F. H. Arnold, and S. R. Quake, "A microfabricated fluorescence-activated cell sorter," *Nature Biotechnology*, vol. 17, pp. 1109–1111, 1999.

[59] M. M. Wang, E. Tu, D. E. Raymond, J. M. Yang, H. C. Zhang, N. Hagen, B. Dees, E. M. Mercer, A. H. Forster, I. Kariv, P. J. Marchand, and W. F. Butler, "Microfluidic sorting of mammalian cells by optical force switching," *Nature Biotechnology*, vol. 23, pp. 83–87, 2005.

[60] A. Revzin, K. Sekine, A. Sin, R. G. Tompkins, and M. Toner, "Development of a microfabricated cytometry platform for characterization and sorting of individual leukocytes," *Lab On A Chip*, vol. 5, pp. 30−37, 2005.

[61] W. C. Chang, L. P. Lee, and D. Liepmann, "Biomimetic technique for adhesion-based collection and separation of cells in a microfluidic channel," *Lab On A Chip*, vol. 5, pp. 64−73, 2005.

[62] D. Di Carlo, C. Ionescu-Zanetti, Y. Zhang, P. Hung, and L. P. Lee, "On-chip cell lysis by local hydroxide generation," *Lab On A Chip*, vol. 5, pp. 171−178, 2005.

[63] D. Irimia, R. G. Tompkins, and M. Toner, "Single-cell chemical lysis in picoliter-scale closed volumes using a microfabricated device," *Analytical Chemistry*, vol. 76, pp. 6137−6143, 2004.

[64] D. Di Carlo, K. H. Jeong, and L. P. Lee, "Reagentless mechanical cell lysis by nanoscale barbs in microchannels for sample preparation," *Lab On A Chip*, vol. 3, pp. 287−291, 2003.

[65] F. T. Han, Y. Wang, C. E. Sims, M. Bachman, R. S. Chang, G. P. Li, and N. L. Allbritton, "Fast electrical lysis of cells for capillary electrophoresis," *Analytical Chemistry*, vol. 75, pp. 3688−3696, 2003.

[66] M. A. Burns, B. N. Johnson, S. N. Brahmasandra, K. Handique, J. R. Webster, M. Krishnan, T. S. Sammarco, P. M. Man, D. Jones, D. Heldsinger, C. H. Mastrangelo, and D. T. Burke, "An integrated nanoliter DNA analysis device," *Science*, vol. 282, pp. 484−487, 1998.

[67] J. Han and H. G. Craighead, "Separation of long DNA molecules in a microfabricated entropic trap array," *Science*, vol. 288, pp. 1026−1029, 2000.

[68] N. Lion, T. C. Rohner, L. Dayon, I. L. Arnaud, E. Damoc, N. Youhnovski, Z. Y. Wu, C. Roussel, J. Josserand, H. Jensen, J. S. Rossier, M. Przybylski, and H. H. Girault, "Microfluidic systems in proteomics," *Electrophoresis*, vol. 24, pp. 3533−3562, 2003.

[69] T. Vilkner, D. Janasek, and A. Manz, "Micro total analysis systems. Recent developments," *Analytical Chemistry*, vol. 76, pp. 3373−3385, 2004.

[70] Y. N. Xia and G. M. Whitesides, "Soft lithography," *Annual Review Of Materials Science*, vol. 28, pp. 153−184, 1998.

[71] B. D. Gates, Q. B. Xu, J. C. Love, D. B. Wolfe, and G. M. Whitesides, "Unconventional nanofabrication," *Annual Review Of Materials Research*, vol. 34, pp. 339−372, 2004.

[72] M. C. Belanger and Y. Marois, "Hemocompatibility, biocompatibility, inflammatory and in vivo studies of primary reference materials low-density polyethylene and polydimethylsiloxane: A review," *Journal Of Biomedical Materials Research*, vol. 58, pp. 467−477, 2001.

[73] M. A. Unger, H. P. Chou, T. Thorsen, A. Scherer, and S. R. Quake, "Monolithic microfabricated valves and pumps by multilayer soft lithography," *Science*, vol. 288, pp. 113−116, 2000.

[74] F. Abbasi, H. Mirzadeh, and A. A. Katbab, "Modification of polysiloxane polymers for biomedical applications: a review," *Polymer International*, vol. 50, pp. 1279−1287, 2001.

[75] G. M. Whitesides and A. D. Stroock, "Flexible methods for microfluidics," *Physics Today*, vol. 54, pp. 42−48, 2001.

[76] T. Thorsen, S. J. Maerkl, and S. R. Quake, "Microfluidic Large-Scale Integration," *Science*, vol. 298, pp. 580−584, 2002.

[77] F. K. Balagadde, L. C. You, C. L. Hansen, F. H. Arnold, and S. R. Quake, "Long-term monitoring of bacteria undergoing programmed population control in a microchemostat," *Science*, vol. 309, pp. 137−140, 2005.

[78] http://www.scscoatings.com/parylene_knowledge/history.cfm. Indianapolis, IN, U.S.A: Specialty Coating Systems.

[79] http://www.scscoatings.com/parylene_knowledge/specifications.cfm. Indianapolis, IN, U.S.A: Specialty Coating Systems.

[80] J. E. Mark, *Polymer data handbook*. New York: Oxford University Press, 1999.

[81] J.-H. Lee and W. Y. Ji, "Electrical and Mechanical Properties of Silicone Rubber for High Voltage Insulation," *presented at International Conference on Properties and Applications of Dielectric Materials*, Nagoya, Japan, 2003.

[82] B. Bhushan and Z. Burton, "Adhesion and friction properties of polymers in microfluidic devices," *Nanotechnology*, vol. 16, pp. 467−478, 2005.

[83] Specifications and properties of Parylene, SCS_Parylene. Cookson Electronics: Specialty Coating Systems, 2005.

[84] L. Licklider, X. Q. Wang, A. Desai, Y. C. Tai, and T. D. Lee, "A micromachined chip-based electrospray source for mass spectrometry," *Analytical Chemistry*, vol. 72, pp. 367−375, 2000.

[85] J. Xie, Y. Miao, J. Shih, Q. He, J. Liu, Y. C. Tai, and T. D. Lee, "An Electrochemical Pumping System for On-Chip Gradient Generation," *Analytical Chemistry*, vol. 76, pp. 3756−3763, 2004.

[86] H. S. Noh, P. J. Hesketh, and G. C. Frye-Mason, "Parylene gas chromatographic column for rapid thermal cycling," *Journal of Microelectromechanical Systems*, vol. 11, pp. 718−725, 2002.

[87] X. Q. Wang and Y. C. Tai, "Normally closed in-channel micro check valve," *presented at the 13th IEEE International Conference on Micro Electro Mechanical Systems (MEMS 2000)*, Miyazaki, Japan, 2000.

[88] J. Xie, X. Yang, X. Q. Wang, and Y. C. Tai, "Surface micromachined leakage proof parylene check valve," *presented at the 14th IEEE International Conference on Micro Electro Mechanical Systems (MEMS 2001)*, Interlaken, Switzerland, 2001.

[89] J. Xie, J. Shih, and Y. C. Tai, "Integrated surface-micromachined mass flow controller," *presented at the 16th IEEE International Conference on Micro Electro Mechanical Systems (MEMS 2003)*, Kyoto, Japan, 2003.

[90] D. C. Rodger and Y. C. Tai, "Microelectronic packaging for retinal prostheses," *IEEE Engineering in Medicine and Biology Magazine*, vol. 24, pp. 52−57, 2005.

CHAPTER 2

BLOOD CELL SEPARATION

2.1 Introduction

Blood cell (here mainly erythrocyte and leukocyte) separation is an important sample preparation step for blood count application. Due to the large number ratio of erythrocytes to leukocytes (approximately 1,000 to 1) and the similarities of their properties (e.g., size, electrical impedance, optical scattering cross area), using whole blood to achieve whole blood count within clinical significant accuracy range is extremely challenging. Because performing cell count with an unseparated blood sample is challenging, conventional automated blood analyzers utilize multiple channels and sensors to count different components inside the blood [1, 2]. For example, in most of the automated hemocytometers made by Beckman Coulter, Inc., (http://www.beckmancoulter.com) erythrocytes are counted in one channel by electrical

impedance sensors from diluted whole blood samples. Leukocytes are counted and differentiated into 3- or 5-parts in another channel by a combination of DC and AC electrical impedance sensing and/or multi-parameter light scattering with hemolyzed blood samples. Sometimes differential lysing is needed to differentiate basophils from the rest of the leukocytes before these basophils are counted in another channel. Often, platelets are counted in one additional channel. Separating the whole blood sample into several subgroups of specific cell types enables the sensitivity of the sensors to be significantly improved because the sensors are designed for one specific type of blood cell, instead of all the blood cells. In this chapter, separation of erythrocytes and leukocytes are studied in microdomain. The goal of this research aims specifically to develop a simple, reusable, continuous separation method using microfluidics for erythrocyte and leukocyte separation without the need for lysing chemicals.

2.1.1 Blood cell composition and geometrical characteristics

Human blood cells can be generally classified into three types: erythrocytes (RBC), leukocytes (WBC), and platelets. Leukocytes can be further classified into granulocytes, monocytes, and lymphocytes. Granulocytes can be further classified into three categories—neutrophils, eosinophils, and basophils—depending on their affinity to different pH-sensitive dyes. Table 2-1 compares the geometries and counts of erythrocytes and leukocytes in adults. Because of its shape, the height of a normal erythrocyte varies from 1.5 to 3.5 μm [3], and it is clearly smaller than an average leukocyte, whose diameter falls between 6 and 20 μm. This difference in size enables the size-based separation of erythrocytes and leukocytes. Table 2-2 shows the composition and geometrical size of leukocytes. A comparison between Table 2-1 and 2-2 shows that

the challenge of size-based separation of erythrocytes and leukocytes can come from the size overlap between erythrocytes and the small lymphocytes, which are dominated by T-lymphocytes.

Table 2-1 Comparison of human erythrocytes, leukocytes, and platelets [1, 4–6]

Cell Type	Cell Shape	Diameter Average (μm)	Diameter Range (μm)	Height (μm)	Count (10^9/L)
Erythrocytes	biconcave disk	8	7–9	1.5–3.0	$3.8–5.9\times10^3$
Leukocytes	sphere	13	6–20	6–20	4.5–11.0
Platelets	irregular	—	2-4	—	$1.5–3\times10^2$

Table 2-2 Components and size of human leukocytes [1, 5, 6]

Leukocyte Type	Diameter Range (μm)	Absolute Count (μL)	Percentage (%)
Total WBC	6–20	4,500–11,000	100
Lymphocytes (Immunocytes)†	7–18	1,000–4,000	25–33
T cells	6–9	800–3,200	80*
B cells	9–15	100–600	10–15*
Natural killer	—	50–400	5–10*
Granulocytes	10–18	3,000–7,500	60–75
Neutrophils†	13–18	3,000–7,000	59–70
Segmented	13–17	2,800–5,600	54–68
Band	16–18	150–600	3–5
Eosinophils†	12–15	50–400	1–5
Basophils†	10–14	25–100	0–0.75
Monocytes†	12–20	100–800	3–7

†5-part differential measurands *Percent of total lymphocyte count

2.1.2 Conventional cell separation techniques

Cells can be extremely heterogeneous, and a good example is cells in human blood. Although the majority of cells are erythrocytes, a mixture of leukocytes inside human blood has very important immunological functions [1]. Even rarer inside blood are circulating tumor cells [7, 8] and hematopoietic stem cells [9].

Traditionally, biological cells can be separated from the surrounding media and each other by different methods. One of the simplest and common ways is centrifugation and ultracentrifugation. If a tube of collected human blood is kept vertical, it can normally be fractionated in 30 to 80 minutes due to specific gravity difference. During this sedimentation process, erythrocytes go to the bottom, while leukocytes form the "buffy coat" layer between packed erythrocytes and plasma. Density-gradient centrifugation is used to expedite the natural sedimentation process in Ficoll-Paque protocol for lymphocyte purification, where erythrocyte agglutination reagent Ficoll helps to move erythrocytes down to the bottom of the centrifugation tube faster and high-density reagent sodium metrizoate or sodium diatrizoate keeps lymphocytes inside the plasma [10, 11]. Another simple method for cell separation is size-based filtering. For example, polycarbonate filters of 8 μm pores made by track etching can be used to isolate circulating tumor cells from blood samples with high recovery and enrichment [12, 13]. More powerful and perhaps the most important cell separation methods are based on immune recognition between antibody and antigen. Immunomagnetic separation uses antibody coated magnetic beads to label target cells, followed by applying a magnetic field to the sample mixture to capture the cells bound to the magnetic beads while eluting out the other cells. Target cells can be collected by

turning off the magnetic field. [14]. Fluorescent activated cell sorting (FACS) is the most widely used technique for cell separation. Target cells are labeled with fluorophore-conjugated antibodies before flowing into a flow cytometer. The flow cytometer sorts the cells electrically and/or mechanically based on the fluorescent signal [2].

2.1.3 Micro scale cell separation

Recently, there are increasing efforts toward cell separation in microscale. Field-flow fractionation is a group of technologies that requires continuous elution. An electric field is placed perpendicular to the fluid flow, which is laminar due to the microscale geometry. Particles are levitated by the field to different stream laminae, and separated due to different flow velocity in the parabolic laminar flow profile. Particles can be differentiated by the nature of the field applied. For example, investigators from Giddings' group use sedimentation field-flow fractionation to separate erythrocytes in less than five minutes [15, 16]. In another attempt, Gascoyne's group uses electrorotation to measure cell membrane capacitance of T- and B- lymphocytes, monocytes, and granulocytes [17]. The difference of cell membrane capacitance among these cell types, according to the single-shell dielectric model, enables separation of T- (or B-) lymphocytes from monocytes, T- (or B-) lymphocytes from granulocytes, and monocytes from granulocytes in a dielectrophoretic/gravitational field-flow fractionation device[18]. The same approach also demonstrates separation of cultured human breast cancer MDA-435 cells from normal blood cells [19].

Two magnetic approaches have been applied to blood cell separation in the microscale [20]. In one method, the difference of native susceptibility between

erythrocytes and other blood cells is exploited. The most paramagnetic cell in the body is the deoxygenated erythrocyte. The approximate 10^9 iron atoms carried by hemoglobin protein in each erythrocyte make the cell paramagnetic, unlike other cells in blood. Even in its oxygenated state, the erythrocytes are less diamagnetic than other blood cells. Both diamagnetic capture mode [21, 22] and paramagnetic capture mode [23] have been demonstrated. The other approach is a more general method using antibody conjugated magnetic beads. CD45-covered micro magnetic beads were used to label leukocytes and separate them from blood [24].

Several biomimetic microdevices have been demonstrated for cell separation or enrichment. A unique device based on the intrinsic features of blood flow in the microcirculation, such as plasma skimming and leukocyte margination, was proposed to separate leukocytes directly from whole blood [25]. 34-fold enrichment was achieved. In another study, a whole blood sample is forced to flow in a lattice of channels designed to mimic the capillary channels hydrodynamically. The leukocytes self-fractionate into the different types due to a combination of stretch-activated adhesion of cells with the walls, stochastic sticking probabilities, and hetero-avoidance between granulocytes and lymphocytes [26]. Chang et al. fabricated an array of square or slender offset pillars coated with E-selectin IgG chimera inside microfluidic channels to mimic physiological process of leukocyte recruitment to blood vessel walls. HL-60 and U-937 cells can be enriched or partially separated by interaction with the antibody-coated wall of the device [27].

Acoustic standing wave technology has been demonstrated for continuous particle separation in both macroscopic and microscopic domains [28]. It has been applied to

continuously separate particles from medium with high efficiency in microchips assembled by anisotropic etched silicon chamber with glass lid [29]. Separation of erythrocytes from lipid microemboli in whole blood has been reported. In this case, the width of the channel is chosen to correspond to half the ultrasonic wavelength, thereby creating a resonator between the side walls of the flow channel in which a standing wave can be formed. Lipid particles are collected in the pressure antinodes by the side walls and erythrocytes in the pressure node [30, 31].

More closed related to this work are examples that separate cells based on size. As shown in Table 1 and 2, the sizes of blood cells are different (leukocytes are larger than erythrocytes). Not shown in these tables is the fact that although there is a diameter overlap between erythrocytes and leukocytes (especially T lymphocytes), the volume of leukocytes is at least twice of that of a normal erythrocyte due to the biconcave disk shape of the erythrocyte [6]. Therefore, a separation of erythrocytes and leukocytes by size should use the 3D volume information as part of the criteria, instead of being based solely on the largest dimension of the cell. A microstep device fabricated on silicon was shown to separate microbeads of different sizes by physically blocking the larger one with the steps [32]. Recently there is a group of devices under the general name of hydrodynamic separators that separate particles continuously and passively based on the streamline theory inside microfluidic devices. Sturm's and Austin's groups designed a device with an asymmetric shifted pillar array and successfully demonstrated separation of microbeads in submicron sizes and DNAs of different lengths [33]. Later the technology was applied to blood cell separation as described later in this chapter [34, 35]. Seki's group demonstrated several designs of channel based hydrodynamic separators

[36–39]. In these devices, particles exit into multiple side branch channels determined by their center positions relative to the streamlines going into the side channels. Beads and cells of different sizes were separated inside the devices. Fluidic resistance calculation was used to calculate the fluidic width inside the main channel that goes into side channel, thus the critical particle sizes.

In the following sections of this chapter, two size-based hydrodynamic separators are presented. The pillar-shaped separator can separate particles with high resolution, while the channel-shaped separator reduces chip footprint significantly and has less requirement for flow control.

2.2 Pillar-shaped separator

2.2.1 Principle

The device is composed of a separation chamber filled by an array of cylindrical pillars as well as inlets and outlets. Each row of pillars has the same center-to-center distance λ and edge-to-edge distance d, and is staggered by a finite displacement from the previous row $\Delta\lambda$ (Fig. 2-1B). Because of small channel dimension (on the order of 10–100 μm) and flow rate (on the order of 0.01–1 μL/min), the Reynolds number ($<10^{-2}$) is in the laminar regime. Thus the flow inside the device can be treated as 2D laminar flow. For fully developed steady flow, each pillar has two stagnation points. The stagnation points of adjacent rows are rotated with respect to the net fluid flow direction because of the row shift. Separation lanes are defined by division lines, which are streamlines ending at stagnation points (Fig. 2-1C). The special property of the separation lines are such that spherical particles with mass centers at the left-hand side of

separation lines will flow from the left-hand side of the pillars, while particles at the right-hand side of separation lines will flow from the right-hand side. The critical separation size is defined as twice the minimum distance between the edge of pillar and the nearest division line. For a given geometrical design, there is one corresponding critical separation size.

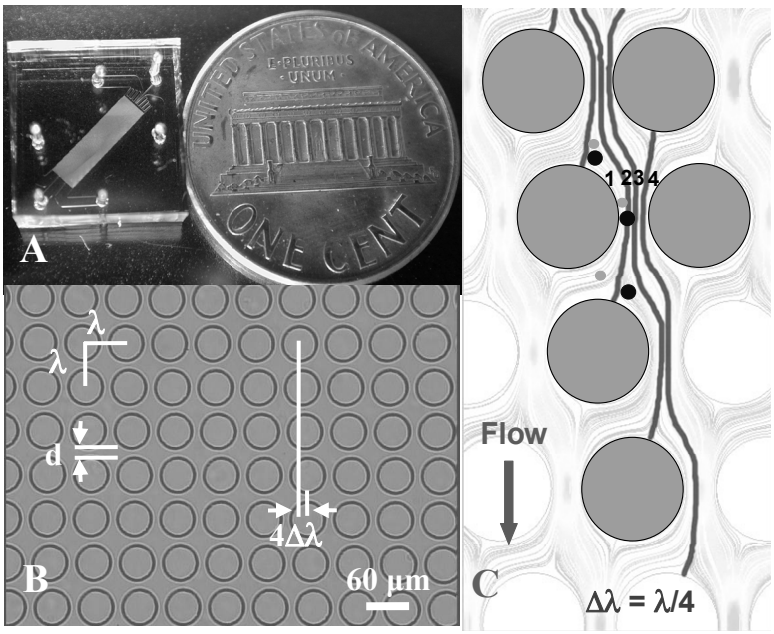

Figure 2-1 *Design of pillar-shaped separator. (A) Device for blood separation. (B) Detailed device structure with geometrics labeled. (C) A small particle moves in zigzag mode and a large particle moves in displacement mode with four separation lanes for* $\Delta\lambda=\lambda/4$.

When the particles are not interacting with walls, it is assumed they will not change the flow pattern and will follow the streamlines. The interactions between particles are also neglected for simplicity of the model. This is a good approximation for blood diluted over ten times, but might not be appropriate for undiluted blood. If the

diameter of a particle is smaller than the critical separation size, it can follow a separation lane exactly resulting in a zigzag flow pattern, which follows the net fluid flow direction over a long distance. On the other hand, if the diameter of a particle is larger than the critical separation size, it flows in displacement mode. The particle does not remain in one separation lane all the time, and changes between lanes as it is unable to make sudden turns around pillars. These particles flow diagonally and do not follow the net fluid flow direction.

2.2.2 Experiment

2.2.2.1 Material

PDMS (polydimethylsiloxane) (Sylgard 184) was obtained from Dow Corning, MI, USA. Polystryrene beads were purchased from Duke Scientific Corporations, CA, USA.

2.2.2.2 Device design and fabrication

PDMS is chosen for the device because of its blood compatibility and ease of use. Devices are fabricated with DRIE-silicon molds and mounted on a glass slide by overnight baking at 80 ℃ (Fig. 2-1A). The channel height is 20 μm. The effective separation area is 7 mm by 1.8 mm and consists of upstream and downstream regions. In each region, every consecutive row of obstacles is shifted horizontally by a fixed amount: 4 μm for upstream, 6 μm for downstream. In both regions, along each row, the center-to-center distance of obstacles, λ, is 60 μm, while the distance between them, d, is 14 μm. At inlet, the blood sample is introduced and focused by two sheath flows.

2.2.2.3 Device simulation

The flow pattern inside the device is simulated by solving a 2D incompressible Navier-Stokes equation with FEMLAB. No-slip boundary conditions are used for the device walls. Also assumed are parabolic velocity field profile at the inlet and zero pressure at the outlet. Fig. 2-2 shows the simulated streamlines for the modeled device. The colors are coded for magnitude of the velocity field. The critical separation size derived by simulation is 7.1 μm.

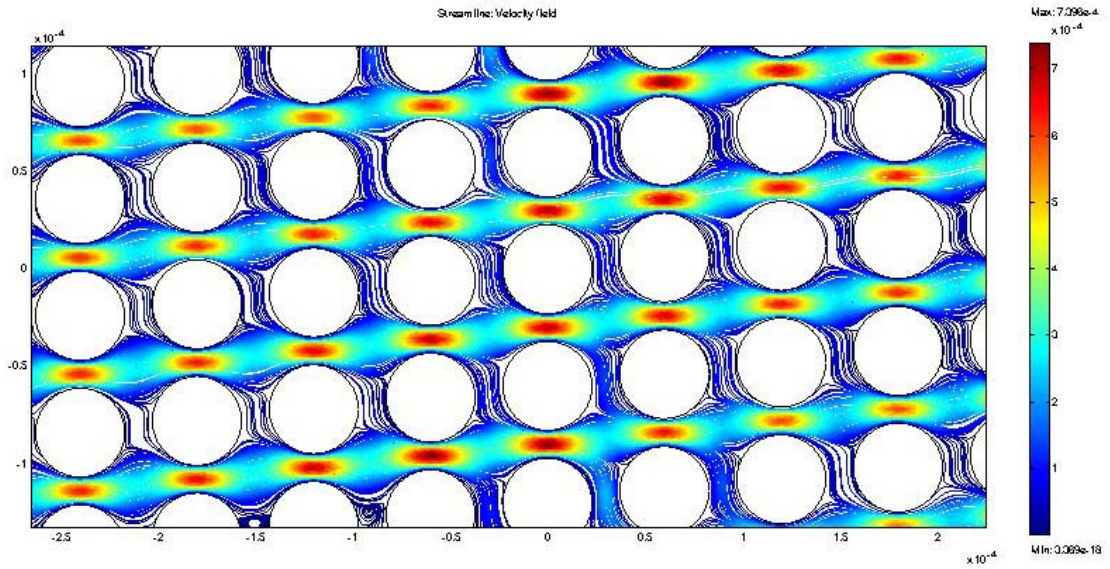

Figure 2-2 *2D Navier-stokes simulation with velocity field magnitude displayed.*

2.2.3 Results and discussion

2.2.3.1 Device calibration

Experimentally, the device was first calibrated with polystyrene beads. Fluids were pumped into devices with syringe pumps (Pico Plus, Harvard Apparatus, MA).

Central flow rate was kept at 0.2 μL/min and sheath flows were 1.2 μL/min. Bead concentrations were on the order of 10^3 /μL.

All beads 5 μm (green) or 7 μm (red) in diameter followed the "zigzag mode." In contrast, 10 μm (red) diameter beads followed the "displacement mode." Finally, the 8 μm diameter (clear) beads did not strictly follow either mode and exited between the 10 μ m and 7 μm beads (Figs. 2-3 and 2-4).

To accurately measure the critical separation size and obtain a separation function, fluorescent-labeled polystyrene beads (Duke Scientific, CA, USA) are used under different flow rates (Fig. 2-5). Flow rate was found to have little effect on separation profile. The bead size is not uniform. The measured size distribution of the beads is given in Fig. 2-6. The separation function is calculated by a table lookup operation Fig. 2-7. The S shape of the separation function proves the binary nature of the separation, validating the use of the device for sorting applications. The experimentally determined critical separation size is approximately 8 μm, which agrees well with the simulation result.

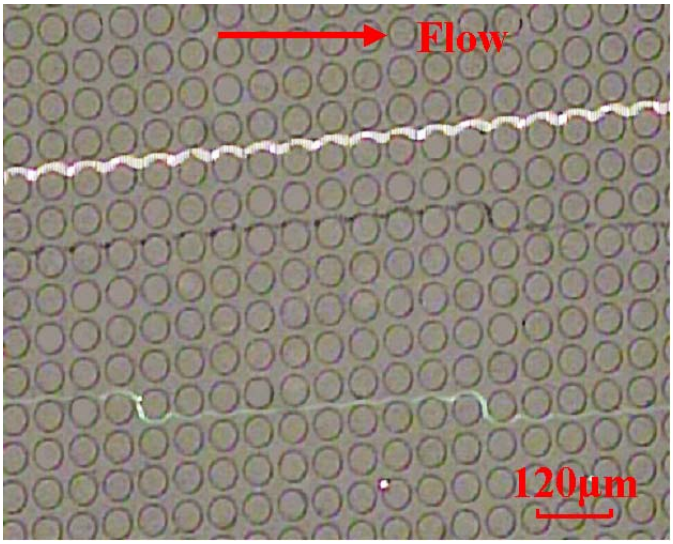

Figure 2-3 *Separation of 5 µm (green), 8 µm (clear), and 10 µm (red) beads*

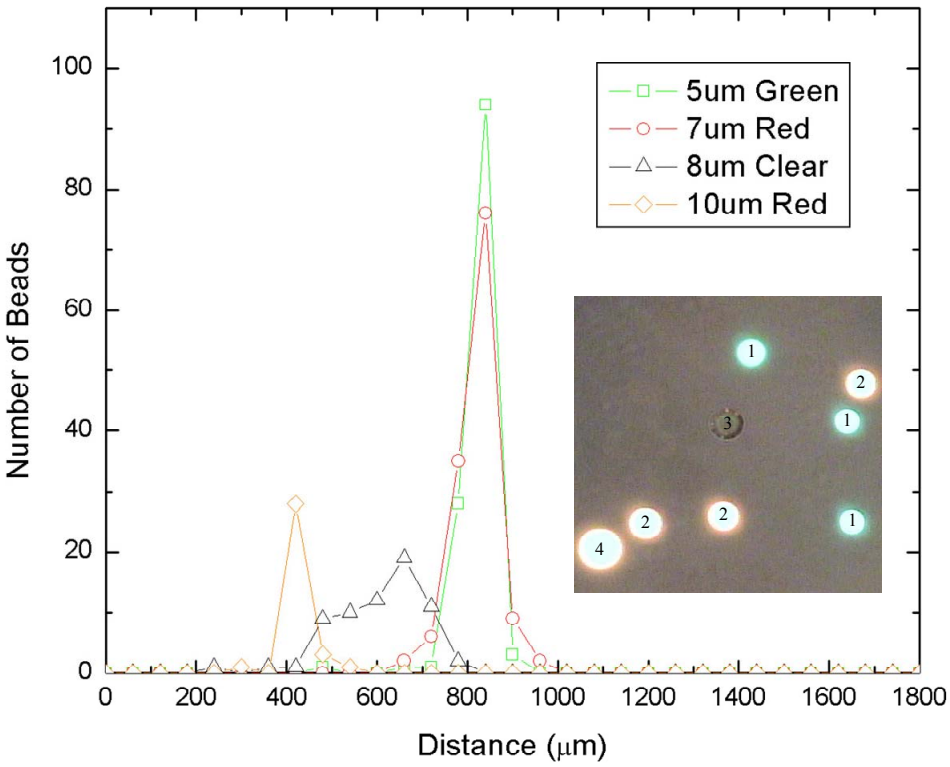

Figure 2-4 *Statistical analysis of bead separation. Inset is taken with fluorescent microscope. Beads with label 1, 2, 3, and 4 are 5 µm, 7 µm, 8 µm, and 10 µm in diameter, respectively.*

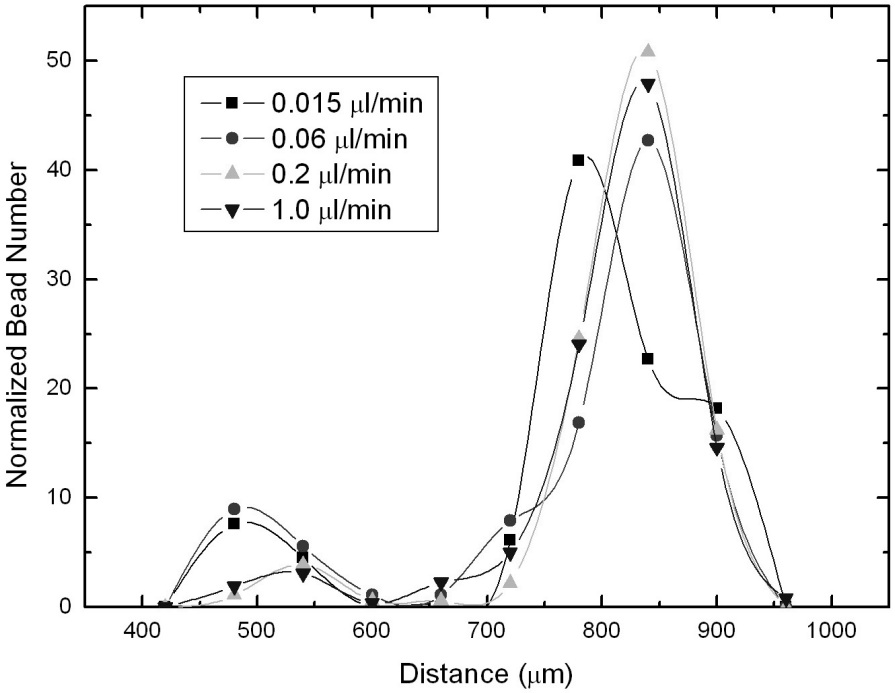

Figure 2-5 *Separation profiles under different flow rates*

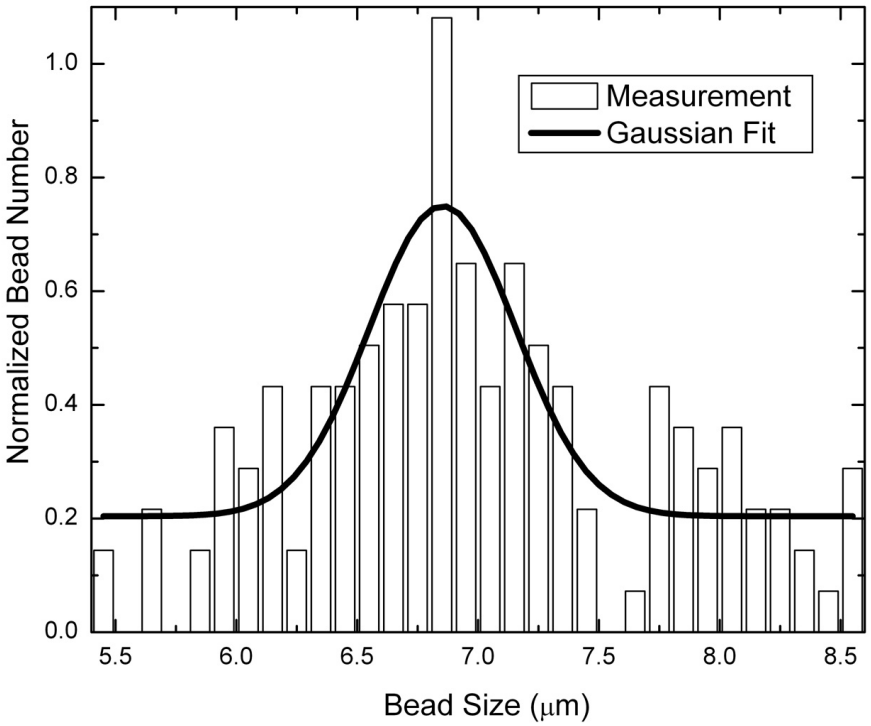

Figure 2-6 *Measurement of bead size distribution*

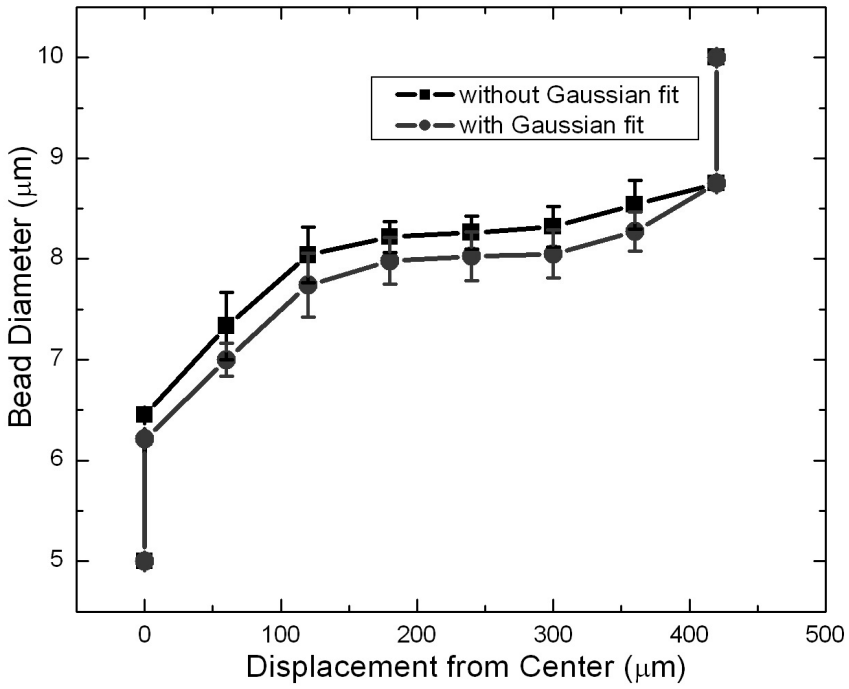

Figure 2-7 *Separation function curve*

2.2.3.2 Human blood cell separation

Human blood cell separation was then demonstrated using a blood fraction of concentrated leukocytes diluted with Ficoll-Paque Plus (Amersham Biosciences, Sweden). Leukocytes were concentrated by repetitive centrifugation at 1500 rcf (relative centrifugation force, equivalent to g) for 10 minutes at 4 ℃, then taking out the top layer of supernatant and the bottom layer of pellet. Ficoll-Paque Plus is a mixture of diatrizoate sodium and Ficoll 400. Ficoll 400 is a neutral, highly branched, hydrophilic polymer of sucrose. Traditionally it has been used as a reagent to purify lymphocytes from human peripheral blood based on density gradient centrifugation. The density of the mixture is 1.077 g/mL, which is closer to blood cell density than aqueous saline.

Diluting blood with Ficoll-Paque Plus enables us to run an experiment over one hour without severe sedimentation.

The use of a hemacytometer yielded a measured leukocyte-to-erythrocyte ratio of 1:43. As shown in Fig. 2-8, two groups of cells following different flow patterns were identified. Statistical analysis concluded that the ratio of cells traveling displacement to those traveling zigzag was 1:38 (Fig. 2-9), very consistent with the leukocyte-to-erythrocyte ratio.

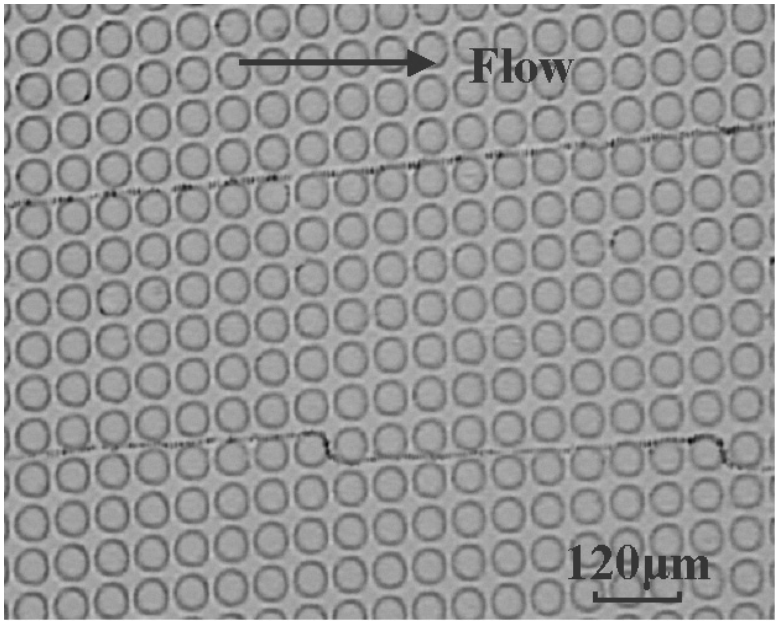

Figure 2-8 *Separation of leukocyte (top) from erythrocyte (bottom). Picture was generated by overlaying of multiple video frames.*

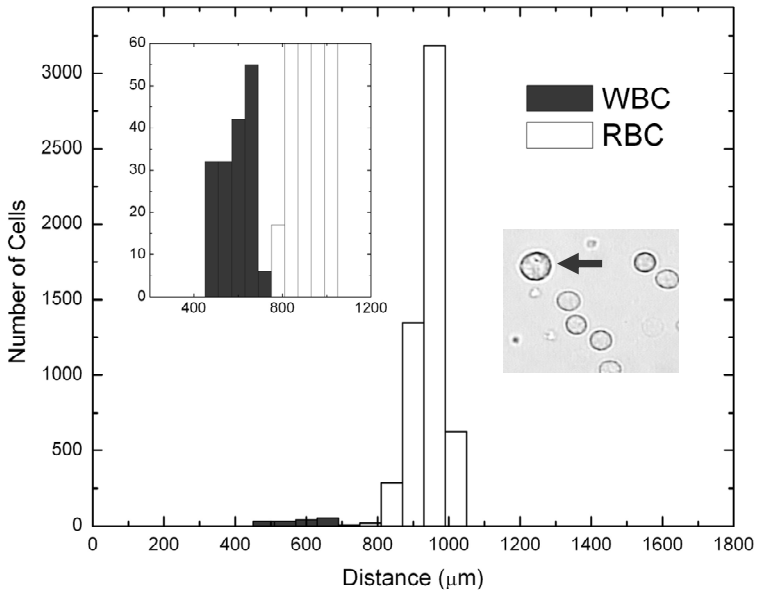

Figure 2-9 *Statistical analysis of separation of blood fraction of concentrated leukocytes. Left inset is a close up of leukocyte data. Right inset shows one leukocyte (arrow pointed) among erythrocytes.*

Tests were then performed using a sample of whole blood, diluted with Ficoll-Paque Plus. Because of the high erythrocyte-to-leukocyte ratio in natural blood, and limitations on flow rate and blood cell concentration, tests were run for over two hours in order to observe several leukocytes. Statistical analysis showed the ratio of cells traveling displacement to zigzag to be 1:502 (Fig. 2-10), which is in agreement with the known leukocyte-erythrocyte ratio. However, towards the end of such tests, several erythrocytes flowing in zigzag mode appeared in the lanes normally occupied by cells flowing in displacement mode. Such phenomena are believed to be caused by the increased amount of blood cells adhering to the obstacles after a long testing time.

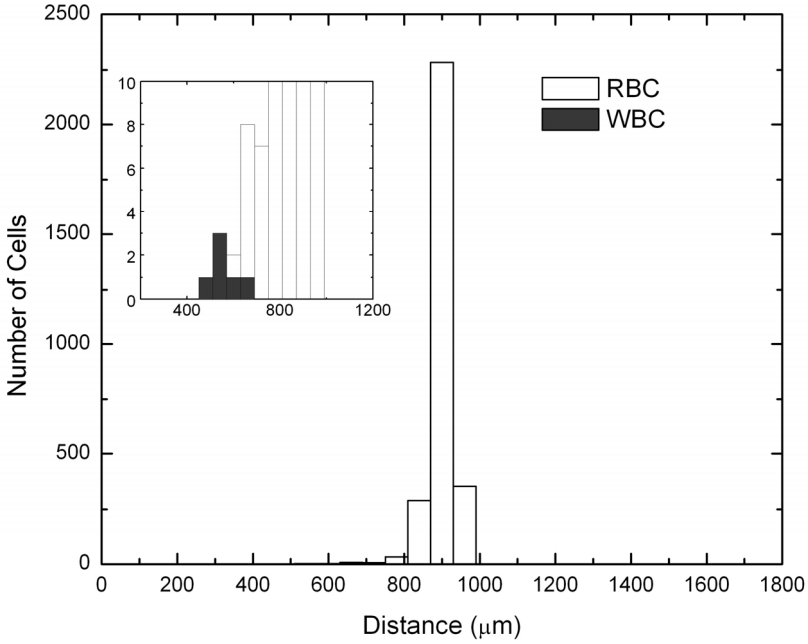

Figure 2-10 *Statistical analysis of separation of diluted whole blood sample. Inset is a close up of leukocyte data.*

To confirm that most leukocytes flow in displacement mode and estimate separation efficiency, we obtained leukocyte-rich plasma by gravity sedimentation of erythrocytes in Wintrobe tubes and stained the leukocytes with acridine orange (Molecular Probes, OR, USA), before resuspension in Ficoll-Paque Plus. Acridine orange is a nuclear fluorescent dye. Erythrocytes, which have no nucleus, do not fluoresce, only leukocytes are stained and fluoresce. Fig. 2-11 shows the separation profile. As expected, most of the leukocytes are found to flow in displacement mode (Fig. 2-11 inset). The fraction of leukocytes with displacements overlapping erythrocytes is 9%, indicating a small separation error or high leukocytes separation efficiency of 91%.

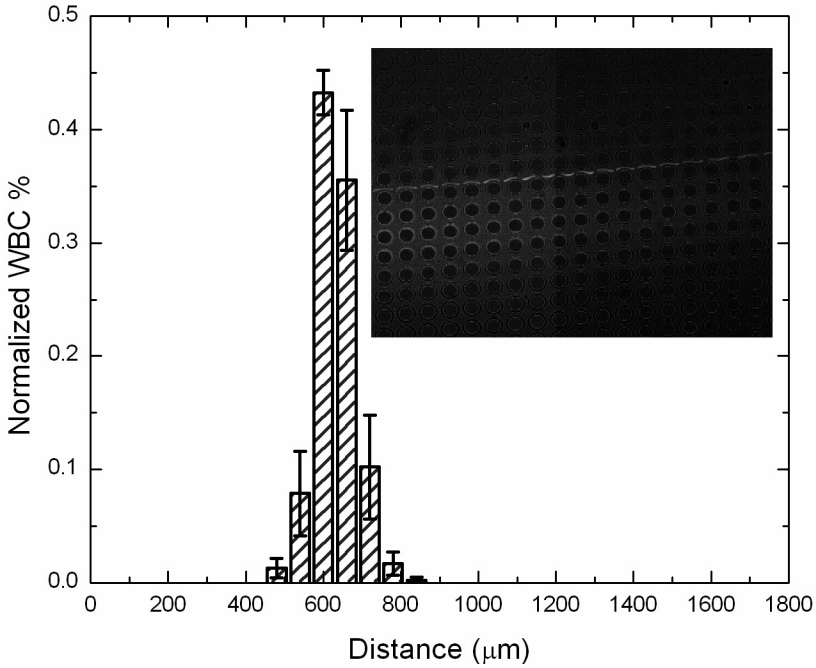

Figure 2-11 *Separation profile of stained leukocyte rich plasma. Insert is an event of leukocyte flow through the detection region.*

2.3 Channel shaped separator

2.3.1 Principle

The principle of the channel-shaped separator device is based on streamline engineering in the separation region. For the dimension of the device and the flow rate used in testing, the Reynolds number is on the order of 10^{-2}. The flow inside devices falls into the low Reynolds number laminar flow regime. Thus the center of particles can be assumed to follow streamlines of the fluidic field if there are no interactions between the particle and the channel wall, and the particle concentration is low enough that particle-particle interaction can be ignored. The separation principle of the device can be illustrated with a T-shape channel in which a side channel branches out from main channel (Fig. 2-12 top). In Fig. 2-12 bottom, the crossing region of the T-shape channel

is illustrated with 2D fluidic simulation of undisturbed streamlines. The flow is from right to left and top to bottom. A stagnation point can be identified, which is normally very close to the downstream vertex of the device wall. At this point, the flow has zero velocity. From this stagnation point, a division line can be drawn that separates the fluid region into two parts. The vertical distance between the division line and device wall at the upstream vertex of the side exit channel defines the critical particle size, R, for separation. The collection zone is defined by the area between the division line and the device walls, including the side channel.

As the first step, when particles flow into the crossing region of the T-shape channel, they are somehow forced to flow along the bottom channel wall, as in Fig. 2-12. When there is no interference from the wall, the particle will flow along the same streamline. The particle-device wall interaction might change the center of a particle to a new streamline. The particle may flow into main outlet or side channels without interaction with the downstream channel wall. If it collides with the downstream channel wall, the vertical component of the velocity vector at the center of the particle determines whether it goes into a side or the main outlet channel. For a particle whose radius is smaller than the critical particle size R, its center always stays inside the collection zone, thus it flows into a side channel. For a particle whose radius is larger than R, its center is above the division line at the upstream vertex and hence it never enters the collection zone afterwards.

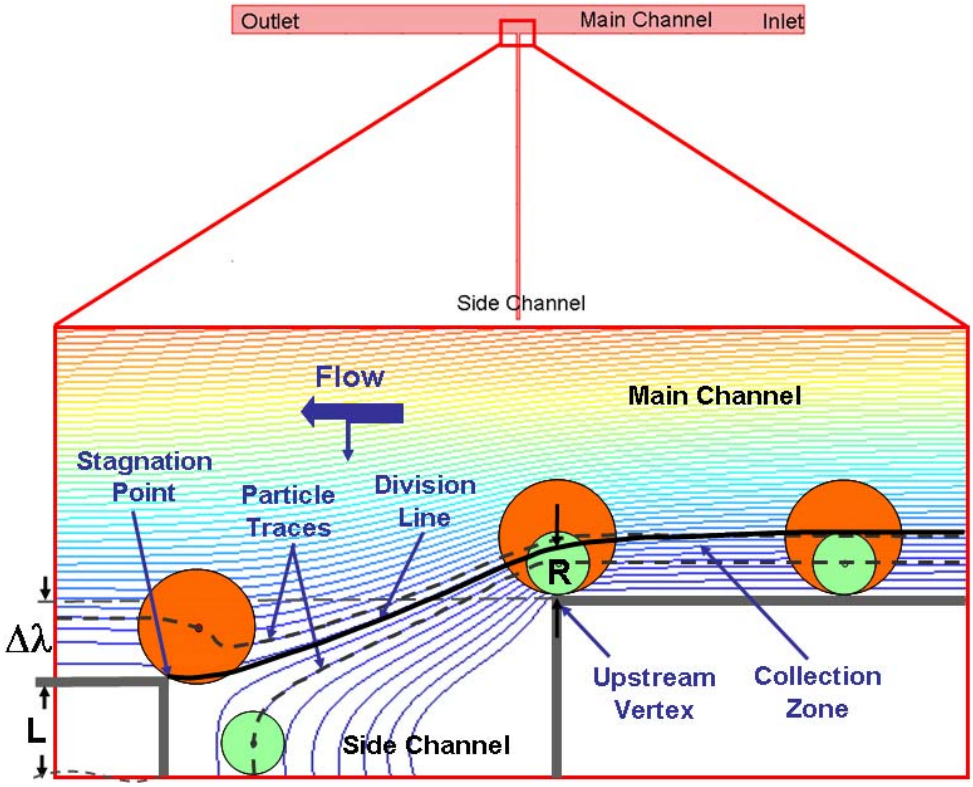

Figure 2-12 *Principle of channeled shaped separation. Top drawing shows the T-shape channel with crossing region labeled by a box. Bottom drawing is a detailed illustration of the boxed area. Background is 2D fluidic field simulation with color coded streamlines. The flow is from right to left, top to down. Stagnation point, division line and collection zone are labeled. Also labeled is the upstream vertex, where the critical particle size for separation R is defined. Length of side channel L and vertical distance between downstream and upstream vertices of side channel walls Δλ are shown. Traces of two particles with radius larger than R (orange color) and smaller than R (green color) are also illustrated with black dash lines.*

2.3.2 Simulation

The separation is determined by the critical particle size R. Two factors that can be used to control R were studied. The T-shape channel served as our model. The effects were studied by a 2D FEMLAB simulation of the Navier-Stokes equation. Aqueous solution was simulated as flowing inside the device. A parallel velocity profile with maximal velocity of 1 mm/sec was applied at the inlet. Zero pressure was used for outlets. The no-slip condition was assumed at the device walls. If not specified otherwise, 1000 μm was used as the channel length for the inlet channel, the main outlet channel, and side branching channels. 100 μm was used as the channel width for both the inlet and main outlet channel. 10 μm was used as the channel width of the side channels.

First, the effect of the length of side channel L is examined. As the solid line in Fig. 2-13 shows, increasing side channel length decreases critical particle size. This is caused by greater fluidic resistance in the side channel and hence a reduced flow rate in the side channel. For low Reynolds number flow in a long tube, the pressure difference is proportional to flow rate. The ratio of pressure difference and flow rate defines fluidic resistance. In 2D geometry, fluidic resistance can be expressed as

$$R = \frac{1}{12\mu}\frac{W^3}{L}$$

where W is channel width, L is channel length, and μ is fluid viscosity. The T-shape channel, the main inlet, main outlet, and side channel outlet were modeled as three resistors by applying the fluidic resistance equation. The fluidic resistance of the main outlet was in parallel with that of the side channel so the product of fluidic resistance and flow rate of the main outlet equals that of the side channel. From the flow rate ratio of

the main outlet and side channel, and assuming a parabolic flow profile of the velocity field in the main inlet, the width of fluid in the main inlet channel that went into the side channel was calculated. The result was plotted in Fig. 2-13 as a dash line. The values calculated with the fluidic resistance model were always larger than those obtained by simulation. This is because only at upstream far from the upstream vertex (where the critical particle size was defined) could the parallel velocity profile be assumed. Therefore, the critical particle size calculated by the fluidic resistance model was the distance between the division line and the main channel wall far upstream of the upstream vertex. This was confirmed by simulation. From the simulation, the distance measured between division line and main channel wall far upstream matched well with the results from the fluidic resistance calculation.

The other factor considered was the local geometry of the crossing region. In this case, the vertical distance between downstream and upstream side channel vertices $\Delta\lambda$ was used as a design parameter. As in Fig. 2-14, critical particle size R increased as $\Delta\lambda$ increased and was more sensitive when $\Delta\lambda$ was positive.

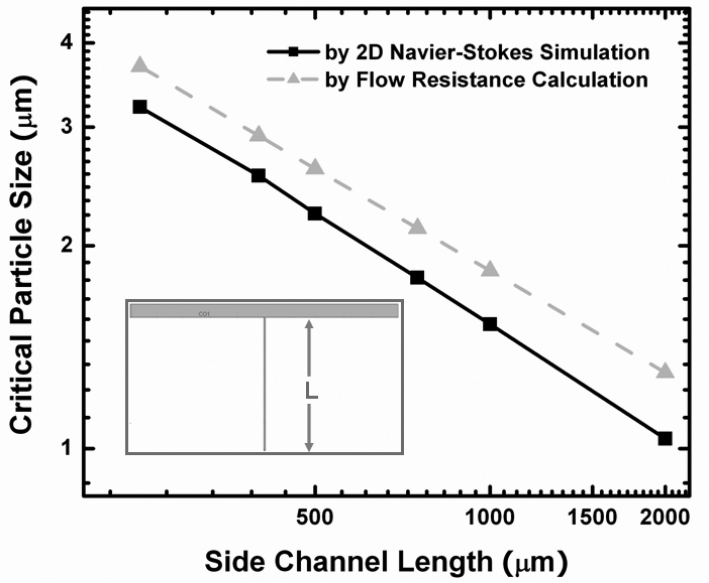

Figure 2-13 *Simulation study of the effect of side channel length L on critical particle size R. Solid line is 2D Navier-Stokes simulation results. Dash line is critical particle size calculated from flow resistance model.*

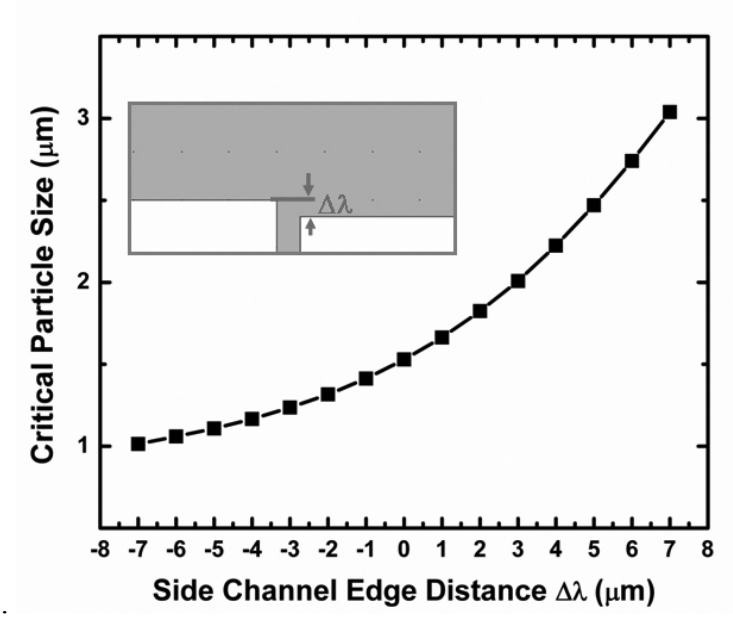

Figure 2-14 *Simulation study of the effect of side channel edge distance $\Delta\lambda$ on critical particle size R. Positive $\Delta\lambda$ is defined as inset.*

2.3.3 Device design

Two devices were designed, fabricated, and tested. For device I, only the effect of local geometry change was tested. Side channel length L was kept the same for all side exit channels, and only the vertical distances $\Delta\lambda$ of downstream and upstream vertices of side channels were changed. To optimize the device for blood cell separation, in device II, both L and $\Delta\lambda$ were changed to achieve a wider range of critical particle sizes.

The devices contained one sample inlet, one buffer inlet, one main outlet, and multiple side channel outlets (Fig. 2-15 and Fig. 2-16). Three side channels with the same local geometry were grouped into one downstream channel. There are eleven groups in device I and ten in device II. After sample flow met buffer flow, the sample flow was squeezed by the buffer flow in the pinch flow region. Relative flow rates were adjusted so that all particles in the sample flow pinched against the main inlet channel wall before they entered the separation region. The pinch flow region was 500 μm long so that the flow was stabilized before it entered the separation region. The separation region consisted of an array of side exit channels perpendicular to the main channel, each with a corresponding critical particle size.

The eleven groups of side exit channels on device I increased in $\Delta\lambda$ from -5 μm to 5 μm in 1 μm increments when considered from upstream to downstream. Simulation from the T-shape channel model predicted the critical particle size for each of them, as shown in Fig. 2-17. From side channel group numbers one to eleven, the critical particle size changes from 2.9 μm to 3.8 μm.

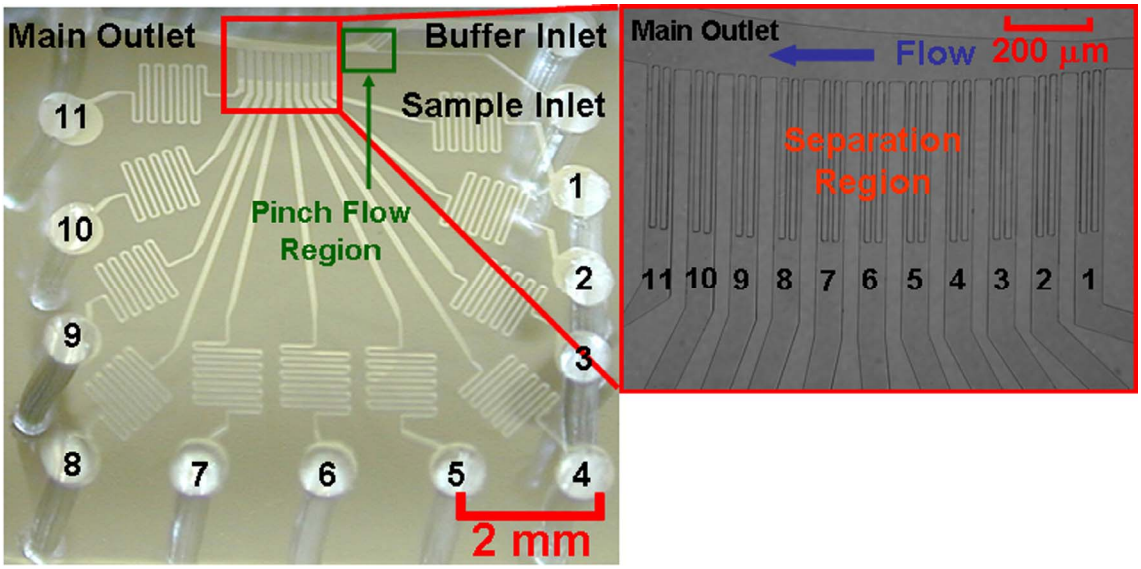

Figure 2-15 *Design of channel-shaped separation device I*

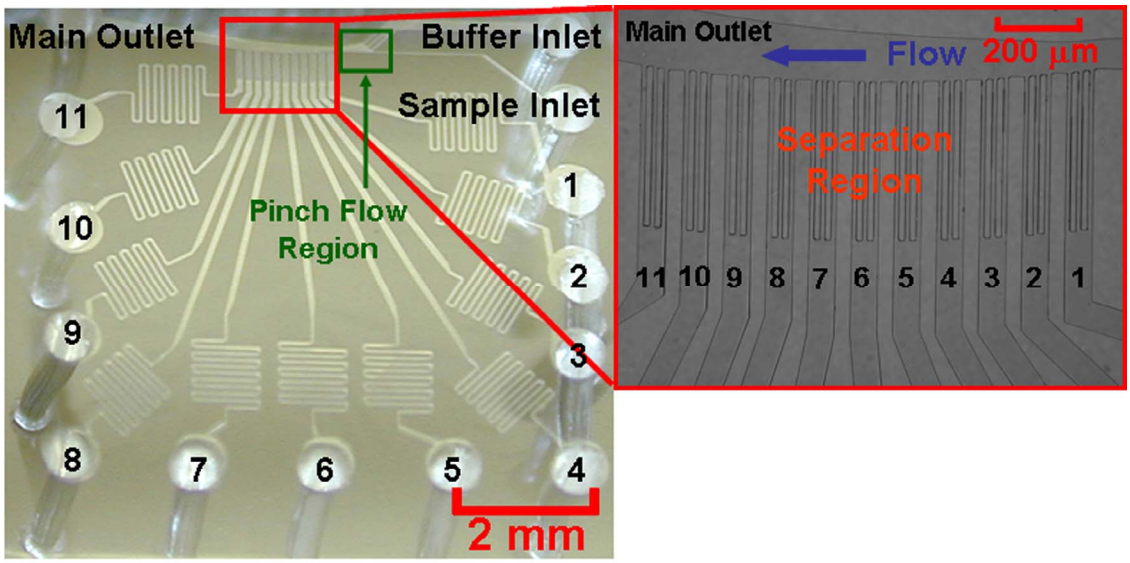

Figure 2-16 *Design of channe- shaped separation device II*

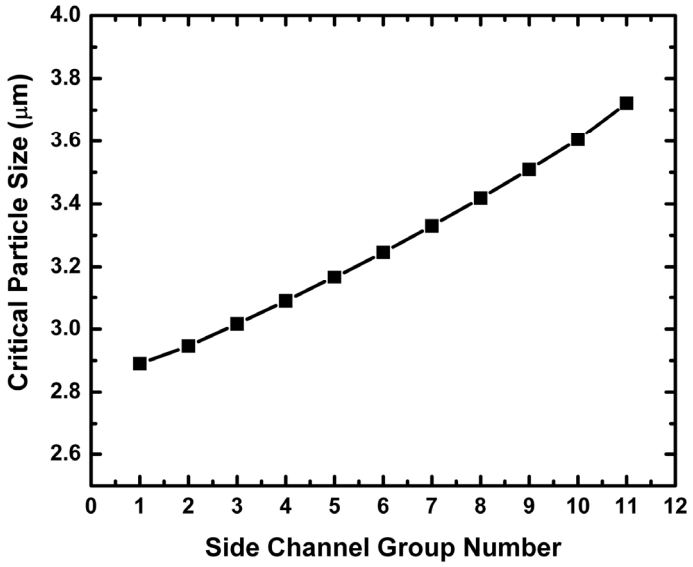

Figure 2-17 *Prediction of critical particle sizes for different side channel groups in device I*

To optimize the device for blood cell separation, a device with larger span of critical particle size is desirable. Erythrocytes average 8 μm in diameter and can range from 7 μm to 9 μm. Leukocytes have a wider range from 6 μm to 20 μm. The ratio of erythrocytes to leukocytes in whole human blood is in the magnitude of thousands to one. For device II, from upstream to downstream, $\Delta\lambda$ increases from 0 μm to 9 μm in 1 μm increments and the length of the exit channels decreases linearly from 22000 μm to 2200 μm in a -2200 μm increment. The critical particle sizes increase from upstream to downstream, as predicted by FEMLAB (Table 2-3). From side channel group 1 to 10, the critical particle size increases roughly exponentially. This is desirable, since the majority of the cells in blood fall into the lower size range. With this design, the separation is finer for smaller particles and rougher for large ones. Fig. 2-18 shows the fluidic simulation of the crossing regions of side channel 1, 6, and 10, overlaid with spherical

particles of radii from 1 μm to 10 μm. At the upstream vertex, where a particle loses its contact with the device wall, its center position is compared against the division line. The particle might flow into a side channel without interaction with the downstream device wall, as is the case for particles 1 and 2 in Fig. 2-18a. It might collide with the downstream vertex of the device wall as do particles 4 to 10 in Fig. 2-18a or the downstream device wall as do particle 3 in Fig. 2-18a, particles 4 and 5 in Fig. 2-18b and particle 10 in Fig. 2-18c. Depending on its center position relative to the division line, the particle will moved into the main channel or side channel. Particles 4 and 5 in Fig. 2-18b are interesting cases, where the particles collide with the side channel wall but the fluidic drag force moves them up into the main channel.

Table 2-3 Design parameters and predicted critical particle sizes for device II

Side Channel Group Number	*Side Channel Length L (μm)*	*Edge Distance $\Delta\lambda$ (μm)*	*Critical Particle Size R (μm)*
1	22000	0	2.28
2	19800	1	2.57
3	17600	2	2.88
4	15400	3	3.08
5	13200	4	3.54
6	11000	5	4.12
7	8800	6	4.79
8	6600	7	5.76
9	4400	8	7.39
10	2200	9	10.75

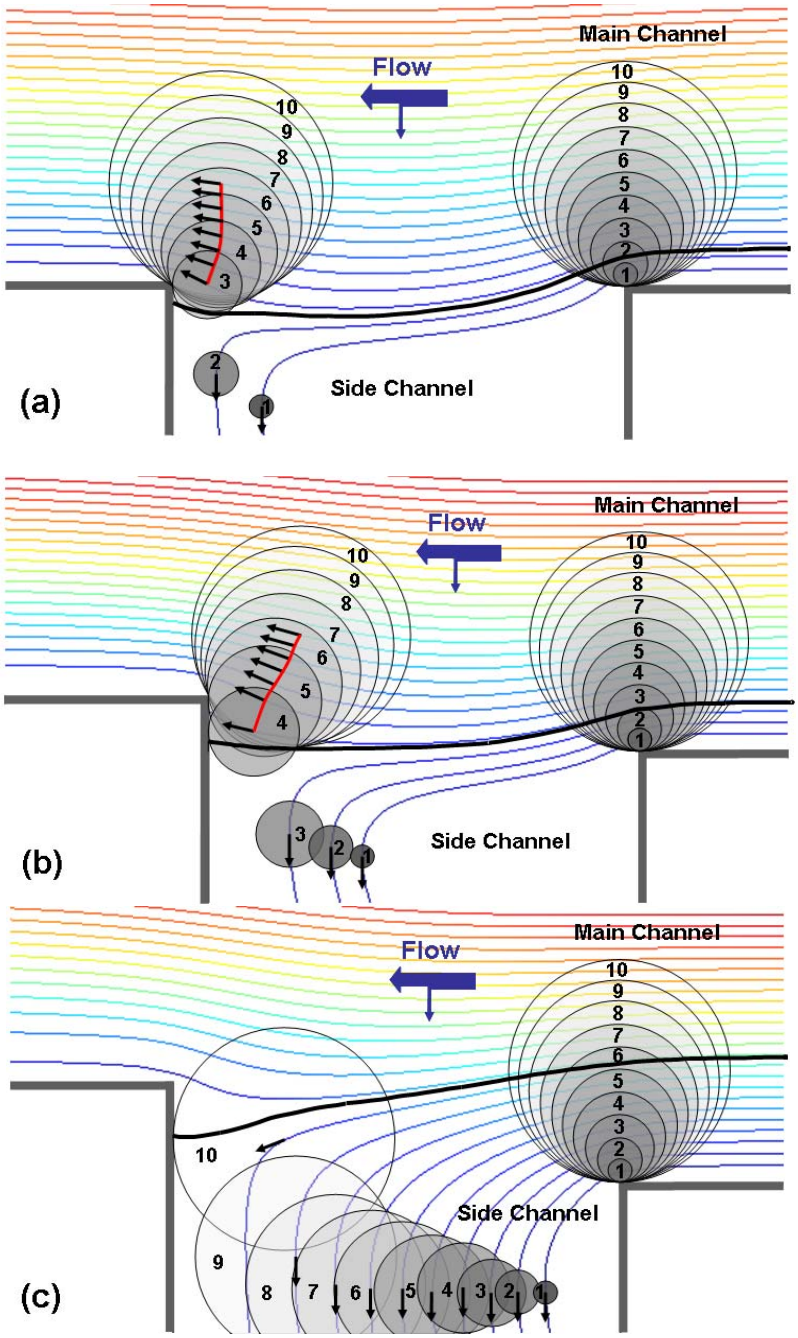

Figure 2-18 *2D fluidic simulation at the crossing region of side channels of device II. Spherical particles with radii from 1 μm to 10 μm with 1 μm increments were also drawn to illustrate their trajectories. Each particle is shown twice. One is at the moment when it is about to lose contact with the upstream vertex of the device wall. The other is when*

it is closest to the downstream device wall. The direction of the undisturbed velocity field at the center of the particle is labeled with an arrow. A: side channel number 1, B: side channel number 6, C: side channel number 10.

2.3.4 Fabrication and testing setup

2.3.4.1 Device fabrication

PDMS was chosen for the device because of its blood compatibility and ease of use. The mold for PDMS was fabricated by Deep Reactive Ion Etching (DRIE) on silicon wafer with photoresist AZ4620 as a mask. The channel height for device I is 40 μm and that of device II is 20 μm. HMDS (1,1,1,3,3,3-hexamethyldisilazane) was used to treat the mold before applying a homogenous mixture of PDMS part A and part B (10:1). PDMS was cured in the mold at 80 ℃ for 25 minutes. Then it was separated from the mold, cut into pieces, and holes were punched on each piece with a Luer stub adapter (gauge 20, Becton Dickinson, NJ, USA). PDMS pieces were then ultrasonically cleaned in acetone for 10 minutes, and rinsed with acetone, then IPA. Finally PDMS pieces were mounted on clean glass slides by overnight baking at 80 ℃.

2.3.4.2 Material

PDMS (polydimethylsiloxane) (Sylgard 184) was obtained from Dow Corning, Midland, MI, USA. Polystyrene beads were purchased from Duke Scientific Corporations, Fremont, CA, USA. Wintrobe tubes of 115 mm long and 3 mm inner diameter were purchased from Chase Scientific (R828B, Rockwood, TN, USA). Fresh human blood was obtained from healthy donors with anticoagulant EDTA added. Blood samples were used within 48 hours of withdrawal. Leukocyte-rich plasma was prepared

with Wintrobe tubes. One milliliter of bubble-free fresh whole blood was filled into the tube. The tube was laid on flat surface for thirty minutes to an hour. Then it was gradually tilted up to a vertical position. The upper, clear, plasma part was carefully transferred to a clean container.

2.3.4.3 Device calibration and testing setup

Calibration of device I and device II were accomplished with fluorescent polystyrene beads of 5 μm and 10 μm in diameter. Sample flow rate was kept at 0.06 μL/min, while buffer flow was in the range of 0.5–0.8 μL/min. The interface of the sample flow and buffer flow could be clearly observed under microscope. The buffer flow rate was adjusted so that a desirable flow profile of the interface was achieved. To minimize the effect of bead-to-bead interaction, total bead concentration was on the order of 100/μL.

Flows were introduced into the device by syringe pumps (pump 11 Pico Plus, Harvard Apparatus, MA, USA). The separation region of the device was observed under a fluorescent microscope (Nikon E800, Japan) during the whole testing period. A CCD camera (Spot RT slider, Diagnostic Instruments, MI, USA) was connected to the microscope and used to take videos. Videos were later analyzed frame by frame.

Human blood cell separation was demonstrated using a blood fraction of concentrated leukocytes diluted with Ficoll-Paque Plus (Amersham Biosciences, Sweden) in device II. Ficoll 400 is a neutral, highly branched, hydrophilic polymer of sucrose. Its density is 1.077 g/mL, which is closer to blood cell density than aqueous saline. Diluting blood with Ficoll-Paque Plus enables us to run an experiment over one hour without severe sedimentation. Human blood cells were prepared by the

sedimentation-based Wintrobe method. The erythrocyte portion was diluted 1500 times with Ficoll-Paque Plus.

2.3.5 Results and discussion

The result of separation of 5 μm and 10 μm beads in device I is summarized in Fig. 2-19. All 5 μm beads exit from side channel group number one to three, with number one capturing the most. This corresponds to $\Delta\lambda$ of -5 μm, -4 μm, and -3 μm, and the predicted critical particle size is in the range of 2.9 μm to 3.0 μm. Approximately 50% of 10 μm beads exit from the main outlet as predicted by the simulation of critical particle size; the rest flow into the side exit channels. Assuming side channels one to three are collection channels for 5 μm beads, and the rest of the exit channels are collection channels for 10 μm beads, the separation efficiency is 97% for device I. Bead counts were normalized for the efficiency calculation.

In device II, 5 μm green beads exit mainly from side channel groups one and two, which correspond to edge distances $\Delta\lambda$ of 0 μm and 1 μm, and side channel lengths L of 22000 μm and 19800 μm (Fig. 2-20). The predicted critical particle sizes were 2.28 μm and 2.57 μm, which matched well with the average radius of the particles. 10 μm red beads exit mainly from side channel groups nine and ten, which correspond to edge distances $\Delta\lambda$ of 8 μm and 9 μm, and side channel lengths L of 4400 μm and 2200 μm. The predicted critical particle sizes were 7.39 μm and 10.75 μm (Fig. 2-21). If 5 μm beads were assumed to exit from exit groups one to three and 10 μm beads from groups four to ten, a histogram of the separation profile showed the separation has an efficiency of 96% (Fig. 2-22).

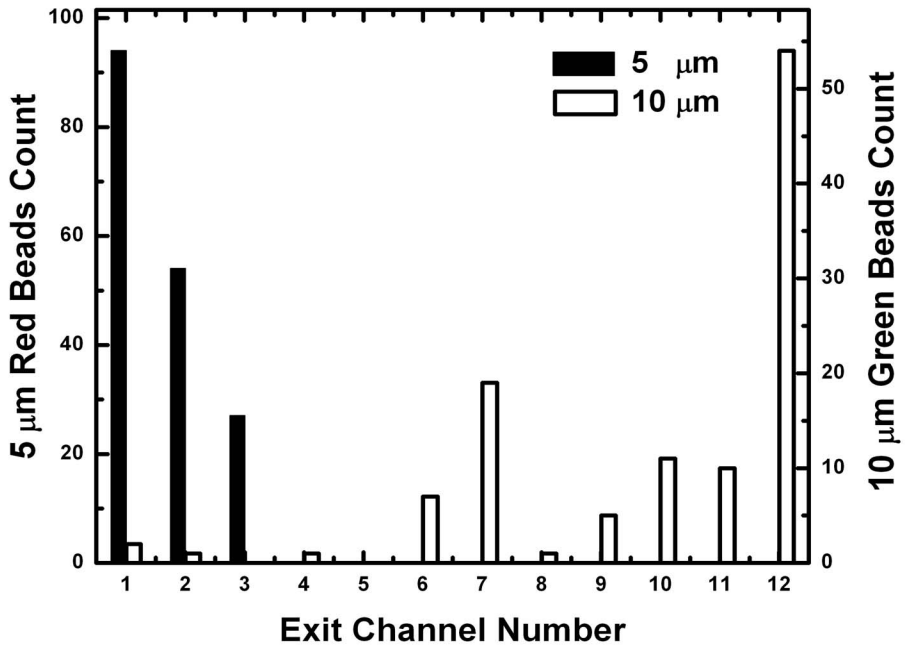

Figure 2-19 *Separation profile of 5 μm and 10 μm polystyrene beads in device I. Exit channels numbered 1 to 11 are side exit channels. Exit channel 12 is the main exit channel.*

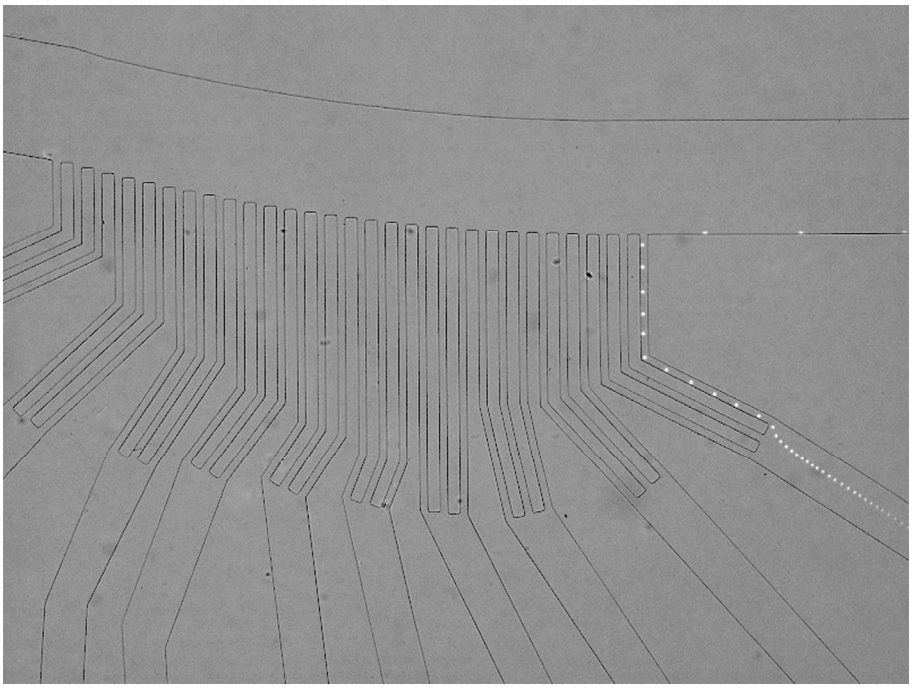

Figure 2-20 *Typical trace of 5 μm fluorescent polystyrene beads in device II*

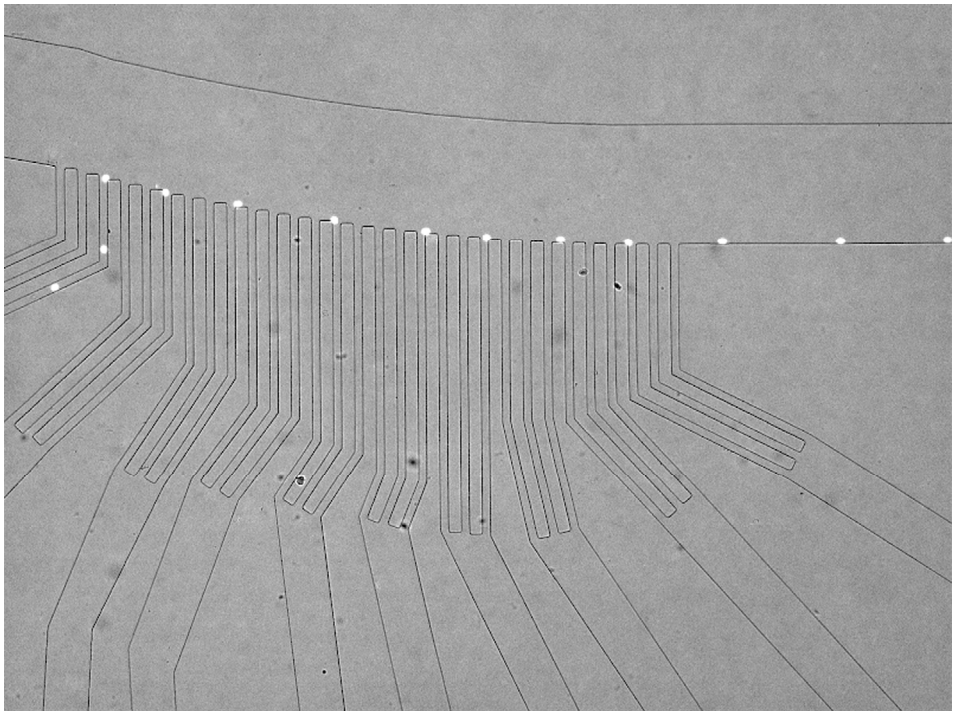

Figure 2-21 Typical trace of 10 μm fluorescent polystyrene beads in device II

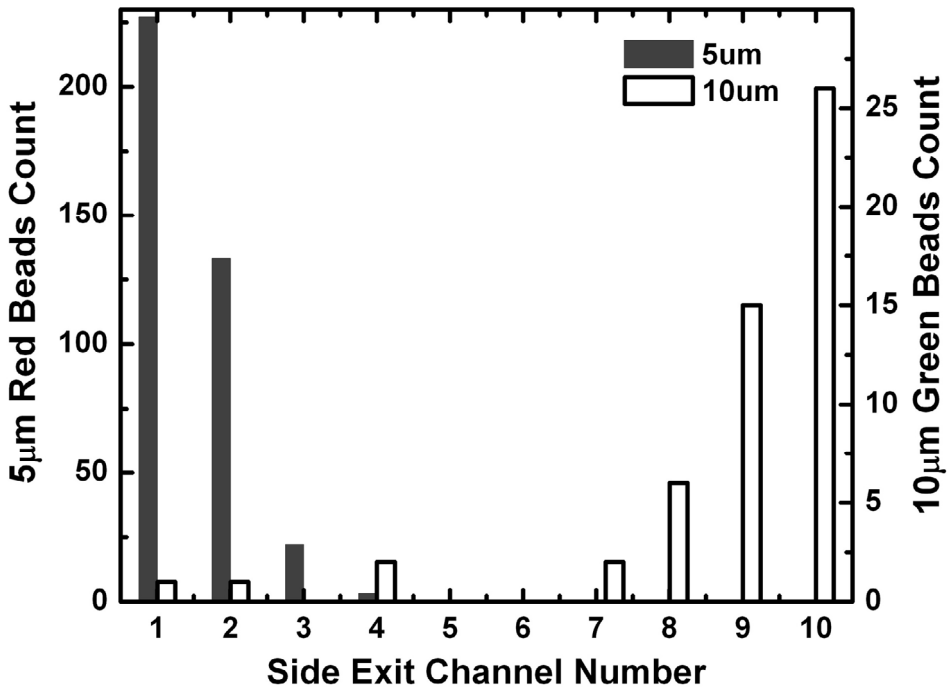

Figure 2-22 Separation profile of 5 μm and 10 μm beads in device II

There are some discrepancies between predicted critical particle sizes and the separation profile for large beads of 10 μm diameter. In device I, according to the simulation, all 10 μm beads should exit from the main outlet. However, in our experiments, about 50% of the large beads exit from side channel groups six to eleven. In device II, the simulation predicted most of the 10 μm diameter particles would exit from side channel group eight. However, in our experiments, they mainly exited from side channel group nine and ten. These discrepancies could be due to the coupling effect of side exit channels, which was not considered in T-shape simulation, and/or to the size variation of the 10 μm beads (up to 15%). Other factors, such as flow fluctuation caused by syringe pumps, adhesion of particles to the device wall, and the difference between 2D fluidic simulation and 3D device operation could contribute to the discrepancies. In general, device II demonstrated a better separation profile for 10 μm particles. In that device, the step sizes of critical particle sizes for larger particles are larger, and so are the error tolerances.

For both devices, it was observed under the microscope that the 10 μm beads flow in a "jumping" mode in the separation region: they move towards the stagnation points close to the downstream vertexes and slow down. After passing these stagnation points, they quickly flow toward the next side exit channel. Also observed were cases like particles 4 and 5 in Fig. 2-18B, where the beads collided with the side channel wall, but were moved up by surrounding fluid and entered back into the main channel to exit.

Erythrocyte and leukocyte separation from diluted human blood was performed with device II. Erythrocyte behavior inside the device was studied with whole human blood diluted one thousand times. Erythrocytes exited mainly from exit channel groups

two and three (Fig. 2-23). To study leukocyte flow inside the device, leukocyte-rich plasma was prepared with a final concentration of leukocytes in the range of 102/μL and an enrichment factor of leukocytes to erythrocytes in the tens to hundreds range. Leukocytes were stained with the fluorescent cell nucleus dye, acridine orange. Since erythrocytes do not contain nuclei, only leukocytes are stained by acridine orange. As shown in Fig. 2-24 and 2-25, the leukocytes demonstrated a different separation profile than the erythrocytes. Not shown in Fig. 2-25, one leukocyte exiting from the main outlet during testing was also observed.

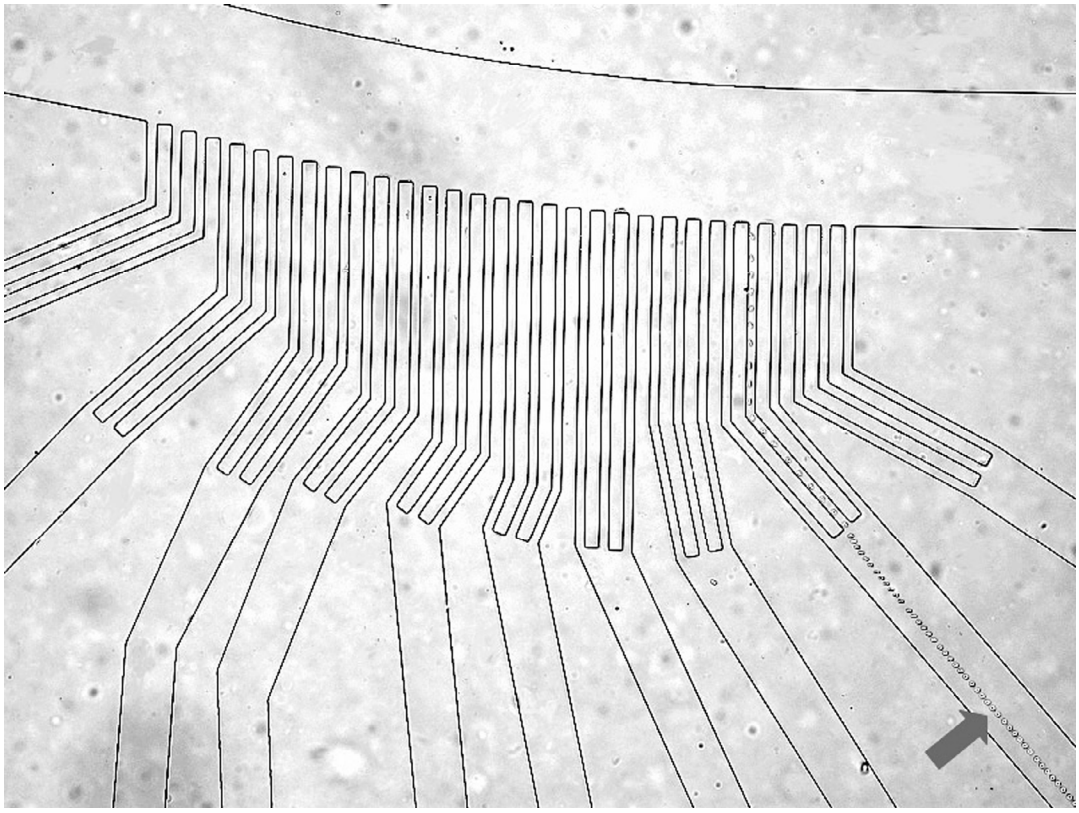

Figure 2-23 *Typical trace of erythrocyte in device II as pointed by arrow. Images were extracted from video with bright field illumination and then overlaid.*

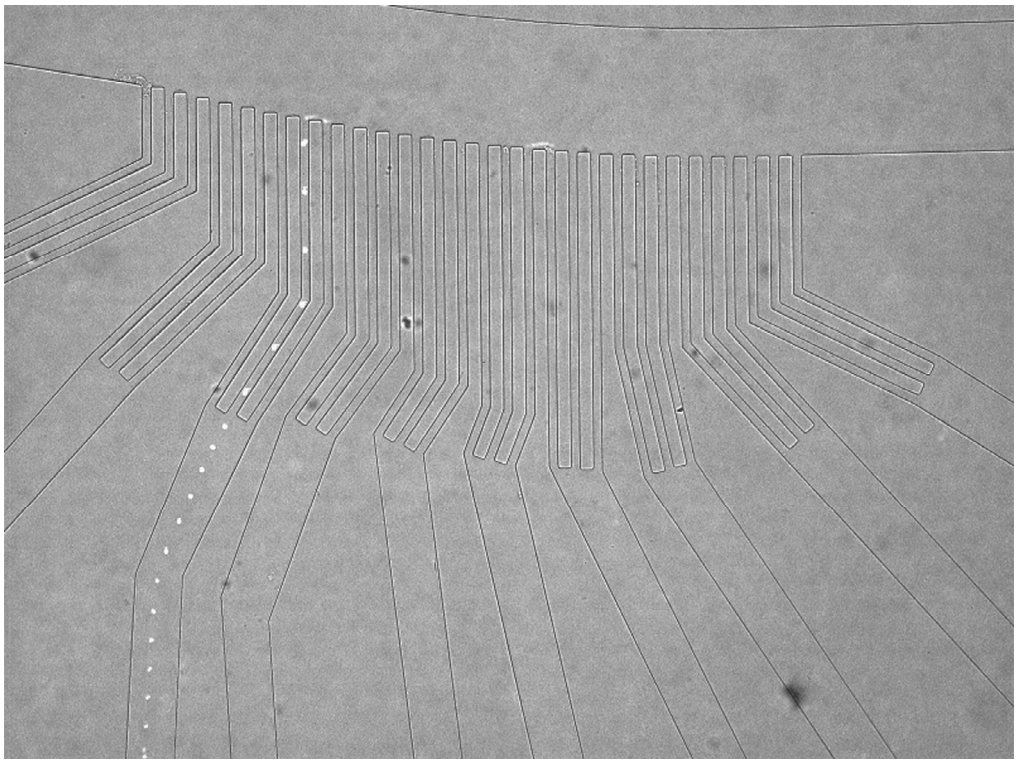

Figure 2-24 *Typical trace of leukocyte in device II. Images were extracted from video with both bright field and Epi fluorescent illumination and then overlaid.*

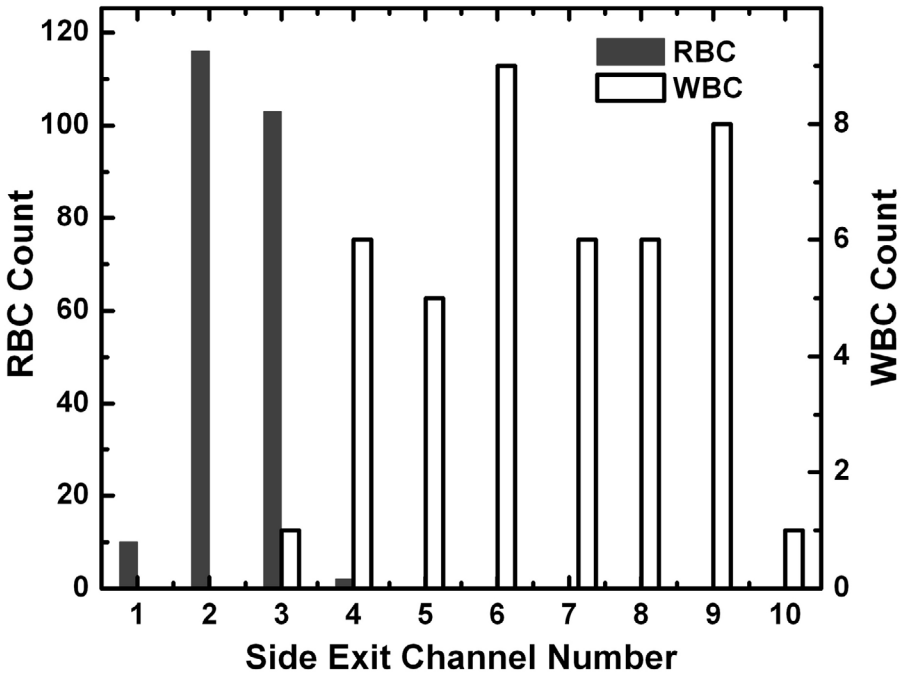

Figure 2-25 *Separation profile of erythrocytes and leukocytes in leukocyte- rich plasma*

If a line was drawn between exit groups three and four with the assumption that erythrocytes exited from group numbers one to three and leukocytes exited from the rest, a separation efficiency of 97% was achieved, meaning that with inputting equal numbers of erythrocytes and leukocytes, over 97% of the cells in exit groups one to three are erythrocytes, and the same for leukocytes in exit groups four to ten. The portion of the separation profile where erythrocytes and leukocytes did not separate very well was likely caused by the size overlap between erythrocytes and small lymphocytes. Although the volume of average small lymphocytes is at least twice that of erythrocytes [40, 41], the size is the determinant factor for the separation inside this device. Diameters of erythrocytes are reported between 7.5 to 8.5 μm, while those of small lymphocytes between 6 to 9 μm [1, 4, 6]. On the other hand, because of the biconcave disk shape of erythrocytes, their heights range from 1.5 to 3.0 μm, which are substantially smaller than the average diameter of small lymphocytes. Therefore, the separation of erythrocytes and small lymphocytes inside the device depends heavily on the orientation of erythrocytes in the separation region. In testing, a large percentage of erythrocytes with the flat portion of the disk shape aligned to the device wall were observed before they entered the separation region. It will be beneficial to increase device height so that the shear stress of fluid can align the erythrocytes along the device wall and the comparison of their heights to critical particle size will determine into which side channel they flow.

There are several benefits offered by these devices. The filtering effect of the device was achieved by the collection zone formed by the fluidic field, not by physical size limitation. Also this filtering effect was in the direction perpendicular to flow direction. These greatly reduce clogging. The separation regions of the devices had a

very small footprint of 1.5 mm by 0.8 mm. Setting up fluidic resistance of the side channels could take up a lot of chip space. Local geometry design of the separation region and reducing the effective cross-section area of the side exit channels could reduce the required length of side channels. Particles of different sizes were collected in different reservoirs that connected to side channels. This could facilitate further characterization of the particles. The solvent of sample flow went into upstream side channels. This means larger particles, which exited from downstream side channels or the main outlet, flowed out with the solvent in the buffer flow, which made solvent change for larger particles possible.

Flow control could be a problem for the operation of the device. Stable fluidic fields are required. Disturbance from pumps, particle adhesion to device walls, and particle-fluid and particle-particle interactions could change the local flow and thus change the separation profile. A multiple port injector structure was designed in the buffer flow inlet, so that the buffer flow channel was wide and the flow was stable and laminar. Another problem for device operation was particle adhesion to the device wall, which degraded device performance, especially in testing with leukocyte-rich plasma. Plasma protein could build up on the device surface. Platelets and blood cells were observed to adhere to the device wall gradually. This process is related to the freshness of the blood sample. For fresh blood withdrawn within 24 hours, it could take more than one hour before significant biomass built up inside the device under our testing conditions. For aged blood samples older than three days, the effect showed up within half an hour of device operation. Surface treatment and dynamic coating could improve the situation.

2D Navier-Stokes fluidic dynamics simulation was used for critical particle size prediction in device design. From Fig. 2-13, even in cases where only the lengths of side channels change, using simulation was more accurate than using a fluidic resistance model for critical particle size prediction. This was because the critical particle size was determined by local streamlines at the crossing region, which is closely related to the local geometrical design. This is not considered in the fluidic resistance model. For devices with local geometry variations ($\Delta\lambda$), streamline-based design with simulation has to be used to predict the critical particle sizes. Although the testing results later showed a good match between 2D fluidic simulation and testing results, the 3D nature of the channels may have some effects on particle separation. Ideally for very deep channels, the parallel velocity profile of the fluid and the resultant shear stress will keep particles of similar size in the same layer of fluid. This can make the flow effectively 2D. Making high-aspect ratio channels could be a problem in device fabrication, and in our PDMS on glass devices, the aspect ratio is under two.

Assuming a particle follows the same streamline in low Reynolds number laminar flow is a simplification used in our design. The actual particle trajectory is more complicated. The flow shears on the particles, the rotation of particles, and the non-spherical shapes of particles contribute to the transverse lift acting on particles [42]. In the case of blood cells, they have been reported to be kept away from capillary walls [43].

2.4 Conclusion

Two types of microdevices were designed and demonstrated to separate erythrocytes and leukocytes from diluted blood sample based on sizes. The

hydrodynamic separation is continuous, passive, and highly efficient. Assuming the particles in the size range of one micron to tens of microns move along the streamlines in the laminar flow devices, a streamline theory was developed to successfully predict the critical particle separation size.

For the pillar-shaped devices, separation of leukocytes from erythrocytes based on deterministic lateral displacement principle was demonstrated. Fluorescent beads of 5 μm, 7 μm, 8 μm, and 10 μm were successfully separated. Simulation of 2D laminar flow inside the device calculates velocity field and predicts the critical separation size for the current design to be 7.1 μm. The critical particle size for separation was shown to be around 8 μm experimentally, which could be used for rough separation of blood cells. The ratio of blood cells following displacement mode to those in zigzag mode matches with the leukocyte-to-erythrocyte ratio. Labeled leukocyte experiments confirm the separation of the two groups of cells is actually mainly erythrocytes and leukocytes. The efficiency for leukocyte separation is about 91%.

For the channel-shaped devices, a streamline-based design of microfabricated devices was presented to achieve particle separation by size. 2D Navier-Stokes simulation was used to predict the critical particle size for separation, which was the parameter that determined the binary nature of the separation. Two devices were designed and fabricated. Both of them separated 5 μm and 10 μm diameter polystyrene beads efficiently. The second device also demonstrated effective separation of human erythrocytes and leukocytes. It had a wider range of critical particle sizes with finer separation for small particles. This made it better suited for human blood cell separation.

2.5 Bibliography

[1] S. B. McKenzie, *Clinical Laboratory Hematology*. Prentice Hall, 2004.

[2] H. M. Shapiro, *Practical flow cytometry*, 4th ed. Hoboken, New Jersey: John Wiley & Sons, Inc., 2003.

[3] H. L. Kasdan, *personal communication*, 2004.

[4] Y. C. Fung, *Biomechanics: mechanical properties of living tissues*, *2nd ed*. New York: Springer-Verlag, 1993.

[5] C. E. Lentner, *Geigy Scientific Tables*. Basle, Switzerland: Ciba-Geigy, 1981.

[6] H. M. Shapiro, E. R. Schildkraut, R. Curbelo, C. W. Laird, R. B. Turner, and T. Hirschfeld, "Combined Blood-Cell Counting And Classification With Fluorochrome Stains And Flow Instrumentation," *Journal Of Histochemistry & Cytochemistry*, vol. 24, pp. 396–411, 1976.

[7] G. P. Gupta and J. Massague, "Cancer metastasis: Building a framework," *Cell*, vol. 127, pp. 679–695, 2006.

[8] E. Racila, D. Euhus, A. J. Weiss, C. Rao, J. McConnell, L. Terstappen, and J. W. Uhr, "Detection and characterization of carcinoma cells in the blood," *Proceedings Of The National Academy Of Sciences Of The United States Of America*, vol. 95, pp. 4589–4594, 1998.

[9] "Stem Cells: Scientific Progress and Future Research Directions," National Institute of Health, 2007.

[10] P. Popescu, H. Hayes, B. Dutrillaux, and R. Popescu, *Techniques in Animal Cytogenetics*. Springer, 2000.

[11] *Ficoll-Paque plus for in vitro isolation of lymphocytes*. Uppsala, Sweden: Amersham Biosciences, 2001.

[12] G. Vona, C. Beroud, A. Benachi, A. Quenette, J. P. Bonnefont, S. Romana, A. Munnich, M. Vekemans, Y. Dumez, B. Lacour, and P. Paterlini-Brechot, "Enrichment, immunomorphological, and genetic characterization of fetal cells circulating in maternal blood," *American Journal Of Pathology*, vol. 160, pp. 51−58, 2002.

[13] G. Vona, A. Sabile, M. Louha, V. Sitruk, S. Romana, K. Schutze, F. Capron, D. Franco, M. Pazzagli, M. Vekemans, B. Lacour, C. Brechot, and P. Paterlini-Brechot, "Isolation by size of epithelial tumor cells—A new method for the immunomorphological and molecular characterization of circulating tumor cells," *American Journal Of Pathology*, vol. 156, pp. 57−63, 2000.

[14] J. T. Kemshead, "Immunomagnetic manipulation of hematopoietic cells: a review of current technology," *J Hematotherapy*, vol. 1, pp. 35−44, 1992.

[15] J. C. Giddings, "Field-Flow Fractionation—Analysis Of Macromolecular, Colloidal, And Particulate Materials," *Science*, vol. 260, pp. 1456−1465, 1993.

[16] Y. Jiang, M. N. Myers, and J. C. Giddings, "Separation behavior of blood cells in sedimentation field-flow fractionation," *Journal Of Liquid Chromatography & Related Technologies*, vol. 22, pp. 1213−1234, 1999.

[17] J. Yang, Y. Huang, X. J. Wang, X. B. Wang, F. F. Becker, and P. R. C. Gascoyne, "Dielectric properties of human leukocyte subpopulations determined by electrorotation as a cell separation criterion," *Biophysical Journal*, vol. 76, pp. 3307−3314, 1999.

[18] J. Yang, Y. Huang, X. B. Wang, F. F. Becker, and P. R. C. Gascoyne, "Differential analysis of human leukocytes by dielectrophoretic field-flow-fractionation," *Biophysical Journal*, vol. 78, pp. 2680−2689, 2000.

[19] J. Yang, Y. Huang, X. B. Wang, F. F. Becker, and P. R. C. Gascoyne, "Cell separation on microfabricated electrodes using dielectrophoretic/gravitational field flow fractionation," *Analytical Chemistry*, vol. 71, pp. 911−918, 1999.

[20] D. W. Inglis, R. Riehn, J. C. Sturm, and R. H. Austin, "Microfluidic high gradient magnetic cell separation," *Journal Of Applied Physics*, vol. 99, 2006.

[21] K. H. Han and A. B. Frazier, "Continuous magnetophoretic separation of blood cells in microdevice format," *Journal Of Applied Physics*, vol. 96, pp. 5797−5802, 2004.

[22] K. H. Han and A. B. Frazier, "Diamagnetic capture mode magnetophoretic microseparator for blood cells," *Journal Of Microelectromechanical Systems*, vol. 14, pp. 1422−1431, 2005.

[23] K. H. Han and A. B. Frazier, "Paramagnetic capture mode magnetophoretic microseparator for high efficiency blood cell separations," *Lab On A Chip*, vol. 6, pp. 265−273, 2006.

[24] D. W. Inglis, R. Riehn, R. H. Austin, and J. C. Sturm, "Continuous microfluidic immunomagnetic cell separation," *Applied Physics Letters*, vol. 85, pp. 5093−5095, 2004.

[25] S. S. Shevkoplyas, T. Yoshida, L. L. Munn, and M. W. Bitensky, "Biomimetic Autoseparation of Leukocytes from Whole Blood in a Microfluidic Device," *Analytical chemistry*, vol. 77, pp. 933−937, 2005.

[26] R. H. Carlson, C. V. Gabel, S. S. Chan, R. H. Austin, J. P. Brody, and J. W. Winkelman, "Self-sorting of white blood cells in a lattice," *Physical Review Letters*, vol. 79, pp. 2149–2152, 1997.

[27] W. C. Chang, L. P. Lee, and D. Liepmann, "Biomimetic technique for adhesion-based collection and separation of cells in a microfluidic channel," *Lab on Chip*, vol. 5, pp. 64–73, 2005.

[28] T. Laurell, F. Petersson, and A. Nilsson, "Chip integrated strategies for acoustic separation and manipulation of cells and particles," *Chemical Society Reviews*, vol. 36, pp. 492–506, 2007.

[29] A. Nilsson, F. Petersson, H. Jonsson, and T. Laurell, "Acoustic control of suspended particles in micro fluidic chips," *Lab On A Chip*, vol. 4, pp. 131–135, 2004.

[30] F. Petersson, A. Nilsson, C. Holm, H. Jonsson, and T. Laurell, "Separation of lipids from blood utilizing ultrasonic standing waves in microfluidic channels," *Analyst*, vol. 129, pp. 938–943, 2004.

[31] F. Petersson, A. Nilsson, C. Holm, H. Jonsson, and T. Laurell, "Continuous separation of lipid particles from erythrocytes by means of laminar flow and acoustic standing wave forces," *Lab On A Chip*, vol. 5, pp. 20–22, 2005.

[32] S. Vankrunkelsven, D. Clicq, K. Pappaert, G. V. Baron, and G. Desmet, "A novel microstep device for the size separation of cells," *presented at microTAS 2004*, Malmo, Sweden, 2004.

[33] L. R. Huang, E. C. Cox, R. H. Austin, and J. C. Sturm, "Continuous particle separation through deterministic lateral displacement," *Science*, vol. 304, 987, 2004.

[34] J. A. Davis, D. W. Inglis, K. J. Morton, D. A. Lawrence, L. R. Huang, S. Y. Chou, J. C. Sturm, and R. H. Austin, "Deterministic hydrodynamics: Taking blood apart," *Proceedings of the National Academy of Sciences*, vol. 103, 14779–14784, 2006.

[35] S. Zheng, R. Yung, Y. C. Tai, and H. Kasdan, "Deterministic lateral displacement MEMS device for continuous blood cell separation," *presented at 18th IEEE International Conference on Micro Electro Mechanical Systems (MEMS2005)*, Miami Beach, Florida, USA, 2005.

[36] J. Takagi, M. Yamada, M. Yasuda, and M. Seki, "Continuous particle separation in a microchannel having asymmetrically arranged multiple branches," *Lab on a chip*, vol. 5, 778, 2005.

[37] M. Yamada, M. Nakashima, and M. Seki, "Pinched flow fractionation: Continuous size separation of particles utilizing a laminar flow profile in a pinched microchannel," *Analytical chemistry*, vol. 76, 5465, 2004.

[38] M. Yamada and M. Seki, "Microfluidic particle sorter employing flow splitting and recombining," *Analytical Chemistry*, vol. 78, pp. 1357–1362, 2006.

[39] M. T. Yamada and M. Seki, "Hydrodynamic filtration for on-chip particle concentration and classification utilizing microfluidics," *Lab on a chip*, vol. 5, 1233, 2005.

[40] S. Bensasso, D. Patinkin, N. B. Grover, and F. Doljansk, "Electrical Sizing Of Particles In Suspensions.4. Lymphocytes," *Journal Of Cellular Physiology*, vol. 84, pp. 205–214, 1974.

[41] M. A. Vandilla, M. J. Fulwyler, and I. U. Boone, "Volume Distribution And Separation Of Normal Human Leucocytes," *Proceedings Of The Society For Experimental Biology And Medicine*, vol. 125, pp. 367-ff., 1967.

[42] E. E. Michaelides, "Review—The transient equation of motion for particles, bubbles, and droplets," *Journal Of Fluids Engineering—Transactions Of The ASME*, vol. 119, pp. 233–247, 1997.

[43] P. A. Aarts, S. A. van den Broek, G. W. Prins, G. D. Kuiken, J. J. Sixma, and R. M. Heethaar, "Blood platelets are concentrated near the wall and red blood cells, in the center in flowing blood," *Arteriosclerosis, Thrombosis, and Vascular Biology*, vol. 8, 819–824, 1988.

CHAPTER 3

ELECTRICAL IMPEDANCE SENSING FOR BLOOD COUNT

3.1 Introduction

3.1.1 Coulter principle

Electrical impedance sensing has been used to measure biological materials, such as tissue samples and cell suspensions, for over a hundred years [1, 2]. Based on the Coulter counter principle, electrical impedance sensing has been one of the preferred technologies for particle sensing and counting. The Coulter counter was invented by Wallace H. Coulter in the late 1940s [3] and the first U.S. patent was secured in 1953. Since then, it has undergone extensive improvements (Fig. 3-1), including adding AC impedance sensing in addition to DC resistance sensing; automatic parallel sample

handling; improving sensitivity, specificity, and efficiency of WBC differential; and improving reliability of quality control.

The Coulter principle is illustrated in Fig. 3-2. Two fluidic chambers are separated by an aperture. The size of the aperture is comparable to the size of the particles (e.g., beads, biological cells, pollens) to be sensed. The particle is forced to flow from one chamber to the other. At the same time, the system impedance is measured by a pair of electrodes placed in each of the two chambers. The small feature size of the aperture makes it the dominant part of the system impedance. As a particle travels through the aperture, the impedance change is recorded. Therefore, the existence of the particle and some of its properties (e.g. volume, cell membrane capacitance) can be determined. Later, the initial DC resistance sensing was extended to AC impedance sensing [2].

Miniaturization can potentially improve device performance. The resistance change can be increased by reducing the size of the sensing region (aperture) of the sensor. In DC or low frequency AC (f < 100 kHz) cases, assuming a uniform electrical field in the sensing region, spherical particles, a cylindrical aperture, and ignoring electrical resistance inside the chambers from aperture to electrode, the resistance change ΔR is:

$$\Delta R = 2\rho\left\{\frac{\arctan\left(r\Big/\sqrt{R^2-r^2}\right)}{\pi\sqrt{R^2-r^2}}-\frac{r}{\pi R^2}\right\}, \qquad (3.1)$$

where r represents the radius of the particle, R the radius of the aperture, and ρ the resistivity of the medium. As shown in Fig 3-3A, shrinking the aperture dimension

greatly increases the resistance change, which is proportional to the signal being sensed. Fig3-3B shows that the channel resistance changes more significantly when the size of the particle is approaching the size of a given aperture of fixed size.

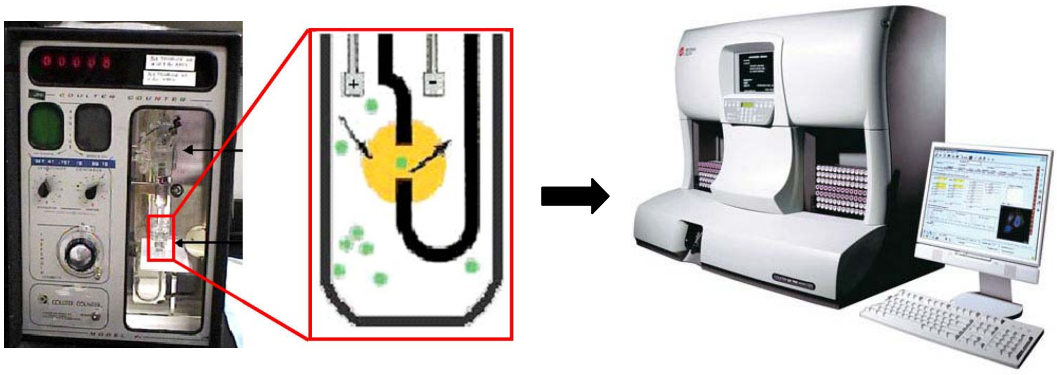

Figure 3-1 *Conventional automated hemacytometers. Left picture is one of the earliest models of DC Coulter counter (Coulter Electronics, Inc.). Right picture is a modern model (COULTER® LH780) with full automation for complete blood count (Beckman Coulter, Inc., 2006).*

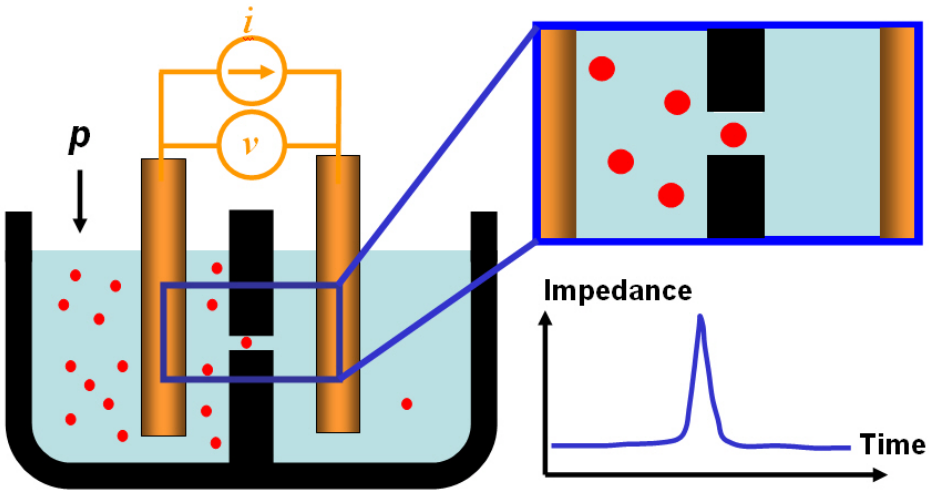

Figure 3-2 Principle of Coulter counter

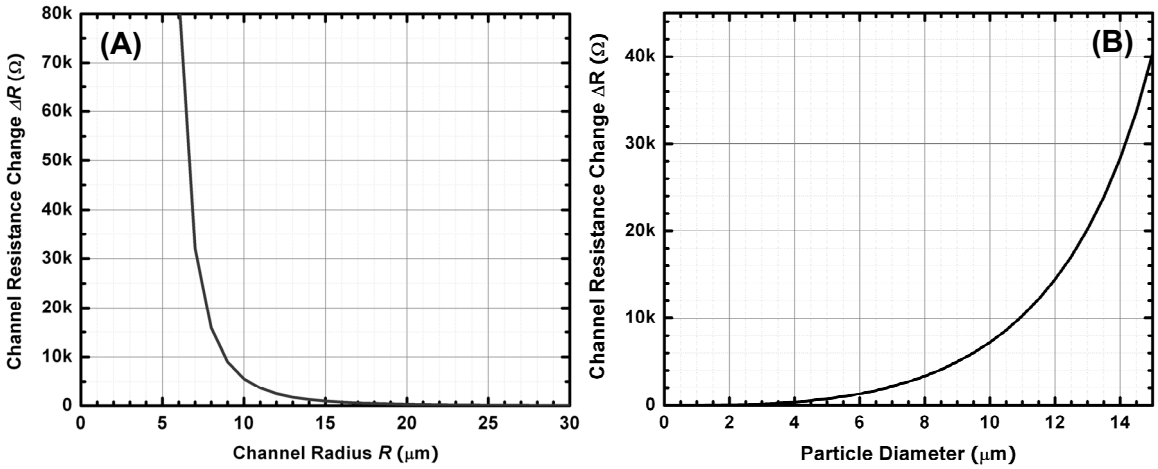

Figure 3-3 *Relationship of channel resistance change to channel radius and particle diameter. (A) Channel resistance change of the same particle (particle radius 5 μm) in devices of different size, assuming electrolyte resistivity of 0.83 Ωm. (B) Channel resistance change of particles of difference sizes in the same device, assuming aperture across section area of 280 μm^2 and electrolyte resistivity of 0.83 Ωm.*

Another benefit of miniaturization is reducing the error rate caused by the coincidence effect. The coincidence effect, when two or more particles flow through aperture at the same time, can be modeled by a Poisson process. The relationship of true count N and observed count n is:

$$n = \frac{V}{\Delta V}(1 - e^{-\frac{\Delta V}{V}N}), \qquad (3.2)$$

where V is the sample volume and ΔV is the aperture volume. Reducing the dimension of the sensing zone improves the error rate greatly, as shown in Fig. 3-4.

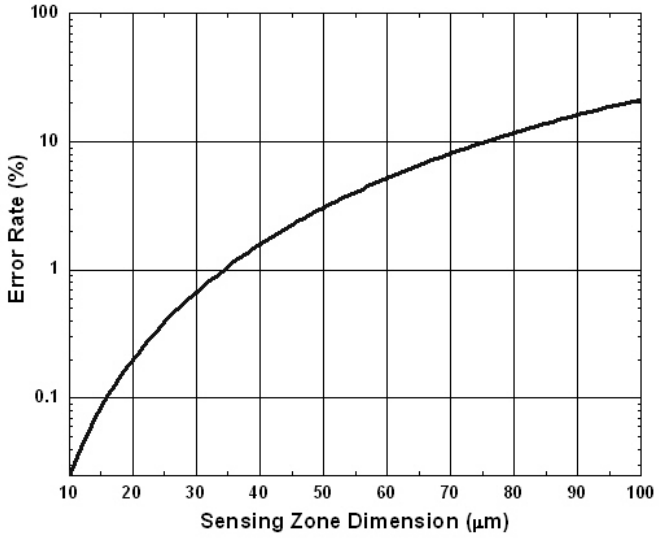

Figure 3-4 *The relation between error rate and sensing zone dimension, assuming cubic sensing zone, sample volume 500 μL and true count 250,000. The error rate is defined as (n-N)/N×100%.*

3.1.2 Cellular model for impedance response

Traditionally when biological tissues and cell suspensions are measured over a frequency range of 1 Hz to 10 GHz with a parallel plate capacitive sensor or its derivatives, three distinct dispersions, or relaxations, are found in an idealized case of dielectric spectra. α-dispersion, which is under a few kHz, is normally due to the double-layer effect of the electrodes, and is believed to originate from the displacement of counter ions surrounding charged membranes. β-dispersion, which is between 100 kHz and 10 MHz, is due to the interfacial polarization of the insulating plasma membrane surrounding the cells. Above 1 GHz, there is γ-dispersion, which results from reorientation of water molecules. Between the β- and γ-dispersions there may be small dispersions resulting from relaxation of biopolymers and bound water [2, 4].

A single biological cell can be modeled either by the single-shell model or one of the composite-cell models. The single-shell model assumes the cell is bound by a plasma membrane and that the interior of the cell is homogeneous. It has been successfully applied to mammalian erythrocytes, which have organelles, a complicated cytoplasm structure, and no cell nucleus [5]. Composite-cell models include additional material layers inside the plasma membrane. For example, a double-shell model has been used to model a large membrane bound cell nucleus in lymphocytes [6], while a double-shell model with vesicles has been used to model additional vacuoles and chloroplasts of plant cells [7]. Measurement of single-cell impedance spectra by electromechanical methods such as dielectrophoresis or electrorotation shows that at low AC frequency (under 100 kHz) the signal is determined mainly by the cell volume, while at higher frequency (100 kHz to 10 MHz), the intracellular structures also contribute to the overall measured impedance and become explorable measurands [3].

3.1.3 Problem of double-layer impedance for microdevices

The principle of impedance particle sensing relies on the momentary change of electrical impedance as particles replace electrolyte in the sensing zone. This impedance change is measured by a pair of electrodes separated by the aperture. This measurement allows for the determination of the presence of a biological cell and provides information on some of its properties. Traditional electrical impedance sensors, however, require a large electrode area to reduce the electrode-electrolyte interface (double-layer) impedance and allow the channel impedance (including electrolyte impedance and particle impedance) to dominate the overall impedance. Macroscopic blood counters, for example, use macro-electrodes, such as platinum wires, to measure the impedance change

across an aperture whose size is in the range of hundreds of microns. However, this presents a major difficulty associated with *micro* impedance sensing. The double-layer impedance, in series with the channel impedance, is inversely proportional to the electrode surface area so downsizing of the electrode area unavoidably increases its impedance and reduces the overall sensitivity [8, 9]. This problem is more serious in the low-frequency range, where the double-layer capacitance dominates over the channel impedance. In the high-frequency range, the parallel stray capacitance resulting from nonideal isolation between electrodes dominates the system impedance. Hence, the system impedance is not sensitive to channel impedance change in either the low or high frequency range. Only in some intermediate frequency range will the channel impedance be the dominate component in the system impedance.

3.1.4 Previous implementation of micro electrical impedance sensors

For micro DC Coulter sensors, several groups have attempted to solve the large double-layer impedance problem by using very large thin-film electrodes [10], macroscopic gold pin electrodes [11], or nonpolarizable Ag/AgCl electrodes [12]. For micro AC impedance sensors, the double-layer impedance is reduced at a high exciting frequency. Unfortunately, there is an upper limit on the operation frequency imposed by the stray capacitance between sensing electrodes, which results from coupling and non-ideal isolation. So to study particles with AC impedance sensing, the device is limited to a frequency range which is high enough to bypass electrode double-layer impedance and low enough that the stray capacitance does not play a significant role in overall system impedance [13]. One way is to increase the electrode surface area to reduce the double-layer impedance so that the sensing can be performed at a lower AC frequency. H. E.

Ayliffe and his coworkers demonstrated AC impedance measurement of cell suspensions and trapped cells with very thick (4 μm) electroplated gold microelectrodes [14]. In this chapter, electroplated platinum black on microelectrode surface is shown to reduce double-layer impedance by two orders of magnitude. With these electrodes, human blood cell sensing with a high signal-to-noise ratio was achieved [15].

A second, complimentary approach is to reduce the stray capacitance so that sensing can be accomplished at higher frequency. Gawad et al. reduced the stray capacitance down to 0.5 pF and achieved sensing at a high-frequency range between 100 kHz and 10 MHz [13, 16]. Generally speaking, high-frequency AC impedance sensing requires more consideration in electrode design, chip isolation, signal conditioning, and processing. In this chapter, an innovative approach to extending the AC impedance sensing range to higher frequencies is also proposed and demonstrated. It uses an external parallel inductor for induced resonance impedance sensing. The inductor cancels out the capacitive components in the system and improves sensitivity significantly. In the following sections of this chapter, a platinum black electroplated micro impedance sensor is first presented, followed by a discussion on the inductor-induced resonance impedance sensing method.

3.2 Platinum black electroplated micro impedance sensors

Theoretically, electrodes with high effective surface areas are ideal to overcome the problem with double-layer impedance. Platinum black electroplated electrodes have porous surface structures, thus increasing the effective electrode surface area. This can reduce the electrode surface double-layer impedance by two orders of magnitude [17, 18].

Consequently the channel resistance becomes the dominant system impedance in some intermediate frequency range, and the device becomes sensitive to what is flowing inside. Platinum black electroplated micro electrodes have been used for extracellular neural signal recording [11−13], gas sensing [14], and thermal infrared detection [15]. Reported here is the use of platinum black electroplated microelectrodes as AC impedance sensors for human blood cell count.

In the following subsections of 3.2, the system model and two special cases are first presented. Then the design and fabrication of two types of devices follow. The principle of electrical impedance sensing with platinum black electroplated devices was validated with impedance spectra measurements first and then with flow sensing of polystyrene beads. Finally, the results of flow sensing of human blood cells in diluted whole blood and leukocyte-rich plasma (LRP) are presented.

3.2.1 Principle and model

The platinum black electroplated impedance sensor can be modeled equivalently as the channel impedance, Z, in series with a constant phase element (CPE) and in parallel with the stray capacitance, C_{st}, as shown in Fig. 3-5. Z includes electrolyte impedance and the impedance of the particle to be sensed between the electrodes. The particle was sensed at 10 kHz. In this low-frequency regime, the resistance component of the channel impedance dominates the reactance component. Therefore, the channel impedance is effectively modeled as a resistor R. A CPE is contributed by the electrode double-layer impedance of the electrolyte-electrode interface. It can include the effects of double-layer capacitance, inhomogeneous reaction rates, charge transfer on electrode surface, and transport of electrochemical active components from and to the surface. It is

affected by factors such as surface roughness, types of ions, ionic concentrations, temperature, and electrode potential. C_{st} is the coupling capacitance between the two electrodes.

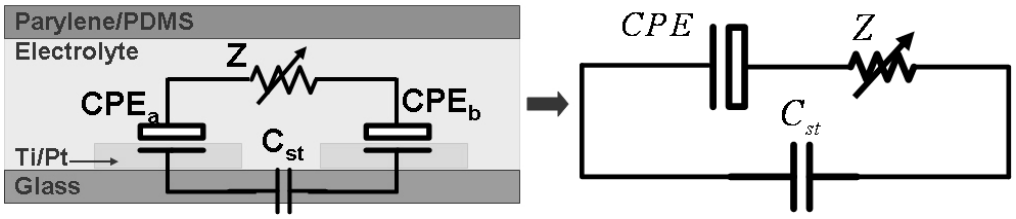

Figure 3-5 *System Model of platinum black electroplated impedance sensor*

The double-layer impedance due to the electrode-electrolyte interface is capacitive in nature. But nonideal factors, i.e., inhomogeneity and dispersion of the system, makes it more practical to model the double-layer impedance as a CPE. Impedance of CPE is:

$$Z_{CFE} = \frac{Z_0}{(j\omega)^{\alpha}}, \quad (0 \le \alpha \le 1), \tag{3.3}$$

with constant Z_0, $j = \sqrt{-1}$, angular frequency ω, and exponent α between zero and one. The phase of the CPE is a constant of $-\alpha\pi/2$. Normal metal electrodes have α close to one and the CPE behaves like a capacitor with phase of $-\pi/2$, in which case Z_0 is simplified to the inverse of the double-layer capacitance C_{dl}. There are at least two effects that can make α deviate from one. The surface roughness can change α from 1 in perfect flat two-dimensional electrodes, to 0.5 in three-dimension porous cubic electrodes [19]. Another effect that is likely to change α in the microdomain is the difference between the electrochemically active ionic concentrations on electrode surfaces and the

bulk ionic concentrations. In microdevices, the ratio of electrode surface area to the volume of the sensing zone is so large that the electrochemical reaction on the electrode surface can be diffusion limited. Also the small size of the channel sets up a diffusion barrier for active ions.

From the system model, the overall measured impedance can be written as:

$$Z_{system} = \frac{1}{j\omega C_{st} + \frac{1}{R + Z_0 / (j\omega)^{\alpha}}}. \qquad (3.4)$$

Ideally when the particle is present at the sensing zone, its impedance will dominate the channel impedance and the overall measured impedance. This requires:

$$\left| \frac{Z_0}{(j\omega)^{\alpha}} \right| \le R \le \left| \frac{1}{j\omega C_{st}} \right|, \qquad (3.5)$$

which translates into the requirement:

$$R \ge C_{st}^{\frac{\alpha}{1-\alpha}} Z_0^{\frac{1}{1-\alpha}}. \qquad (3.6)$$

Clearly from equation (3.6), lowering the stray capacitance and double-layer impedance are favored for particle sensing. If the channel impedance satisfies equation (3.4), the system shows some typical asymptotic behaviors. When ω approaches zero, the system is reduced, approximately, to the channel impedance in series with the CPE. When ω approaches infinity, the system approaches the channel impedance in parallel with the stray capacitance. These asymptotic behaviors are illustrated in the Nyquist plot of Fig. 3-6, which can be used to extract parameters for measurement.

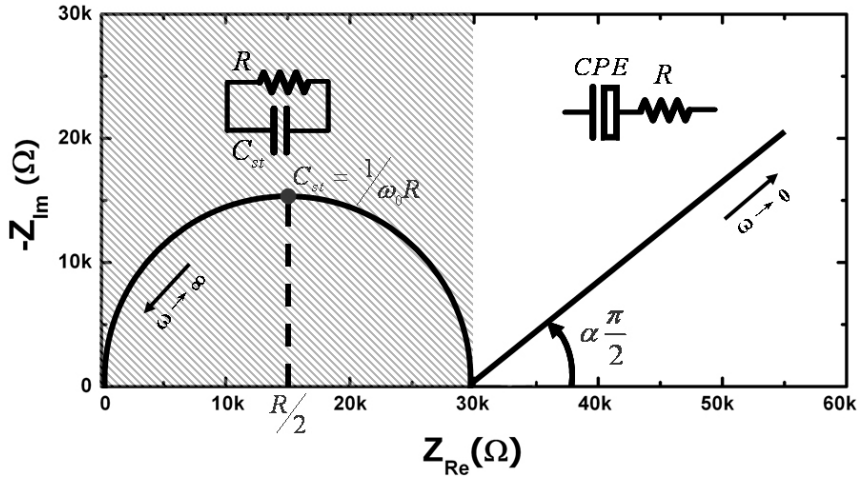

Figure 3-6 Asymptotic behaviors of platinum black electroplated impedance sensors in Nyquist plot. ω_0 is the angular frequency when Z_{Re} is R/2.

In order for the system to sense particles flowing past the electrode, the particle impedance should be the major component in overall system impedance at the excitation frequency. This is difficult to achieve in microsystems because of the miniaturization of the electrodes. In the low-frequency range, impedance of the CPE dominates the system impedance, while at high frequency the stray capacitance dominates. For particle sensing in low-frequency domain, an effective way is to lower impedance of the CPE by platinum black electroplating. It can change the surface roughness of metal electrodes by making the surface extremely porous and increasing surface area by two orders of magnitude, thus reducing electrical impedance by two orders of magnitude.

There are two special cases which will be considered: 1) α is close to one, and 2) α is close to 0.5. For these two cases, it is possible to gain some physical intuition from the equivalent model.

When α approaches one, the CPE effectively becomes a double-layer capacitance C_{dl}. To be more general, we also include a resistor R_{ct} in parallel with C_{dl} for charge transfer resistance. The system equivalent model is simplified as the inset of Fig. 3-7. The system impedance has two poles (P_1 and P_2) and one zero (Z_1) which can be expressed as:

$$Z_{sys}(s) = (R + R_{ct}) \frac{1 + s/Z_1}{(1 + s/P_1)(1 + s/P_2)} \quad . \qquad (3.7)$$

For microelectrodes, R_{ct} (~ GΩ) is much larger than R (< 100 kΩ). Therefore,

$$Z_1 = \frac{1}{RC_{dl}}, \qquad (3.8)$$

$$P_1 = \frac{C_{dl} + C_{st}}{RC_{dl}C_{st}}, \qquad (3.9)$$

$$P_2 = \frac{1}{R_{ct}(C_{dl} + C_{st})}. \qquad (3.10)$$

It can be shown that $P_2 < Z_1 < P_1$ under the condition $R << R_{ct}$.

For typical platinum black electroplated electrodes, the Bode plot of the magnitude of the system impedance in equation (3.7) contains a plateau frequency region limited by Z_1 and P_1. The plateau frequency region defines the *sensing zone*, in which the overall impedance is sensitive to channel resistance. For frequencies lower than Z_1, the system behaves as the double-layer capacitor C_{dl}. For frequencies higher than P_1, the stray capacitance C_{st} dominates the frequency response.

Shown in Fig. 3-7 are two extreme cases where the sensing zone shrinks and the whole system behaves like a capacitor. The first case is when R is extremely large. This

is the case where the channel is filled with air or DI water instead of electrolyte. The other case is with the electrodes without platinum black electroplating, which have a C_{dl} two orders of magnitude smaller. Thus, the overall impedance is dominated by the double-layer impedance. The signal due to the passing particles is reduced. This effect is seen on the impedance spectra when zero Z_1 moves to higher frequency and approaches the high-frequency pole P_1. One possible solution is to reduce the stray capacitance C_{st}. This will increase *P1*, shifting the sensing zone to higher operating frequency. This, however, is not always favorable. It can make the device structure and sensing circuitry more complicated. Another solution is to increase double-layer capacitance C_{dl}, which will decrease the zero frequency Z_1 and extend the sensing zone to lower operating frequency.

The other special case is when α is close to 0.5. If this is the case, the slope of the low-frequency linear part on the Nyquist plot will be one. This low-frequency region represents typical Warburg impedance, which generally indicates a diffusion-limited regime [20]. It will be shown later in this chapter that one type of the devices fabricated belongs to this case.

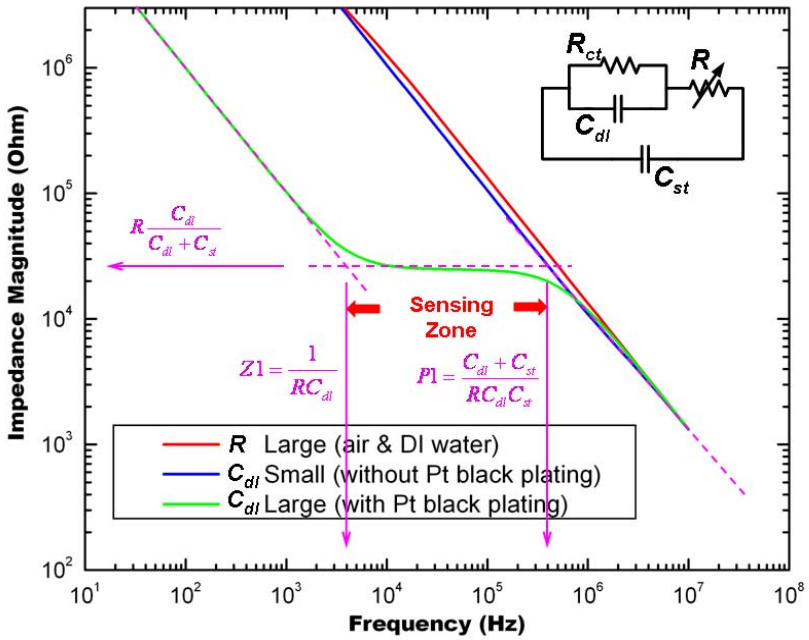

Figure 3-7 *Bode plot of numerical simulation of impedance magnitude spectra of platinum black electroplated impedance sensor device I. Inset is the simplified circuit diagram. Dash lines are asymptotes*

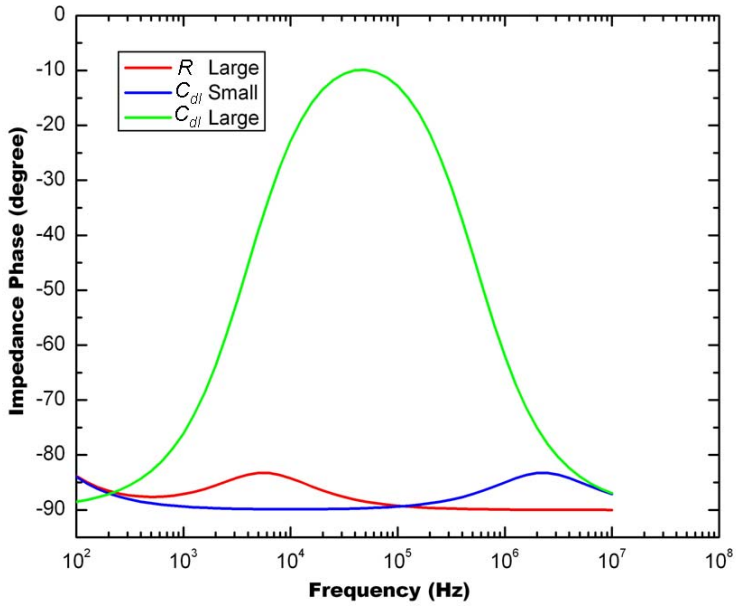

Figure 3-8 *Bode plot of numerical simulation of impedance phase spectra of platinum black electroplated impedance sensor device I.*

3.2.2 Device design and layout

Fig. 3-9 shows an overview of device I. There are three devices on each chip. The middle one has an aperture size of 20 μm in length by 15 μm in width. It has two pairs of electrodes separated by 50 μm. Channel height is 20μm and channel wall thickness is 10 μm. All tests were performed using the middle device.

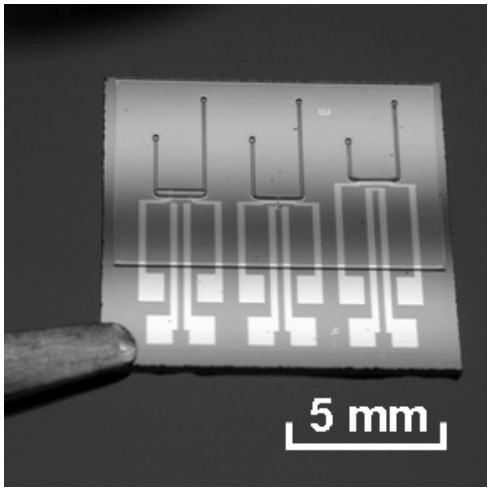

Figure 3-9 *Fabricated platinum black electroplated impedance sensor device I*

The chip layout for device II is illustrated in Fig. 3-10. Two fluidic chambers are separated by an aperture. The width of the aperture is 15 μm. The length of the aperture is 30 μm. One pair of metal electrodes is used to sense the electrical impedance across the aperture. The size of the chamber is very large compared with the aperture so that the measured channel impedance is dominated by the impedance of the aperture region. The distance between the electrodes is 70 μm. At the inlet and outlet, some filter structures are designed to mechanically block contaminants and particle aggregates and prevent

them from clogging the aperture. Channel height is optimized to be around 15 μm so that all blood cells can pass while maintaining the maximum signal magnitude.

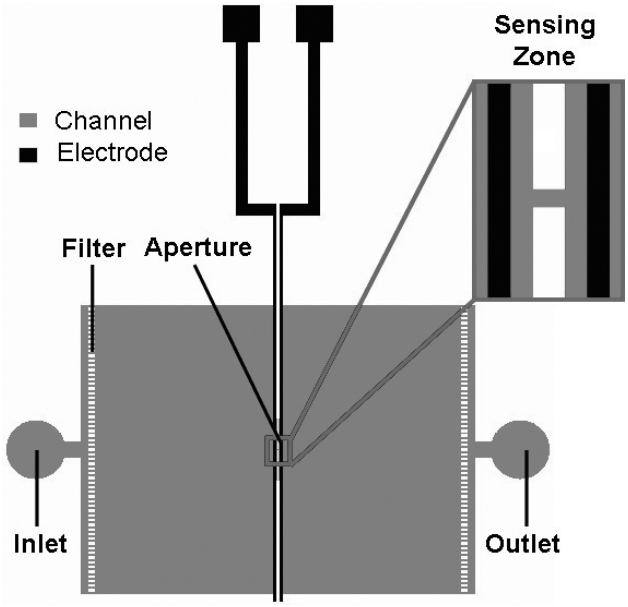

Figure 3-10 Design layout of platinum black electroplated impedance sensor device II

3.2.3 Device fabrication

Device I is based on integrated parylene technology (Fig. 3-11) [21]. The benefits of parylene include its processibility, stability, flexibility, and biocompatibility. The parylene channels are strengthened by SU8. The process is started with thermal growth of oxide to provide electrical isolation. Then Ti/Pt/Ti (200A/2000A/200A) electrodes are patterned by liftoff process. The top layer of Ti inside the channels is etched away with buffered HF. Ti/Pt electrodes are used because they are chemically inert and can withstand high voltage without erosion for the duration of the device's use. Other portions of the top Ti layer are kept to provide superior adhesion to parylene. To avoid parylene channel delamination during later processing stages, parylene anchors are made

on silicon using DRIE. Then 10 μm of parylene is deposited by CVD and patterned by RIE with an Ti/Au mask. Before sacrificial photoresist releasing in acetone, a 50 μm thick SU8 layer is coated and patterned to planarize the surface and strengthen the parylene channels. Finally, platinum black is electroplated selectively on electrode surfaces that are exposed to electrolyte. Electroplating solution was introduced into the channel either by syringe injection or vacuum suction.

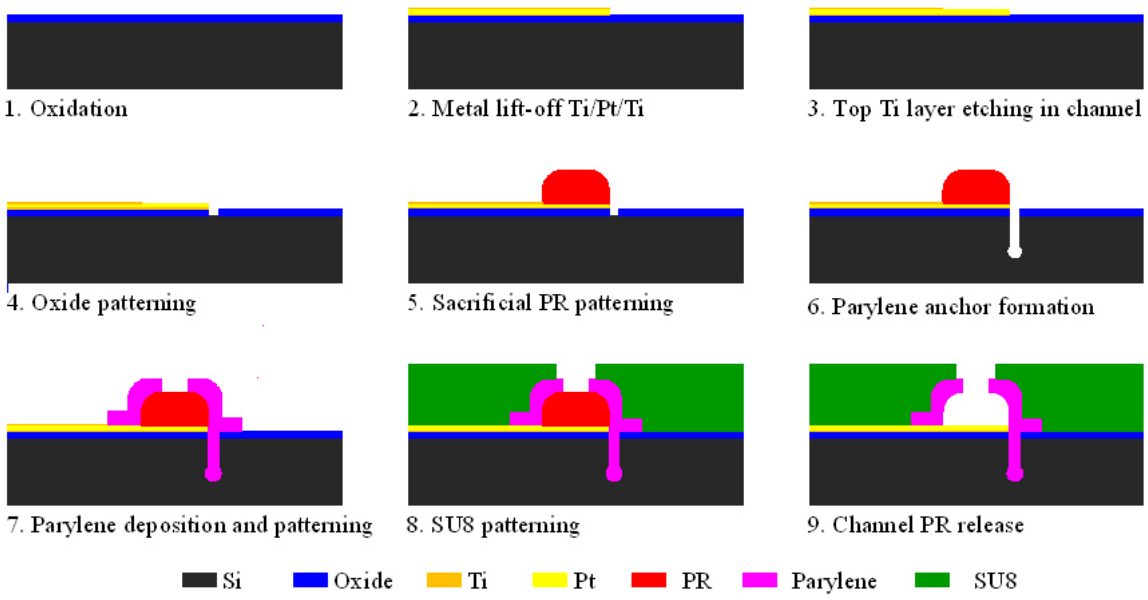

Figure 3-11 *Fabrication process flow for platinum black electroplated impedance sensor device I*

A transparent acrylic packaging jig was designed and fabricated for device I to provide convenient electrical and fluidic accessibility from the top and thus avoid backside wafer processing (Fig. 3-12). The jig provides eight fluidic accesses simultaneously. Commercial fittings (Upchurch Scientific, WA, USA) are used to connect between the jig and other fluidic components, such as syringe pumps or outlet

tubings. There is a recess at the bottom of the acrylic jig which provides space for an epoxy-strengthened wire bond region on the chip.

After fabrication, the chip is glued and wire bonded onto a printed circuit board (PCB). There are a total of 44 pads on the PCB of which only 12 are used. A 200 μm thick PDMS layer with through holes is aligned and placed on top of the chip to provide sealing between the jig and the chip. Finally, the jig is tightened firmly onto the PCB with screws (Fig. 3-13).

The fabrication of device II is based on soft lithography [22]. It starts with molding channel structure on PDMS with a DRIE etched Si mold. Ti/Pt (200 A/2500 A) electrodes are patterned on a soda-lime glass substrate by E-beam evaporation and lift-off process. Platinum black is then electroplated on the areas where metal electrodes are exposed to electrolyte. The thickness of the electroplated platinum black layers is normally greater than 1 μm. Finally, the PDMS block is bonded to the glass surface at 80 ℃ overnight. After fabrication, the chip is glued and wire bonded onto a printed circuit board.

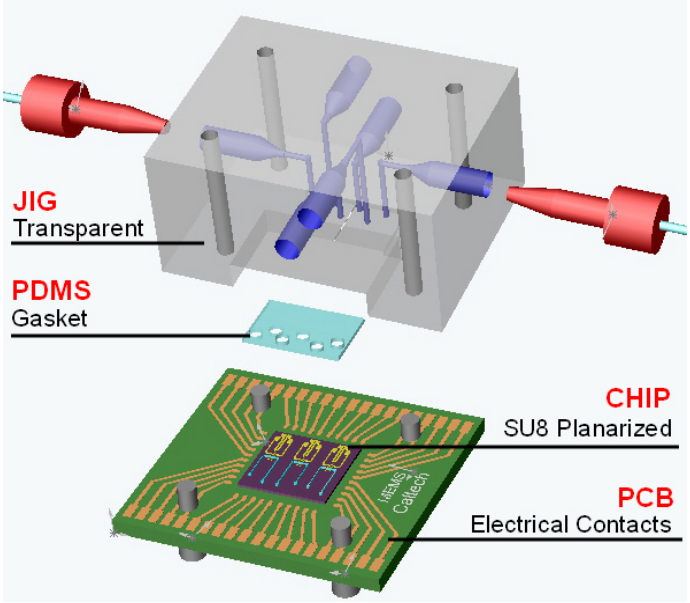

Figure 3-12 *Chip assembly with jig and PCB for platinum black electroplated impedance sensor device I*

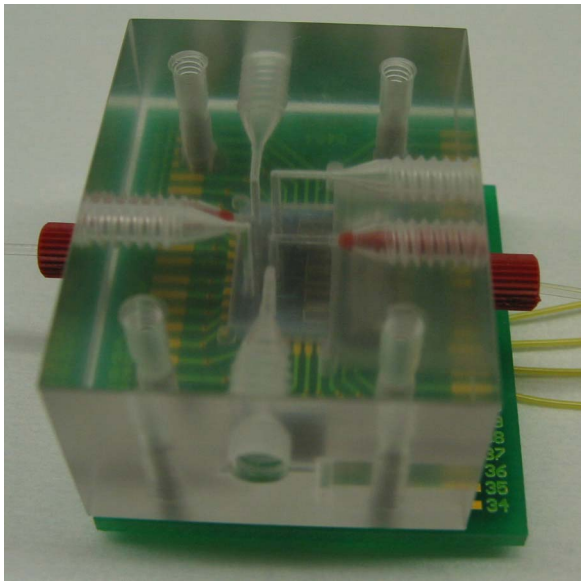

Figure 3-13 *Assembled platinum black electroplated impedance sensor device I with jig*

3.2.4 Testing materials and setup

5 μm, 8 μm, and 10 μm polystyrene beads were purchased from Duke Scientific Corporations, Fremont, CA. Fresh human blood was obtained from healthy donors and used within three days. EDTA was added to the blood collection tube to prevent coagulation. Blood samples were diluted in phosphate buffered saline (10x PBS Ambion, Austin, TX). The impedance spectra of the device filled with different media were measured with an LF impedance analyzer (HP 4192A, Santa Clara, CA). The excitation voltage was set to 0.1 V for all measurements. For flow sensing, the particles were introduced into devices by a syringe pump (Harvard Apparatus Pico Plus, Holliston, MA). Electrical excitation and particle pulse sensing were performed with a lock-in amplifier (EG&G Princeton Applied Research 5210, Princeton, NJ).

3.2.5 Platinum black electroplating

Platinum black was electroplated selectively on the electrode surface exposed in the channel. Electroplating solution contains 1% chloroplatinic acid (Sigma C-3044), 0.0025% hydrochloric acid, and 0.01% lead acetate in water [17]. Electrodes were plated with 5 V DC through a 10 MΩ resistor for up to four minutes.

To preventing the platinum black from being exposed to potentially destructive chemicals during device fabrication, the platinum black electroplating is performed as the last step after channel release. Electroplating solution is introduced into the channels. The electroplating process for device I is not as easy to control as that of device II, which is performed in a reservoir of electroplating solution. As a result, the electroplating for device I is not as complete as that of device II. This is an important factor in explaining the differences in impedance spectra of the electrodes from the two processes.

SEM pictures of a platinum black electroplated electrode of device I and II are shown in Fig. 3-14. The surface of device II is much rougher than device I, which suggests a more complete platinum black electroplating.

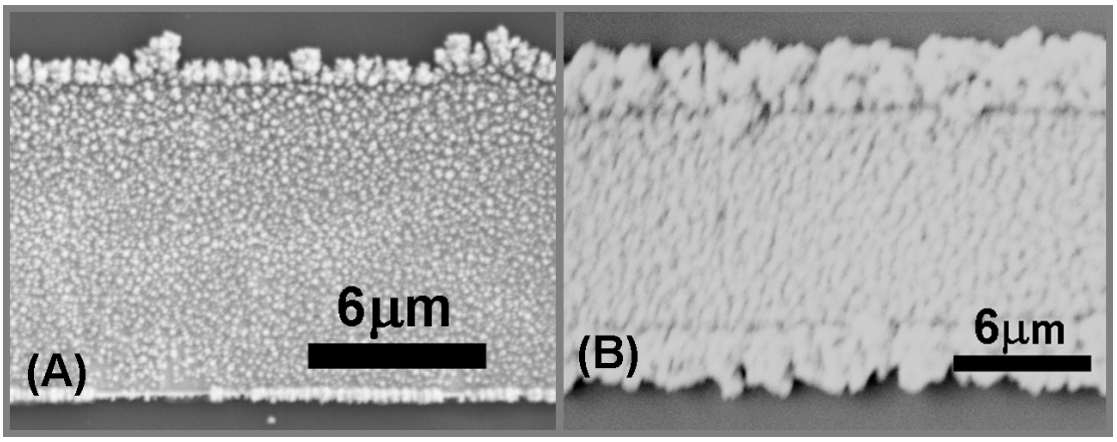

Figure 3-14 SEM pictures of platinum black electroplated electrodes. (A) device type I. (B) device type II

Fig. 3-15 shows images from AFM measurements of platinum electrodes before and after Pt black electroplating. The surface feature size becomes much larger after Pt black electroplating. The measured surface roughness changed from 6.75 nm to 238 nm, an increase of 35 times.

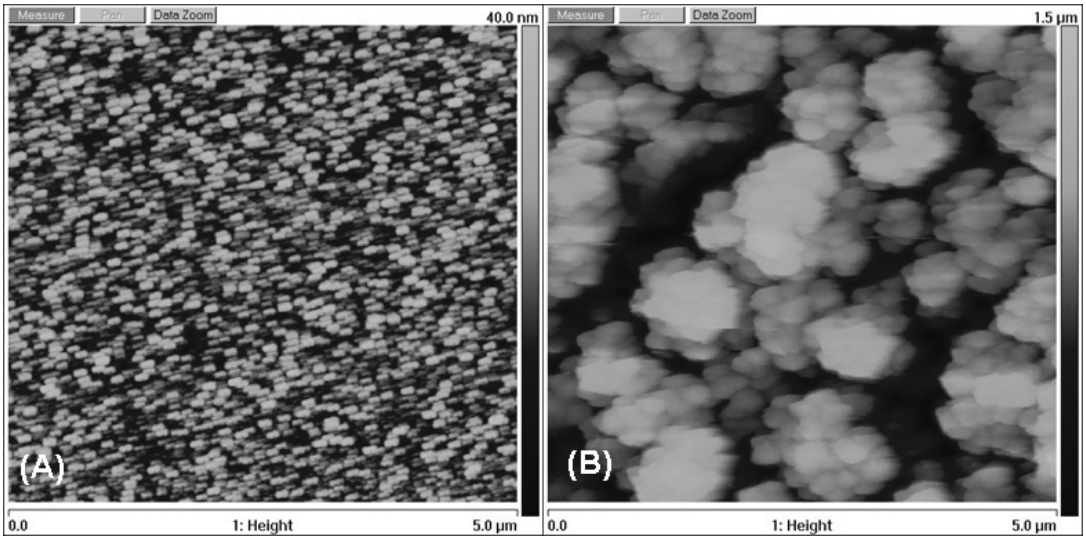

Figure 3-15 *AFM images of platinum electrode before electroplating (A) and after electroplating (B) of device II. Note the scales are different, with maximum of 40 nm in (A) and 1.5 µm in (B).*

3.2.6 Impedance spectra measurement

Measured impedance spectra of device I are shown in Fig. 3-16 and Fig. 3-17, which demonstrate the introduction and expansion of the sensing frequency zone by platinum black electroplating. The frequency responses of air and water almost overlap. Their magnitude responses are straight lines and phase responses kept a constant -90 degree angle for the frequency range scanned. This agrees with the case of large *R* in the model analysis.

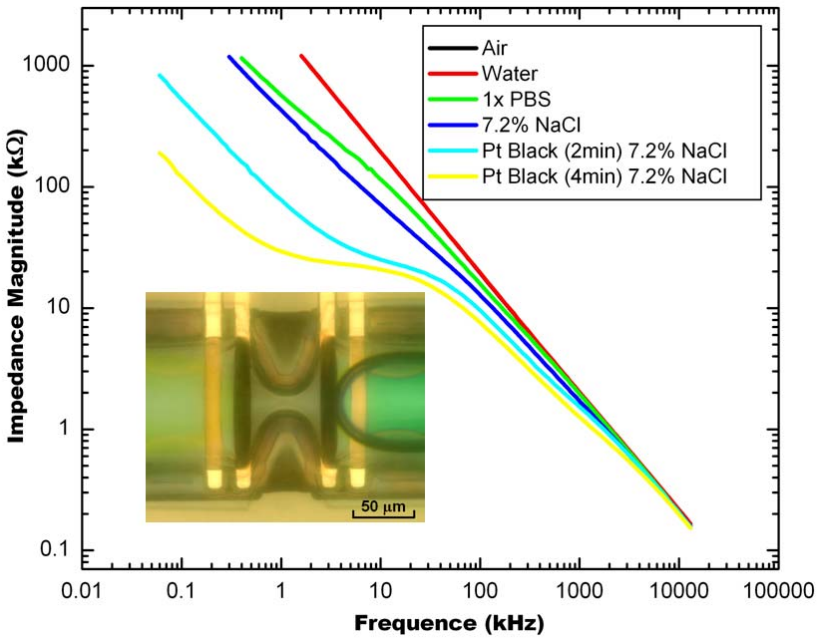

Figure 3-16 *Bode plot of measured impedance magnitude response in different environments of platinum black electroplated impedance sensor I. Electroplating with platinum black (the lower two curves) effectively expand the sensing zone.*

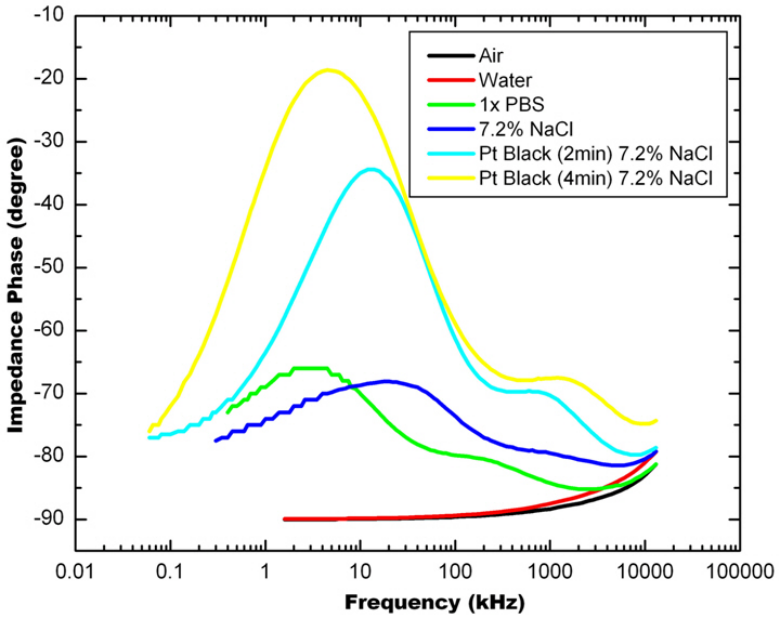

Figure 3-17 *Bode plot of measured impedance phase response of platinum black electroplated impedance sensor I*

Before platinum black electroplating, both phosphate buffered saline (PBS) and high salt solution (7.2% sodium chloride) have little impact on the frequency response. This is because at high frequency, the system is dominated by stray capacitance, C_{st}, and at low frequency by C_{dl}. Since *Z1* and *P1* are so close, the sensing zone in the frequency domain shrinks to zero. After electroplating, C_{dl} was measured to be 2.5 nF, an increase of two orders of magnitude. The magnitude response showed a plateau region between 1 kHz and 30 kHz. This region expanded as the time of electroplating increased. The expansion is caused mainly by reducing the low-frequency bound, which is determined by the double-layer impedance. The high-frequency bound remains almost unchanged. The high frequency is determined by the large stray capacitance, which is mainly caused by the coupling between the electrodes and the Si substrate. It can be improved by using a thicker oxide insulation layer or building devices on electrical insulating materials, such as glass. The phase response exhibits a large increase in the sensing zone and the maximal phase of -20 degrees at 5 kHz is achieved for four minutes of platinum black electroplating. Fig. 3-18 is the Nyquist plot with a linear fit on the low-frequency part and circular fit on the high-frequency part.

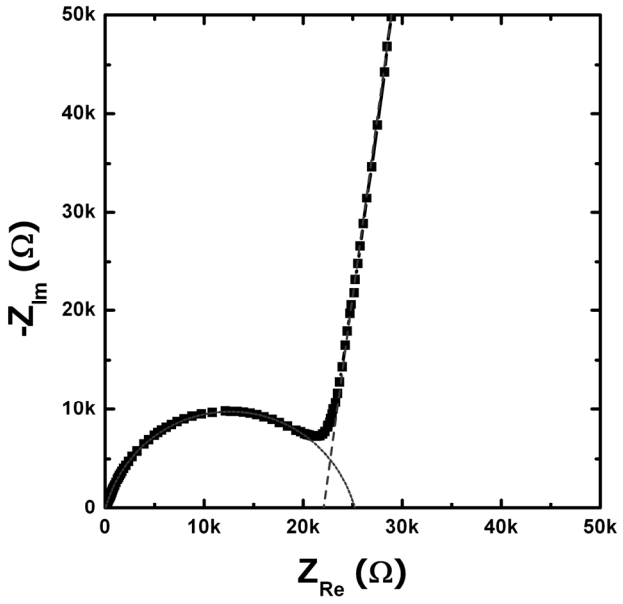

Figure 3-18 Nyquist plot of platinum black electroplated impedance sensor device I. Dash lines are fitted curves.

Fig. 3-19 shows the Bode plot of measured and simulated impedance magnitude and phase responses of device II. Similar to device I, before platinum black electroplating, the system impedance response shows capacitive characteristics in all frequency ranges. And the impedance responses in air, deionized (DI) water, and PBS are similar to device I (data not shown here). After platinum black electroplating, resistive characteristics in the frequency range from 100 Hz to 3 MHz (the plateau in the figure) appear. This is the frequency range suitable for cell sensing. $\alpha = 0.5$ is used to fit the impedance spectra measurement data to the model proposed as before. Table 3-1 lists parameters extracted from the Nyquist plots (Fig. 3-18 and Fig. 3-20) of the asymptotic behaviors of device I and II.

Comparing system impedance spectra of device I and device II, device II has a broader sensing zone (100 Hz–3 MHz versus 1 kHz–30 kHz). The glass substrate of device II has a lower stray capacitance than the oxide-isolated Si substrate of device I. This extends the high bound of the sensing zone by one decade. The improvement in the lower bound of the sensing zone was mainly due to the platinum electroplating. From the SEM pictures of Fig. 3-14, the platinum black electroplating is more complete for device II. Consequently, the electrode surface of device II is rougher and resembles more of a 3D structure. This is reflected in the measured α values of the two types of devices. The difference of α values between device I and device II is likely caused by the difference in surface roughness of these two types of devices.

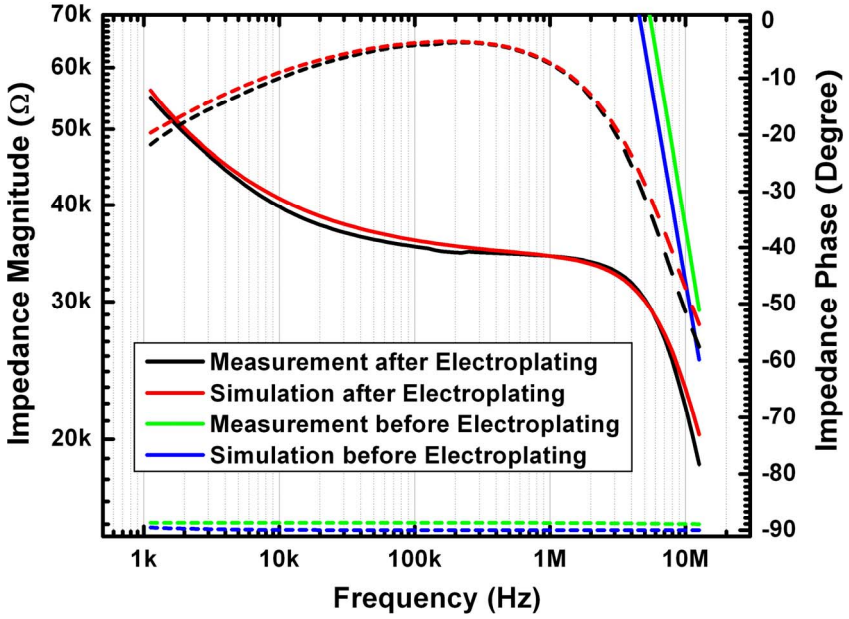

Figure 3-19 Bode plot of simulated and measured system impedance magnitude (solid lines) and phase (dash lines) response in electrolyte phosphate buffered saline (PBS) of platinum black electroplated impedance sensor device II. Data were fitted by least-squares curve-fitting, with parameters $Z_0 = 2.24$ MΩ, $C_{st} = 0.5$ pF, and α=0.5.

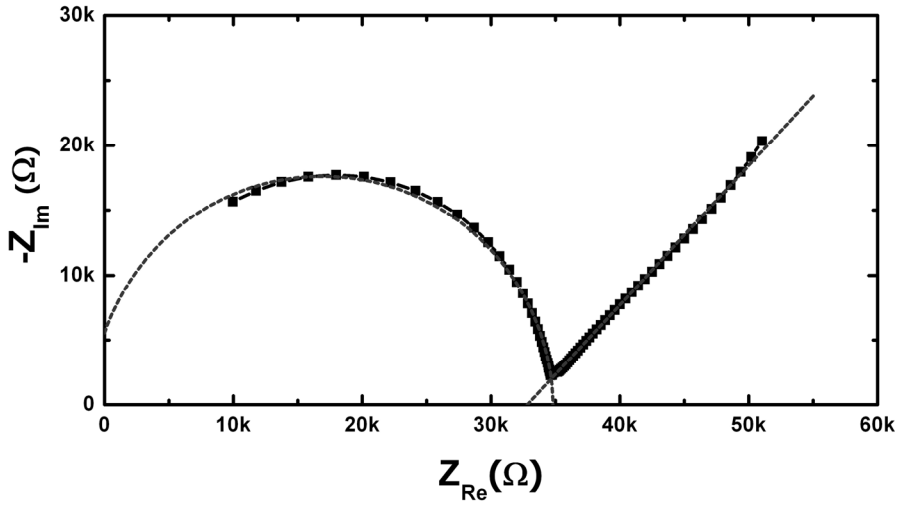

Figure 3-20 Nyquist plot of measured impedance data of platinum black electroplated impedance sensor device II

Table 3-1 Parameters obtained by fitting Nyquist plots to asymptotes of platinum black electroplated impedance sensor device II. Low-frequency domain was fitted to a straight line and high-frequency data were fitted to a part of circular curve. R^2 is the multiple correlation coefficient.

		Device I	Device II
Linear $-Z_{Im}=A+BZ_{Re}$	**A (kΩ)**	-161.1 ± 1.3	-35.22 ± 0.25
	B	7.304 ± 0.047	1.074 ± 0.006
	R^2	0.9992	0.9986
Circular $(Z_{Re}-a)^2+(-Z_{Im}-b)^2=r^2$	**a (kΩ)**	12.62 ± 0.05	16.9 ± 0.2
	b (Ω)	-326 ± 8	-281 ± 197
	r (kΩ)	13.0 ± 0.8	17.9 ± 0.2
	R^2	0.9989	0.9967
R (kΩ)		26.0	35.8
C_{st} (F)		1.3 n	3.6 p
α		0.91	0.52

3.2.7 Flow sensing of polystyrene beads

Results of bead and human blood cell sensing are presented here only for device II. Similar results were obtained for device I. Polystyrene beads with different sizes were used to calibrate the system. The flow rate was 1 nL/min. The particle concentrations were in the range of 10^4 beads/μL. Fig. 3-21 shows an example of a time trace of 8 μm polystyrene beads. The peak height was 0.2608 V ± 0.0127 V less than a 5% standard deviation, for a sample of 43 beads in one testing. The duration of the peaks were 17.21 ms ± 0.67 ms, which corresponded well with the expected time for the beads to pass the sensing zone. Fig. 3-22 is a typical peak from the same data set. Measured signals from 5 μm and 10 μm polystyrene beads are plotted in Fig. 3-23. Theoretical channel resistance change with DC excitation was calculated and plotted as the dashed line. It is well known as the Coulter principle, that under DC excitation the signal magnitude is determined by the volume of the particles. Our measurement results confirmed that for low excitation frequency, such as 10 kHz, the magnitude of resistance change was determined by the particle size.

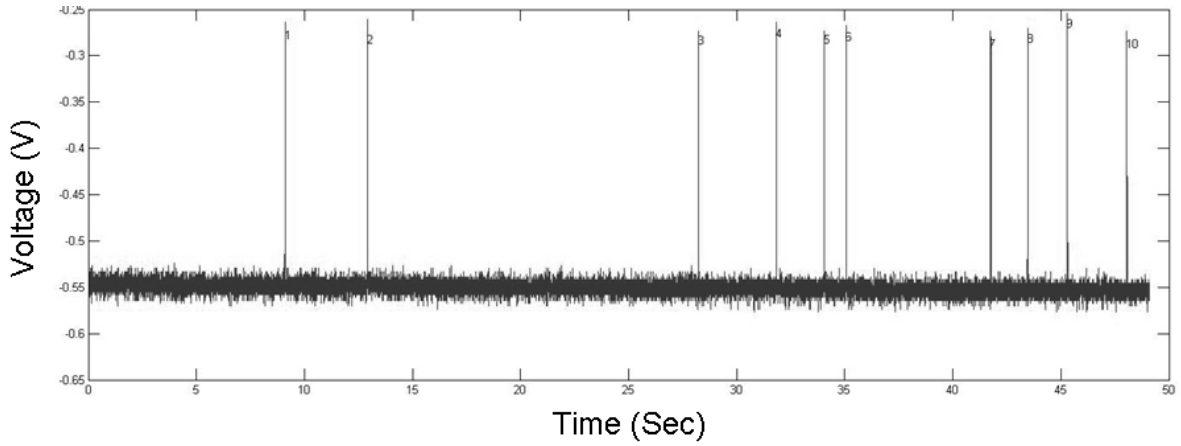

Figure 3-21 *Time trace of 8 μm beads tested at 10 kHz in platinum black electroplated impedance sensor device II. Detected peaks are labeled.*

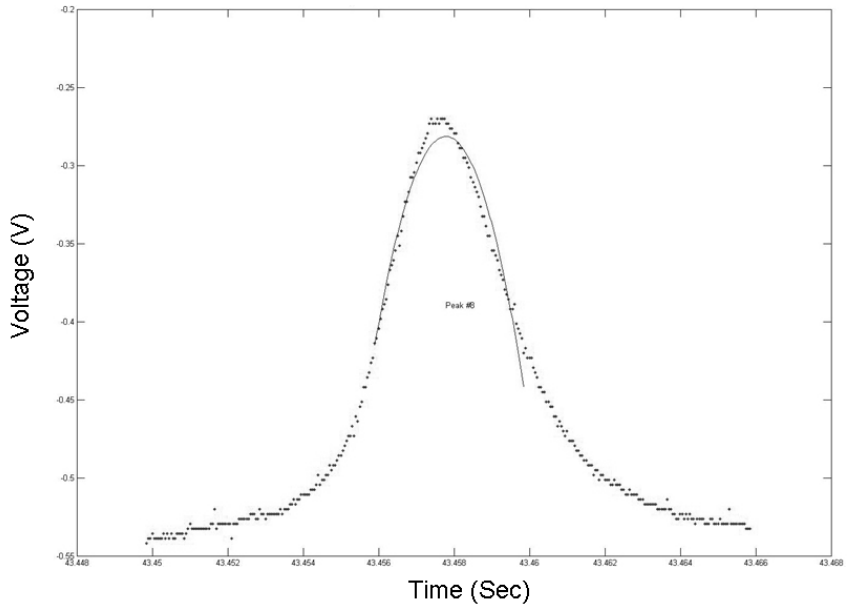

Figure 3-22 *A typical example peak of 8 μm beads tested at 10 kHz in platinum black electroplated impedance sensor device II. The solid line is least-squares curve-fitting to a parabola*

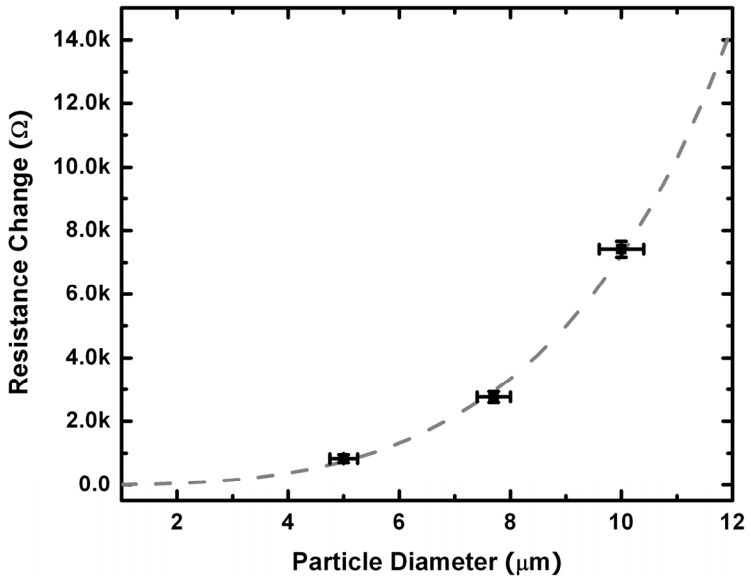

Figure 3-23 *Sensing signal depends on the size of polystyrene beads in platinum black electroplated impedance sensor device II. Dash line is theoretical relationship at DC.*

3.2.8 Flow sensing of human blood cells

Human blood cell sensing was performed either with diluted whole blood or diluted leukocyte-rich plasma. Whole blood samples were obtained from healthy donors and used within 48 hours. Normal whole blood has an erythrocyte-to-leukocyte ratio of about one thousand to one. Hence, it is suitable for erythrocyte characterization without leukocyte interference. Leukocyte-rich plasma was prepared by collecting the plasma fraction after whole blood sedimentation in Wintrobe tubes. Erythrocyte-to-leukocyte ratio can be reduced by at least two orders of magnitude. Therefore, leukocyte-rich plasma is better for leukocyte testing.

Fig. 3-24 shows a time trace for human whole blood diluted one thousand times with PBS and Ficoll-Paque Plus. The signal-to-noise ratio is not as good as for the 8 μm beads, and a slowly drifting baseline was sometimes experienced. Closeups of peaks are

shown in Fig. 3-25. The peak height has a wide distribution, which indicates that the cell size varied. The distribution of pulse height matches well with the known volume distribution of erythrocytes (Fig. 3-26). Leukocyte-rich plasma was used for leukocyte sensing. The tail part of the peak height distribution is due to leukocytes. The data resembles the known leukocyte volume distribution (Fig. 3-27).

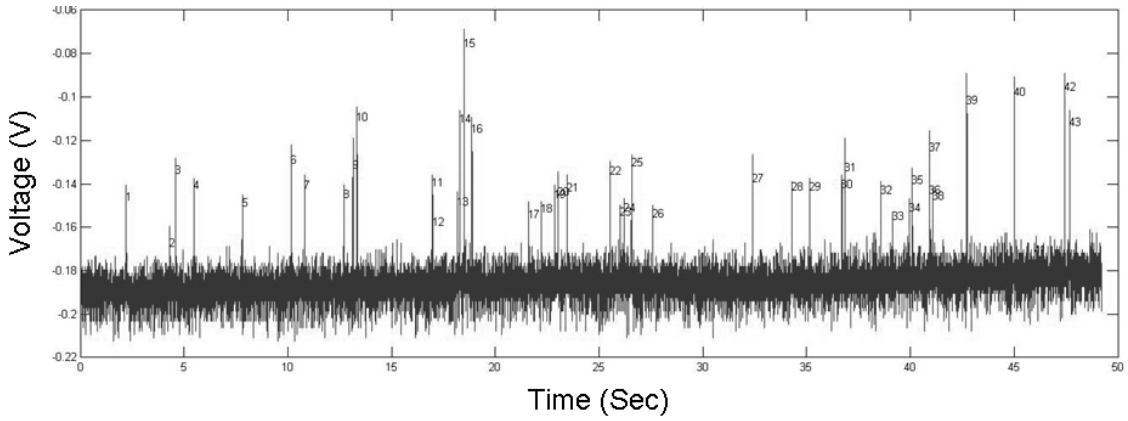

Figure 3-24 *Time trace of diluted human whole blood in platinum black electroplated impedance sensor device II. Detected peaks are labeled*

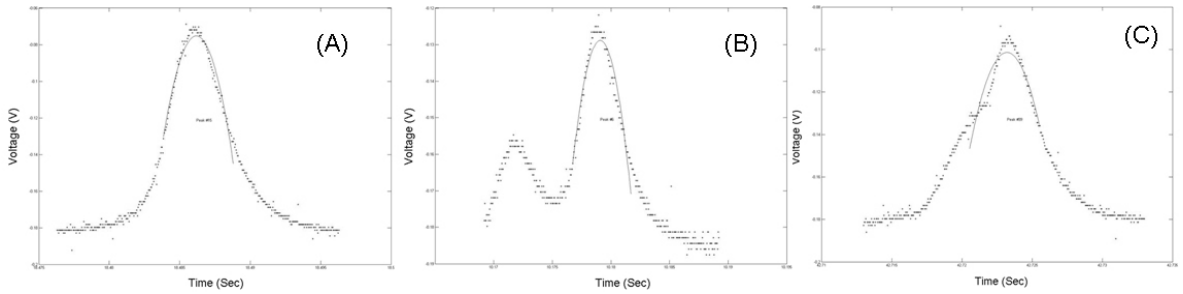

Figure 3-25 *Sensing cells from diluted human whole blood in platinum black electroplated impedance sensor device II. The solid lines are least-squares curve-fittings to parabola: (A) a typical peak, (B) two close peaks, (C) two peaks too close to be separated.*

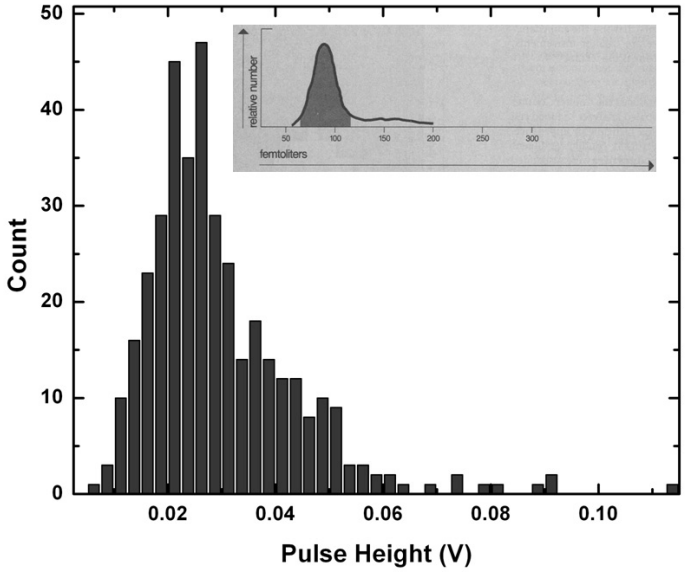

Figure 3-26 *Pulse height distribution of diluted human whole blood, in which leukocyte to erythrocyte ratio is about one to a thousand. Inset is erythrocyte volume distribution from [23].*

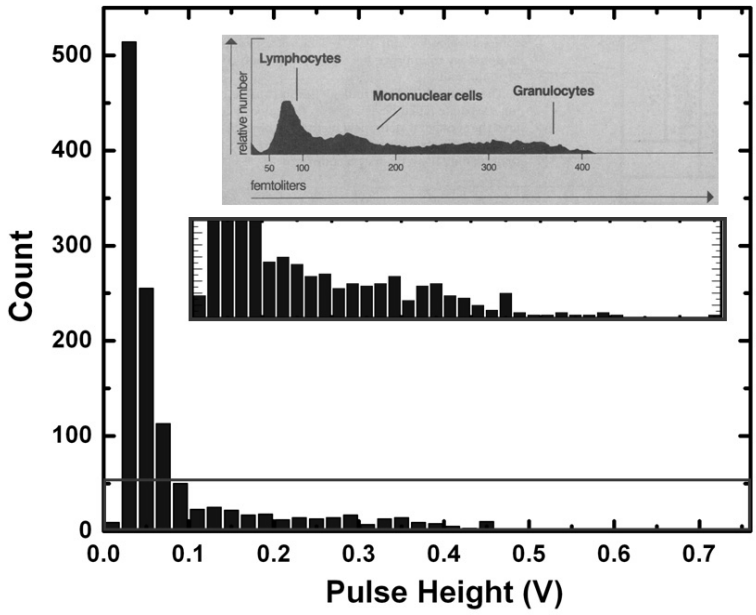

Figure 3-27 *Pulse height distribution of leukocyte rich plasma, in which leukocyte to erythrocyte ratio is about one to ten. Middle inset shows the detail of the tail of the distribution. Top inset is leukocyte volume distribution from [23].*

3.3 Inductor-induced resonance impedance sensing

In traditional AC impedance sensing, the electrodes are a metal helical conduit, in which the particle suspension flows. The metal conduit acts as an electrical inductor. To achieve electrical isolation, an external parallel capacitor is introduced to induce resonance and make the metal conduit a high-impedance path for the electrical signal. Alternatively, an external parallel inductor can be introduced into the system for the purposes of AC impedance sensing. At the resonant frequency, the capacitive components of the system are nullified by the inductor, leaving the channel impedance to be the major component in system impedance. Unlike the traditional AC impedance sensor system, the inductor is introduced to nullify the inherent capacitive components. We recently demonstrated that the sensitivity of a microchip capacitively-coupled contactless conductivity detector (C^4D) can be improved by more than 10,000 times [24]. In this study, conventional discrete coil inductors were used to demonstrate the principle, but the inductors can also be fabricated on the microchip to provide an integrated solution [25].

3.3.1 Principle

The device without the inductor connected can be modeled as the channel impedance, *Z,* in series with a double layer capacitance, C_{dl},, in parallel with the stray capacitance C_{st} as in Fig. 3-28. *Z* includes electrolyte impedance and impedance of particle to be sensed between the electrodes. For low-frequency excitation (under 100 kHz), the resistance part of the channel impedance dominates the reactance part. So in the following, the channel impedance is effectively modeled as a resistor, *R*. C_{dl} is due to the electrolyte-electrode interface. For micro metal electrodes without surface treatment,

this is a reasonably good approximation. C_{st} is the coupling capacitance between the two electrodes. After an inductor is connected to the system, its inductance (L) and resistance (R_L) are included in the model.

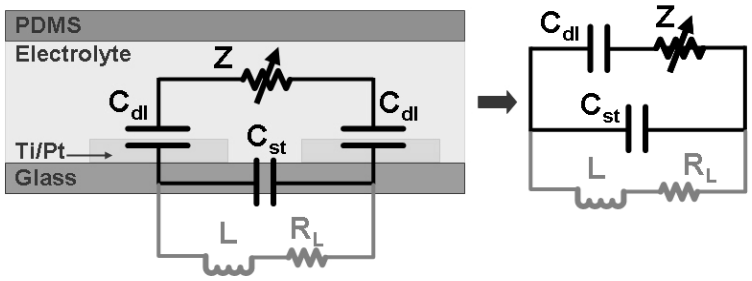

Figure 3-28 *System model of inductor-induced resonance impedance sensor. The channel impedance Z is replaced with channel resistance R in later analysis.*

From the system model, the overall measured impedance can be written as:

$$Z_{sys}(j\omega) = \frac{1}{j\omega C_{st} + \frac{1}{R + 1/j\omega C_{dl}} + \frac{1}{R_L + j\omega L}}. \tag{3.11}$$

When the total current and the terminal voltage is in phase, the parallel circuit is considered to be in resonance[26]. In resonance, the imaginary part of the total admittance (the susceptance) will be zero, from which the resonant frequency and the impedance (resistance) at resonance can be calculated as:

$$f_0 = \frac{1}{2\pi}\sqrt{-\frac{R_L^{\,2}}{2L^2} + \frac{\Delta}{2C_{dl}^{\,2}C_{st}L^2R^2}}, \tag{3.12}$$

$$Z_0 = \left(\frac{2C_{dl}^{\,2}C_{st}R^2R_L}{\Delta + C_{dl}^{\,2}C_{st}R^2R_L^{\,2}} + \frac{1}{R\left(1 - \frac{2C_{st}L^2}{C_{dl}^{\,2}C_{st}R^2R_L^{\,2} - \Delta}\right)}\right)^{-1}, \tag{3.13}$$

$$\Delta = -C_{dl}L^2 - C_{st}L^2 + C_{dl}{}^2LR^2 + \sqrt{-4C_{dl}{}^2C_{st}L^2R^2(-L + C_{dl}R_L{}^2 + C_{st}R_L{}^2) + (C_{dl}L^2 + C_{st}L^2 - C_{dl}{}^2LR^2 + C_{dl}{}^2C_{st}R^2R_L{}^2)^2}$$
. (3.14)

Under conditions, $L >> C_{st}R_L{}^2$, the above equations can be simplified:

$$\Delta_{simple} \approx 2C_{dl}{}^2LR^2, \quad (3.15)$$

$$f_{0,simple} = \frac{1}{2\pi}\frac{1}{\sqrt{C_{st}L}}, \quad (3.16)$$

$$Z_{0,simple} = (\frac{C_{st}R_L}{L} + \frac{C_{dl}{}^2R}{C_{dl}{}^2R^2 + C_{st}L})^{-1}. \quad (3.17)$$

3.3.2 Devices design and layout

Two types of devices were designed and fabricated. Device I is designed for sensing at a single frequency. Device II is designed for sensing at dual frequencies. The chip layout for device I is illustrated in Fig. 3-29. Two parallel sensing zones double the system throughput and enable differential input to sensing circuitry to reduce drift and noise. The two fluidic chambers are separated by an aperture. The width of the aperture is 14 μm. The length of the aperture is 20 μm. One pair of metal electrodes is used to sense the electrical impedance across the aperture. The size of the chamber is very large compared with the aperture, so the measured channel impedance is dominated by the impedance of the aperture region. The distance between the electrodes is 50 μm. At the inlet, filter structures are fabricated to mechanically block contaminants and particle aggregates and prevent clogging of the aperture. Channel height is optimized to be around 15 μm to allow blood cells to pass while maximizing signal magnitude.

For device II, two pair of electrodes for sensing, at low and high frequency respectively, are separated by 100 μm (Fig. 3-30). These electrodes also measure the real-time particle velocity inside the channel.

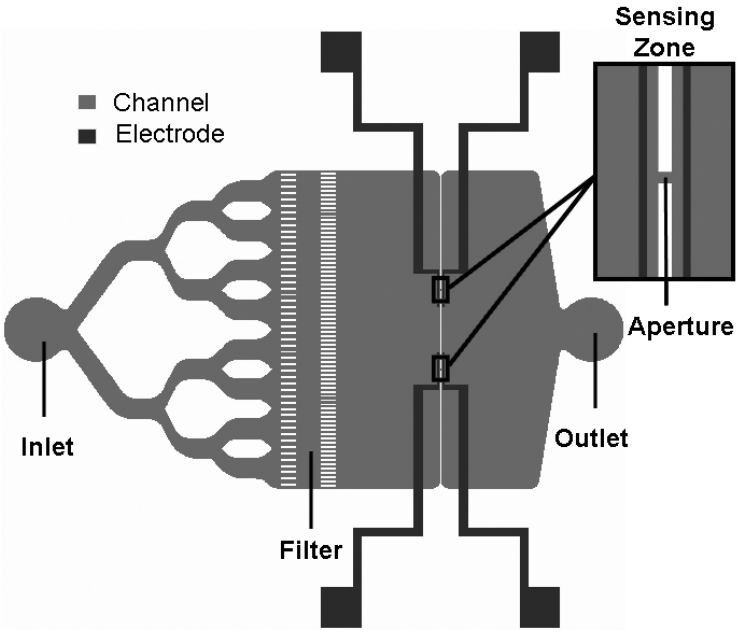

Figure 3-29 Design layout of inductor-induced resonance impedance sensor device I

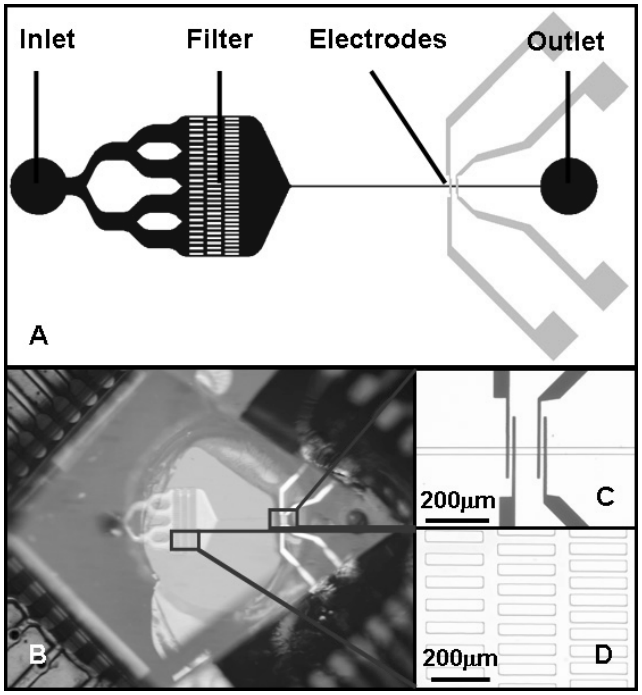

Figure 3-30 Device design and fabricated device of inductor-induced resonance impedance sensor device II. (A) Fluidic passage including inlet/outlet, filter and channel

and with electrodes patterned on bottom. (B) Assembled device. (C) Closeup view of the sensing region. (D) Close-up view of the filter region.

3.3.3 Device fabrication

The fabrication of the device is based on soft lithography [22]. It was started with molding channel structure on PDMS with a DRIE-etched Si mold. Ti/Pt (200 A/2500 A) electrodes are patterned on a soda-lime glass substrate with E-beam evaporation and lift-off process. Finally the PDMS block is bonded to a glass surface at 80℃ overnight. After fabrication, the chip is glued and wire bonded onto a printed circuit board.

3.3.4 Testing materials and setup

5 μm polystyrene beads were purchased from Duke Scientific Corporation, Fremont, CA. Fresh human blood was obtained from healthy donors and used within three days. EDTA was added to the blood collection tube to prevent coagulation. Blood samples were diluted in phosphate buffered saline (10x PBS Ambion , Austin, TX). The impedance spectra of the device filled with different media were measured with an LF impedance analyzer (HP 4192A, Santa Clara, CA). The excitation voltage was set to 0.1 V for all the measurements. Before particle flow testing, the resonant frequency of the system with the parallel inductor connected was identified from the impedance spectra measurement.

During flow sensing with device I, the particles were introduced into devices by a syringe pump (Harvard Apparatus Pico Plus, Holliston, MA). Electrical excitation and particle pulse sensing were performed with a lock-in amplifier (EG&G Princeton Applied Research 5210, Princeton, NJ) on one of the electrode pairs across one aperture. A voltage signal with constant amplitude was applied and the total current was measured.

Limited by the bandwidth of this lock-in amplifier, inductors with inductance value larger than 400 mH are needed in particle sensing to achieve resonant frequency under 100 kHz.

For device II testing, an inductor of 1 mH was connected in parallel to the device for sensing at 2.05 MHz, and inductors with a total of 1 H of inductance were used for sensing at 77 kHz. Without the inductor connected, the differences among system impedance spectra in air, DI water, and electrolyte solution PBS were small, indicating the device has poor sensitivity. Parallel inductors introduced resonance at specific frequencies determined by the inductance. Lock-in amplifier EG&G 5210 was used in current sensing mode for the low-frequency (77 kHz) signal. Another high-frequency lock-in amplifier SRS 844 (Stanford Research Systems, Sunnyvale, U.S.A.) was used in voltage sensing mode for the high-frequency (2.05 MHz) signal. A transimpedance amplifier was built to convert the current signal to a voltage signal before it was applied to the input of the high-frequency lock-in amplifier.

3.3.5 Impedance spectra measurement

3.3.5.1 Impedance spectra measurement of device I

Without the parallel inductor connected, the system impedance spectra were measured (Fig. 3-31). The impedance magnitude responses are straight lines with slope of -1. The impedance phase responses are constant at -90 degrees. These results mean the system behaved effectively as a capacitor. The impedance spectra had similar impedance responses whether the channel was filled with air, water or phosphate buffered saline (PBS). This confirmed that for bare micro electrodes, the sensors are not sensitive to the change of channel resistance. The system impedance spectra connected

with inductors of various inductance values were measured in PBS. Each impedance spectrum curve had one resonant frequency, at which the impedance magnitude achieved its maximum. Around this resonant frequency, the phase of the impedance changes from +90 degrees to -90 degrees, indicating the system changes from inductance dominant to capacitance dominant. The resonant frequency increases as the inductance value decreases.

The measurement data were fitted with the model. The inductance and resistance of various inductors were measured separately. The fitting was performed iteratively. The initial trial value of stray capacitance was approximated from the impedance spectra measurement in PBS without any parallel inductor. The initial channel impedance with PBS was approximated by calculation of DC resistance given the channel geometry and the conductivity of PBS (1.6 S/m). Fig. 3-32 is the simulated impedance spectra with C_{st} = 1 pF, C_{dl} = 0.34 pF, and R = 50 kΩ for a system without inductors, and with C_{st} = 5 pF, C_{dl} = 1.7 pF, and R = 50 kΩ for a system with inductors. The inclusion of inductors on the printed circuit board introduces extra stray capacitance which increases C_{st}. Both the impedance magnitude and phase responses matched well with experimental data. Table 3-2 summarizes the measured and calculated resonant frequencies. $f_{0,meas}$ is the measured resonant frequency. $f_{0,num}$ is the frequency to achieve the largest impedance magnitude in numerical simulation. $f_{0,cal}$ is calculated using equation (3.12) with the definition of resonance. f_{0,cal_simple} is calculated from formula (3.16).

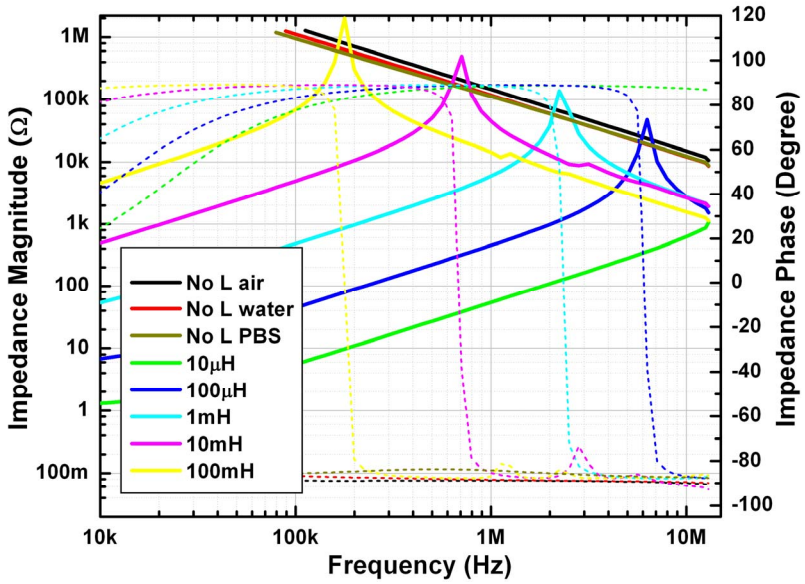

Figure 3-31 *Bode plots of measured system impedance responses in different environments and with various inductance values of inductor-induced resonance impedance sensor device I. The solid lines are impedance magnitude responses. The dash lines are impedance phase responses.*

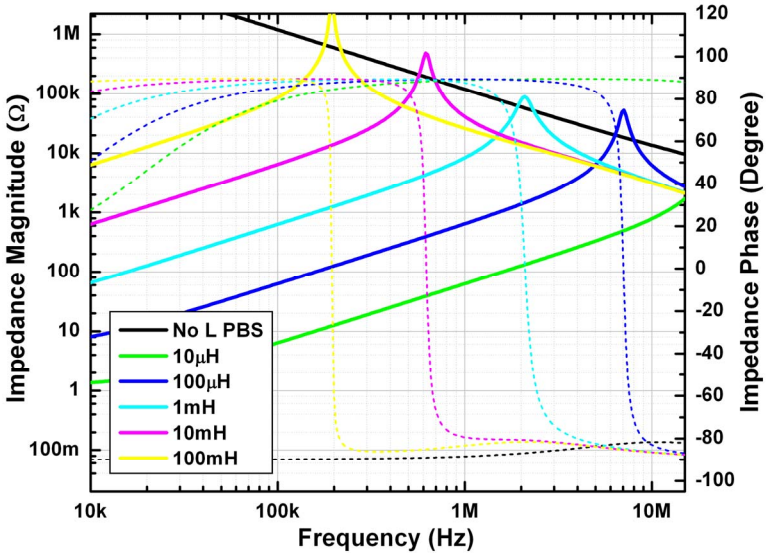

Figure 3-32 *Bode plot of simulated impedance response with various inductance values of inductor-induced resonance impedance sensor device I. The solid lines are impedance magnitude responses. The dash lines are impedance phase responses.*

Table 3-2 Calculation and measurements of resonance frequency for four cases of different parallel inductors

L (mH)	R_L (Ω)	$f_{0,meas}$ (MHz)	$f_{0,num}$ (MHz)	$f_{0,cal}$ (MHz)	f_{0,cal_simple} (MHz)
0.1	5.12	6.4	7.08	7.04	7.12
1	22	2.0	2.09	2.10	2.25
10	73	0.71	0.617	0.623	0.712
100	184	0.18	0.195	0.195	0.225

$f_{0,num}$ and $f_{0,cal}$ are almost identical; hence, when the system is in resonance, its impedance magnitude is maximized. Both $f_{0,num}$ and $f_{0,cal}$ are very close to $f_{0,meas}$, with maximal difference of approximately 10% for all four cases of different inductance values. The simple formula of (3.16), which was based on the assumption that the resonance was established mainly by the inductor and the stray capacitor, actually resulted in a very good approximation of the resonant frequency. This indicates that for this device, the added parallel inductor mainly nullifies the stray capacitor at resonant frequency. For conventional coil inductors used in testing, the inductance is proportional to the square of the number of coil turns, while the inductor resistance is proportional to the number of coil turns [24]. So the relationship of R_L and L can be fitted using the formula:

$$R_L = k\sqrt{L} \quad . \qquad (3.18)$$

From Table I, k was fitted to be 18.3 ± 1.6 Ω/mH$^{1/2}$. By plugging equation (3.18) into equation (3.12), the relationship between resonant frequency and inductance can be obtained. This relationship and the results from the simple resonant frequency approximation are plotted in Fig. 3-33A. The two curves almost overlap, especially in the low-inductance (high-resonant-frequency) region. The difference at high inductance

of 1 H is only approximately 16%. So for this device, equation (3.16) can be used to estimate the resonant frequency.

With the approximation equations (3.16) and (3.18) for f_0 and R_L, the relationship between Z_0 and f_0 is determined:

$$\frac{1}{Z_0} = 2\pi C_{st}^{3/2} k f_0 + \frac{1}{R[1 + \frac{1}{(2\pi C_{dl} R f_0)^2}]}. \qquad (3.19)$$

Asymptotic analysis shows four frequency ranges:

$$Z_0 = \begin{cases} \frac{1}{2\pi C_{st}^{3/2} k f_0} & (f_0 \le \frac{C_{st}^{3/2} k}{2\pi C_{dl}^{2} R}) \\ \frac{1}{4\pi^2 C_{dl}^{2} R f_0^{2}} & (\frac{C_{st}^{3/2} k}{2\pi C_{dl}^{2} R} \le f_0 \le \frac{1}{2\pi C_{dl} R}) \\ R & (\frac{1}{2\pi C_{dl} R} \le f_0 \le \frac{1}{2\pi C_{st}^{3/2} k R}) \\ \frac{1}{2\pi C_{st}^{3/2} k f_0} & (\frac{1}{2\pi C_{st}^{3/2} k R} \le f_0) \end{cases} \qquad (3.20)$$

For the device under investigation, the first range is below 10^{-9} Hz, the second is between 10^{-9} Hz and 1.6 MHz, the third is between 1.6 MHz and 5.7 GHz, and the fourth range is above 5.7 GHz. So the relevant frequency range in our measurement is in the upper second range and lower third range. Fig. 3-34B plots the impedance magnitude at resonance frequency (Z_0) versus resonance frequency (f_0). Measurement points corresponding to the peak positions in Fig. 3-31 are labeled.

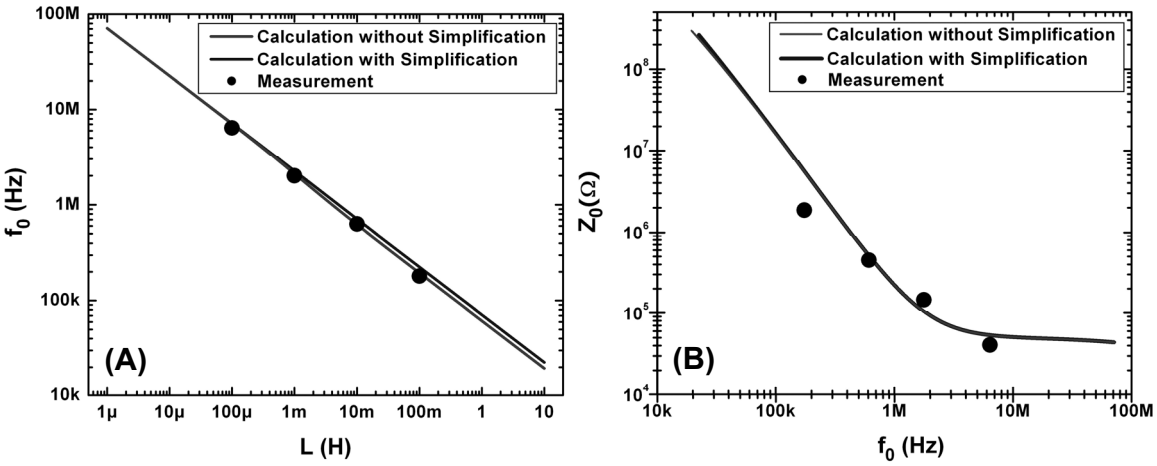

Figure 3-33 *Simulation and measurements for (A) resonance frequency and (B) impedance magnitude at resonance frequency of inductor-induced resonance impedance sensor device I. The red lines are calculation using formulas (2) and (3), which are directly derived from model. The blue lines are calculation with simplification using equations (6), (7), and (8). The black dots are measured points with extrapolation.*

3.3.5.2 Impedance spectra measurement of device II

An example of measured impedance spectra of device II is shown in Fig. 3-34. Due to the limitation of the LF impedance analyzer, the upper limit of frequency sweep range is 13 MHz and the upper limit of impedance magnitude is 1.2 MΩ. The measurement data were fitted with the model. The fitting was performed iteratively. The initial trial value of stray capacitance was approximated from the impedance spectra measurement in PBS without any parallel inductor. The initial channel impedance with PBS was approximated by calculation of DC resistance, given the channel geometry and the conductivity of PBS (1.6 S/m). Fig. 3-35 is the simulated impedance spectra with C_{st} = 5 pF, C_{dl} = 4 pF, and R = 40 kΩ for a system without inductors and with C_{st} = 1 pF, C_{dl}

= 0.5 pF, and R = 40 kΩ for a system connected with inductors. The inclusion of inductors on the printed circuit board introduces extra stray capacitance which increases C_{st}.

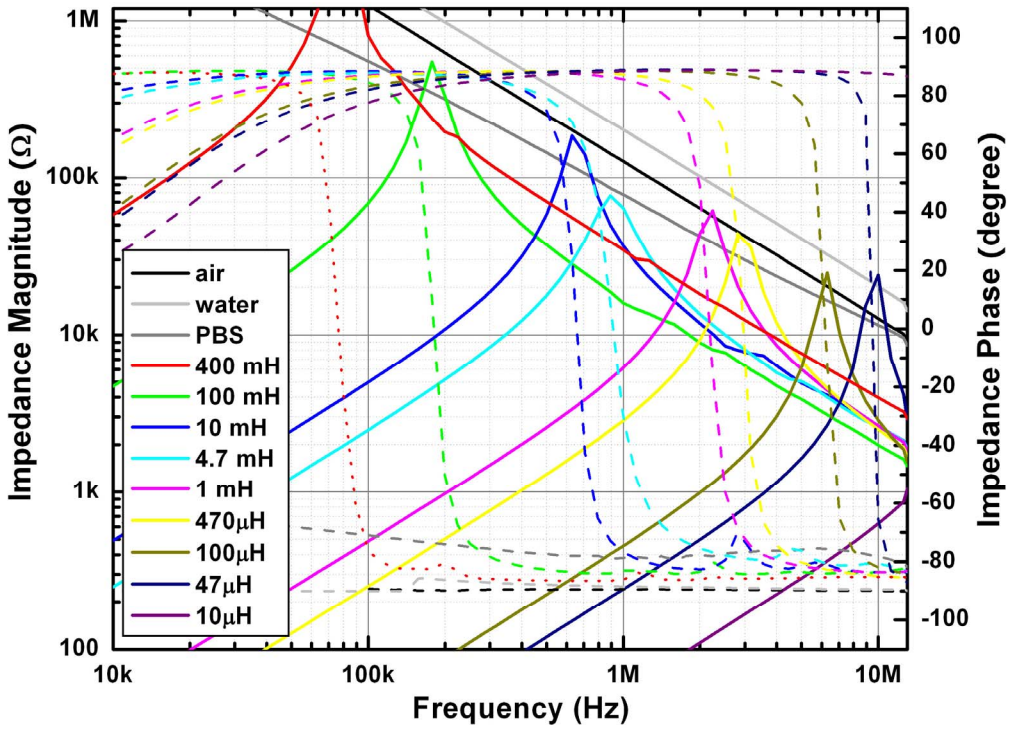

Figure 3-34 *Measured impedance magnitude (left axis and solid lines) and phase (right axis and dotted lines) spectra of inductor-induced resonance impedance sensor device II without inductor connected and filled with air, DI water, and electrolyte PBS, as well as device in PBS with inductors of various values connected.*

Similar to device I, the relationship between resonance frequency and inductance, as well as the relationship between the impedance magnitude at resonance frequency and the resonance frequency, are plotted in Fig. 3-36 for device II. The simplification is justified and the model fits the measurements.

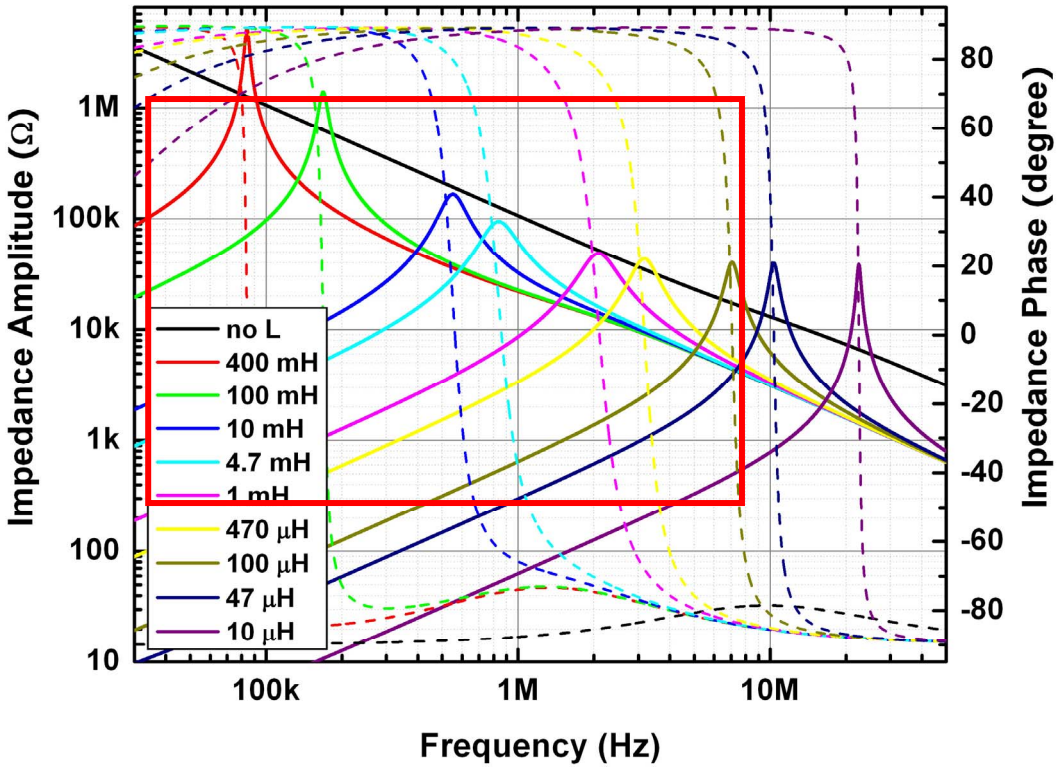

Figure 3-35 Simulated impedance magnitude (left axis and solid lines) and phase (right axis and dotted lines) spectra of inductor-induced resonance impedance sensor device II without inductor and with inductors of various values connected. Boxed range corresponds to the whole plot range in Fig. 3-34.

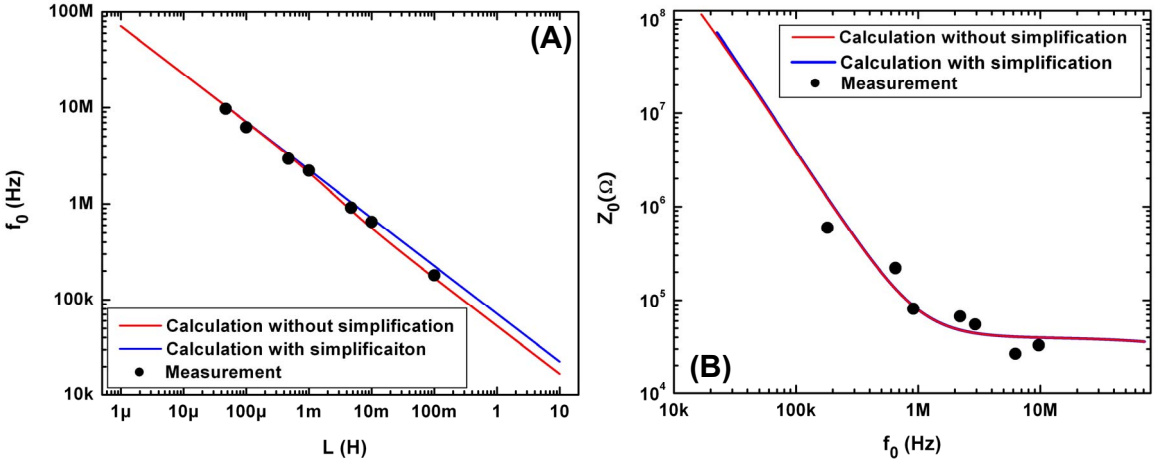

Figure 3-36 *Simulation and measurements for (A) resonance frequency and (B) impedance magnitude at resonance frequency of inductor-induced resonance impedance sensor device II. The red lines are calculation using formulas (2) and (3), which are directly derived from model. The blue lines are calculation with simplification using equations (6), (7), and (8). The black dots are measurement with extrapolation.*

3.3.6 Study on the sensitivity

The sensitivity of the measurement system to a parameter α is defined as:

$$S_\alpha = \frac{1}{|Z_{sys}|}\left|\frac{\partial Z_{sys}}{\partial \alpha}\right| \quad . \qquad (3.21)$$

From the above definition, we calculated the sensitivity to R, S_R, and to C_{dl}, S_{Cdl}.

S_R is a figure of merit for the system performance. Higher S_R indicates better system performance. C_{dl} can change with environment during measurement. S_{Cdl} is a measurement of system resistance to C_{dl} change during measurement. Lower S_{Cdl} indicates higher system performance. S_R versus frequency for five cases of various inductance values and for the case of no inductor are plotted in Fig. 3-37A for device I and in Fig. 3-38B for device II. All cases with an inductor connected have a single peak at the corresponding resonant frequency, while the case without a parallel inductor has a very broad peak. The peaks of S_R for all five cases of parallel inductors are one order of magnitude higher than the case without the parallel inductor, with the exception of the 1 mH inductance.

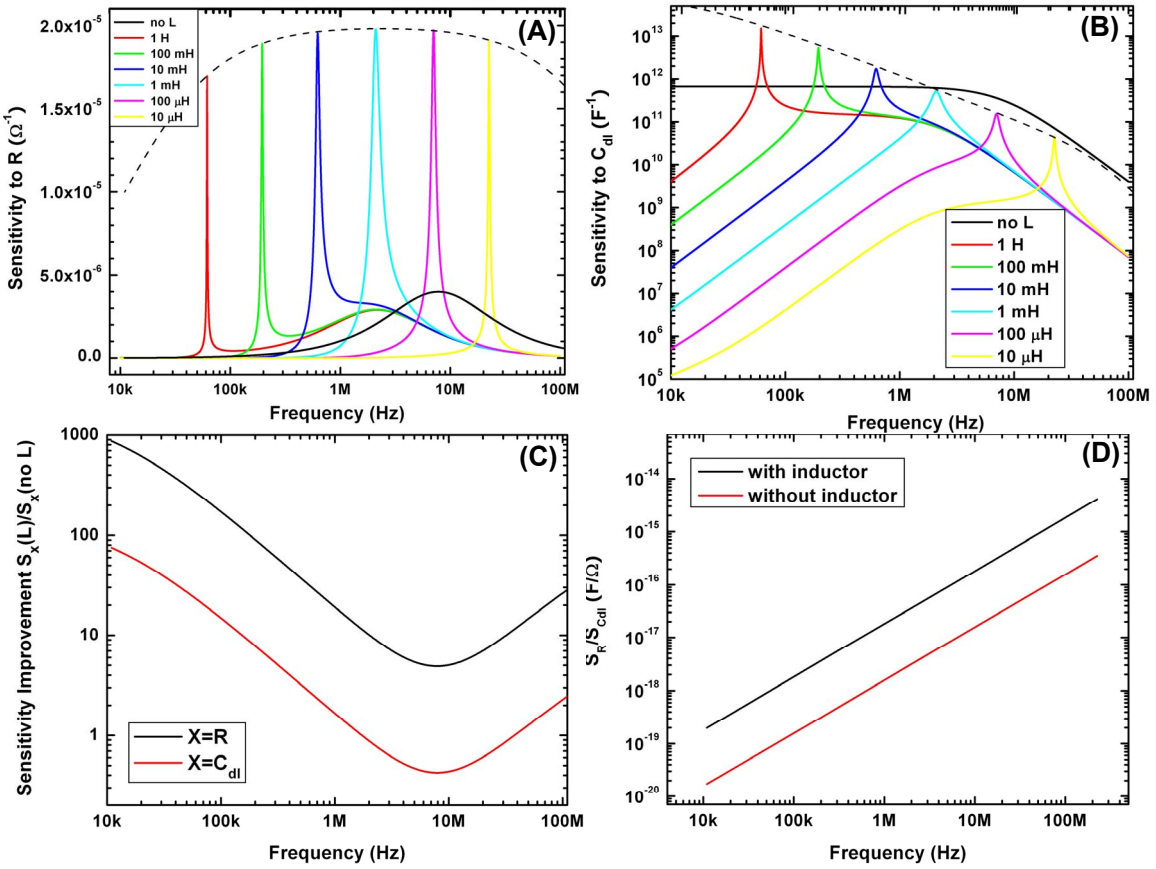

Figure 3-37 *Sensitivity study on inductor-induced resonance impedance sensor of device I. (A) The sensitivity to R for various parallel inductors and no inductor connected in device I. The curve without inductor overlaps with the high-frequency regions of the 10 mH and 100 mH cases. (B) The sensitivity to* C_{dl} *for various parallel inductors and no inductor connected. (C) Sensitivity improvement for R and* C_{dl}*. (D) Ratio of* S_R *and* S_{Cdl} *versus frequency with and without inductors.*

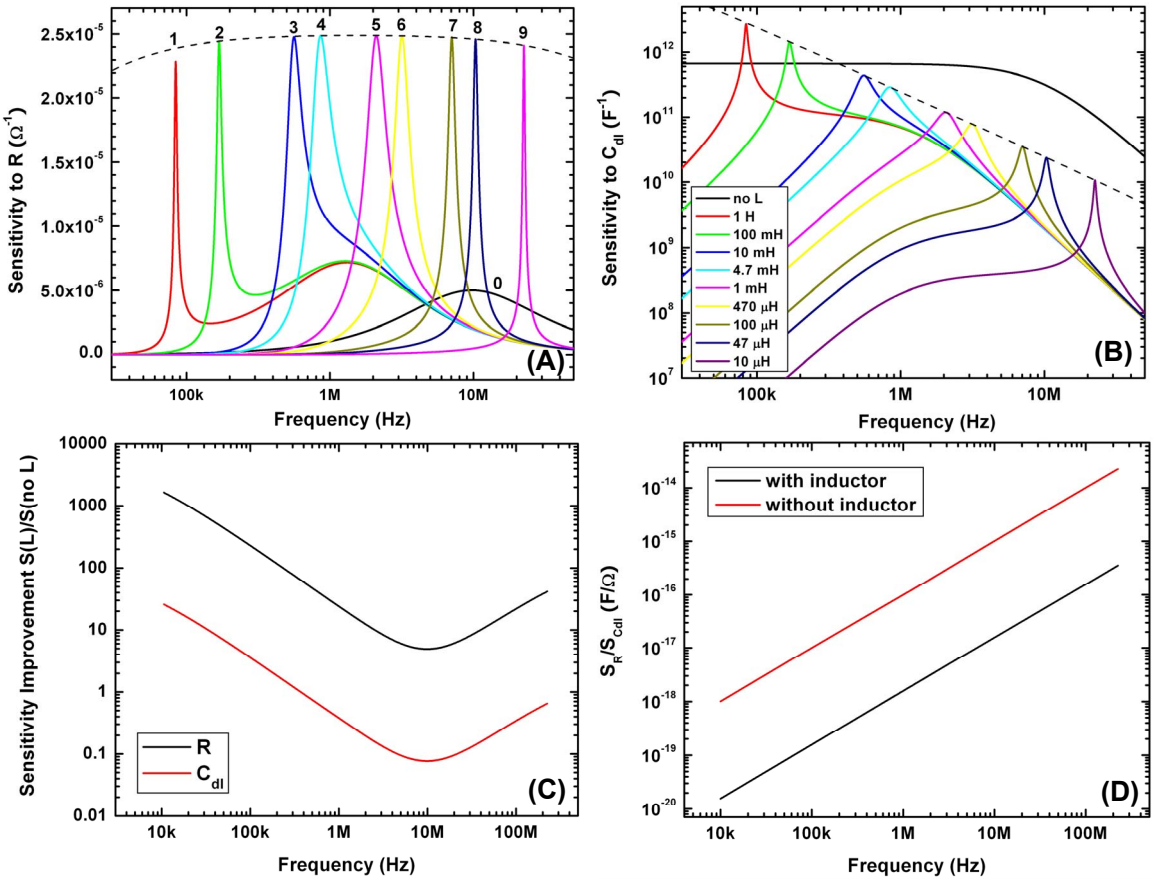

Figure 3-38 *Sensitivity study on inductor-induced resonance impedance sensor of device II. (A) The sensitivity to R for various parallel inductors and no inductor connected in device II. The curve without inductor overlaps with the high-frequency regions of the 10 mH and 100 mH cases. (B) The sensitivity to C_{dl} for various parallel inductors and no inductor connected. (C) Sensitivity improvement for R and C_{dl}. (D) Ratio of S_R and S_{Cdl} versus frequency with and without inductors.*

S_{Cdl} versus frequency for five cases of various inductance values and for the case without parallel inductor are plotted in Fig. 3-37B for device I and in Fig.3-38B for device II. All the cases with inductor connected also have a dominating single peak at

the corresponding resonant frequency, while the case without parallel inductor has a plateau in the low-frequency region.

It is interesting to note that there is a broad peak for the case without inductor connected and the peak centered on frequency $f_1 = \frac{1}{2\pi C_{dl} R}$. In cases with a parallel inductor connected, if the resonant frequency f_0 is lower than f_1, the effect of C_{dl} still shows up in the capacitance-dominated frequency range ($f > f_0$). A similar broad peak appeared in sensitivity plots Fig. 3-37A and Fig. 3-38A. On the other hand, if the resonant frequency f_0 is higher than f_1, this broad peak disappears because it is located in the inductance dominated frequency range ($f < f_0$) and the effect is dominated by the inductor.

Different from S_R, the maximal S_{Cdl} for smaller inductance is much smaller than that for larger inductance, which indicates sensing at a resonant frequency of smaller parallel inductance will result in fewer errors caused by the change of double-layer capacitance during measurement.

3.3.7 Flow sensing of polystyrene beads

3.3.7.1 Flow sensing of polystyrene beads in Device I

Fig. 3-39A shows an example of time trace of 5 μm polystyrene beads. The flow rate is 10nL/min. The particle concentration is in the range of 10^4 beads/μL. The peak height is 0.058 V ± 0.013 V for a sample of 249 beads. The duration of the peaks is 37.8 ms ± 6.8 ms, which corresponds well with the expected time that the beads passed the sensing zone. Fig. 3.39B is a typical peak from the same data set.

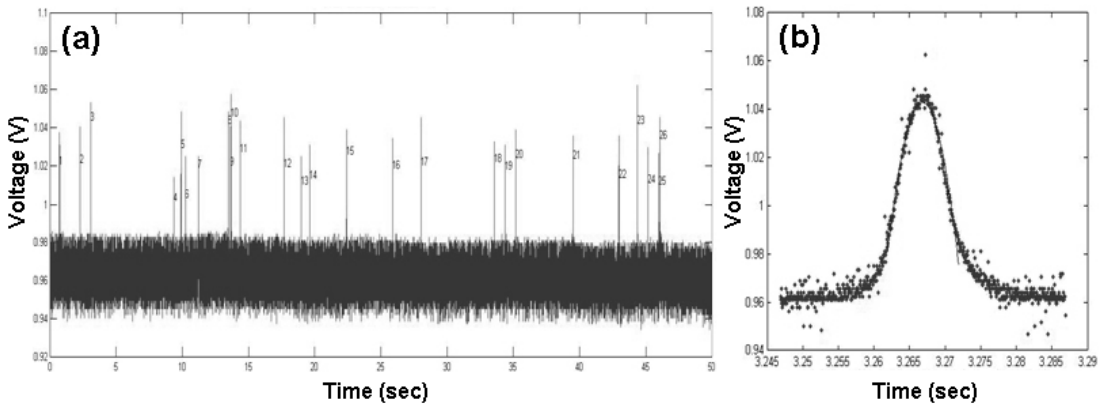

Figure 3-39 *Flow sensing of polystyrene beads in inductor-induced resonance impedance sensor device I (A) Time trace of 5 μm beads tested at resonant frequency of 104 kHz. Detected peaks are labeled. (B) A typical example peak of 8 μm beads tested at 104 kHz. The solid line is least-squares curve-fitting to a parabola.*

3.3.7.2 Flow sensing of polystyrene beads in device II

The devices are first validated with a mixture of 5 μm and 10 μm diameter polystyrene beads (Fig. 3-40). A scatter plot of impedance at high frequency versus that at low frequency showed two separated regions.

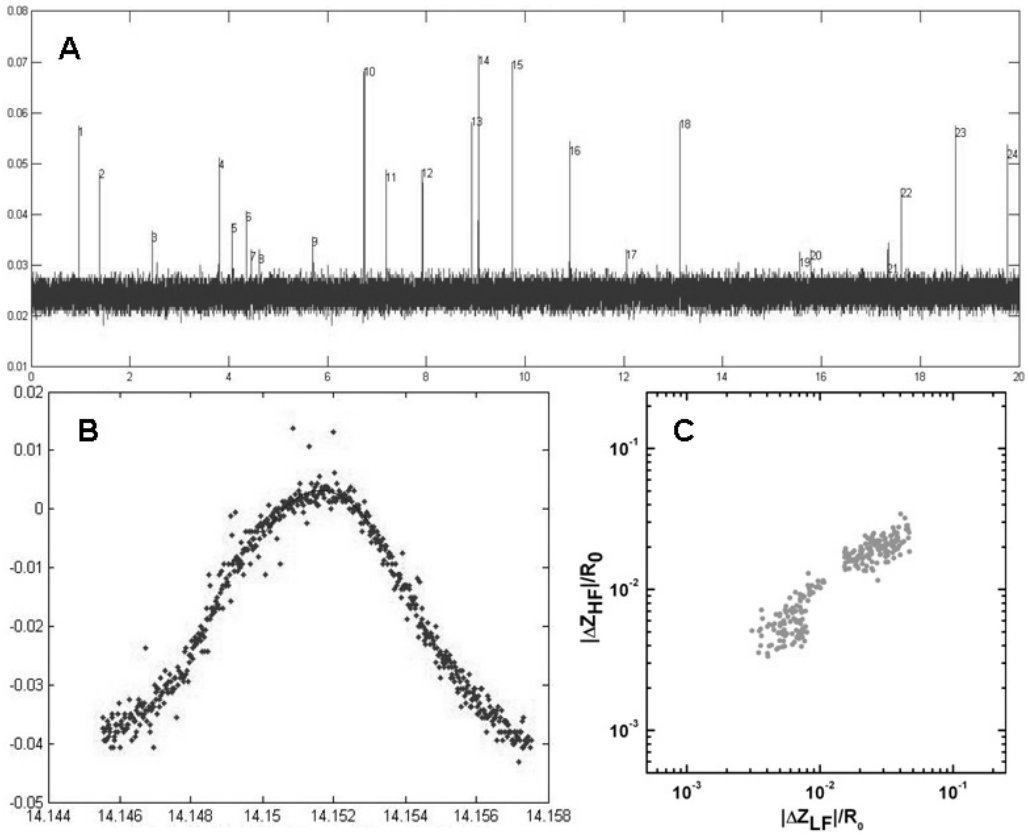

Figure 3-40 Testing with 5 μm and 10 μm polystyrene beads mixture in 20 μm channel dimension in inductor-induced resonance impedance sensor device II. (A) Time trace of 20 seconds. (B) Closeup of an individual peak. (C) Scatter plot of impedance magnitude..

3.3.8 Flow sensing of human blood cells

Human blood cell sensing was performed either with diluted whole blood or diluted leukocyte-rich plasma. Whole blood samples were obtained from healthy donors and used within 48 hours. Whole blood was used for erythrocyte characterization and leukocyte-rich plasma was used for leukocyte testing.

3.3.8.1 Single-frequency sensing in Device I

Fig. 3-41A shows a time trace for human whole blood diluted by one thousand times. Close-ups of peaks are shown in Fig. 3-41(B)-(D).

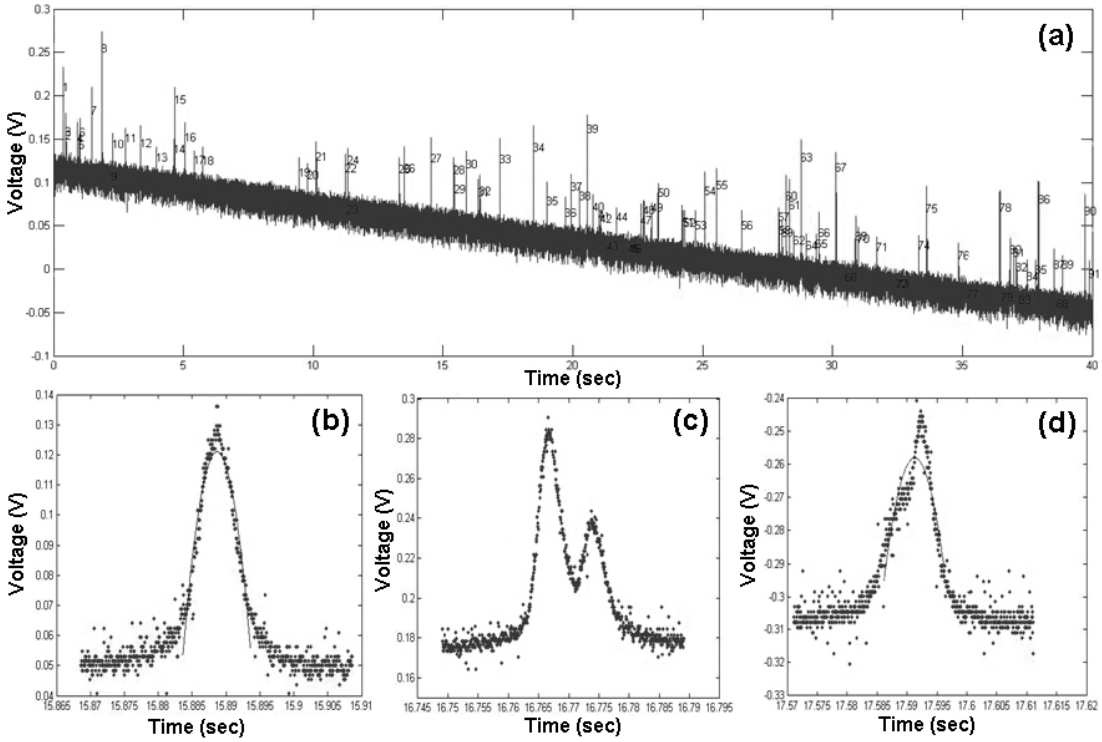

Figure 3-41 *Time traces of flow sensing of human blood cells in inductor induced resonance impedance sensor device I. (A): Time trace of diluted human whole blood tested at resonant frequency of 90.8 kHz. Detected peaks are labeled. (B)–(D): Sensing cells from diluted human whole blood. The solid lines are least-squares curve-fittings to parabola: (B) a typical peak, (C) two close peaks, (D) two peaks too close to be separated.*

It is well known that under DC and low-frequency AC excitation, the change of channel impedance is correlated to the volume of the particles including biological cells.

The relationship between the channel resistance change and particle volume at DC [27, 28] was used to calculate the change of total system impedance magnitude versus particle volume (Fig. 3-42). Based on our proposed system model, and fitting parameters obtained from impedance spectra measurement, we calculated the total system impedance magnitude change when a particle in size ranging from 5 μm diameter to 14 μm diameter enters the aperture. The data fits well onto a straight line. Hence, the volume of the particles can be determined from the change of total impedance magnitude at resonance.

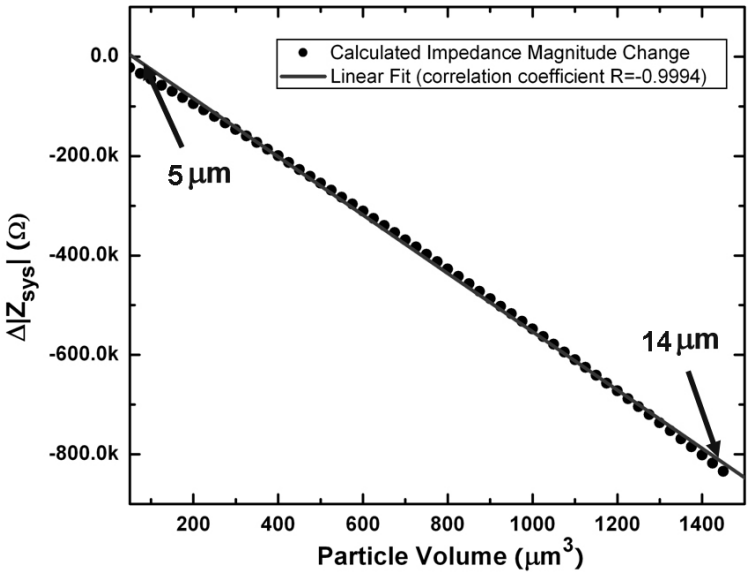

Figure 3-42 *Impedance magnitude change with the particle volume*

The peak height in Fig. 3-41 is approximately proportional to the change of total impedance magnitude. From Fig. 3-42, it is also approximately proportional to the particle volume. So, the peak height distribution can be used to measure the particle volume distribution. The peak height of blood cell traces (Fig. 3-41) had a wide distribution which indicates that the cell size varied. The histogram of pulse height

matched well with the known volume distribution of erythrocytes (Fig. 3-43). The tail part of the peak height histogram was contributed by leukocytes (Fig. 3-44), while the small pulse height portion (under 0.1 V) is presumably still dominated by erythrocytes. It resembles the known leukocyte volume distribution.

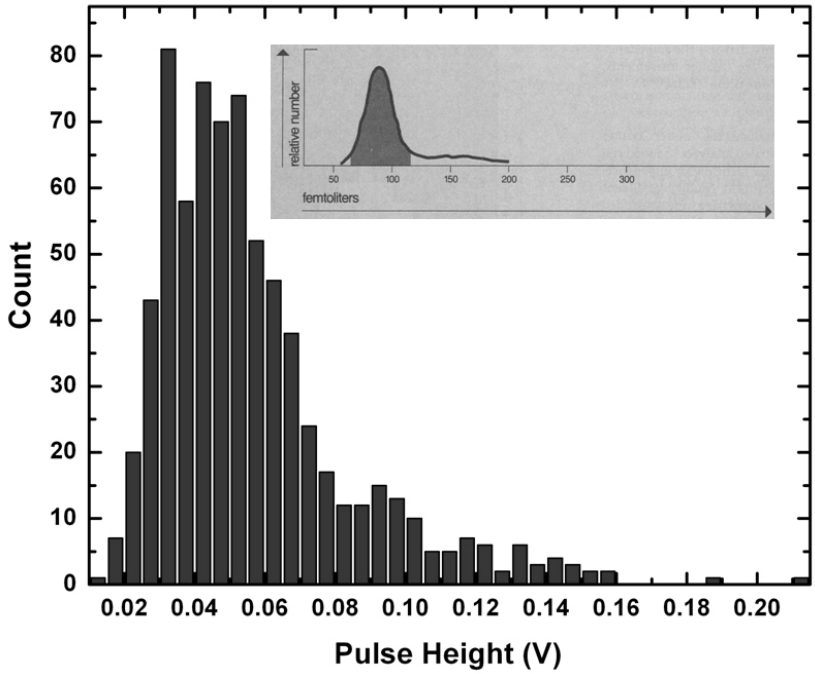

Figure 3-43 *Pulse height distribution of diluted human whole blood, in which leukocyte to erythrocyte ratio is about one to a thousand, in inductor-induced resonance impedance sensor device I. Inset is erythrocyte volume distribution from [23].*

Out of the 381 blood cell signals during the above testing with diluted whole blood, six coincident events like Fig. 3-41D were identified. There were also two cases of close peaks as shown in Fig. 3-41C. The coincident effect can be modeled as a Poisson process[29]. Cacluations using equation (3.2) results in a true count of 385.7. The difference between true count and observed count was 4.7, which is on the same order but a little less than the six coincident events observed. This might reflect

statistical fluctuation, but it is more likely caused by the tendency to aggregation among blood cells.

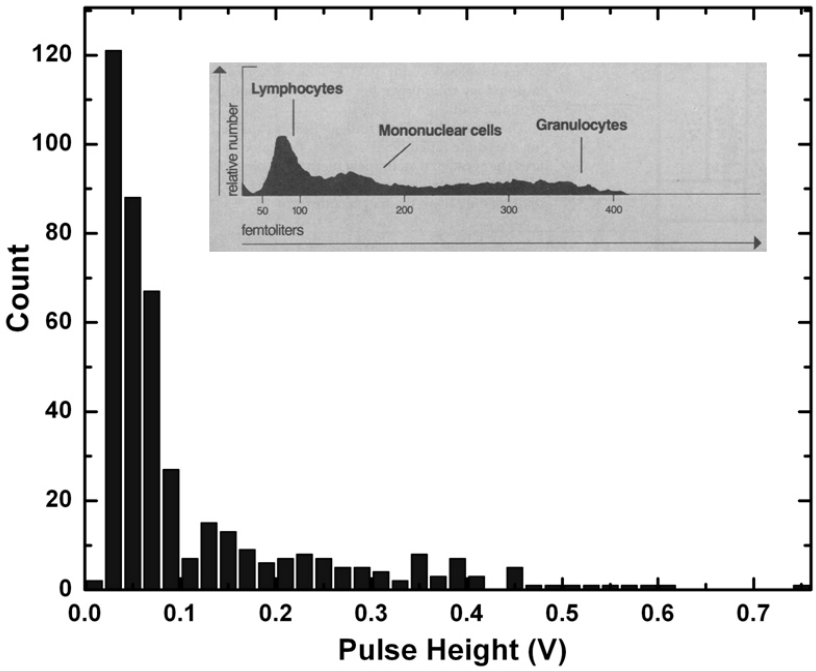

Figure 3-44 Pulse height distribution of leukocyte-rich plasma, in which leukocyte to erythrocyte ratio is about one to ten, in inductor-induced resonance impedance sensor device I. Top inset is leukocyte volume distribution from [23].

3.3.8.2 Dual-frequency sensing in device II

For human blood cell testing, two types of sample of blood cells were used. Diluted whole blood mainly shows the characteristic of the red blood cells (RBCs) because of the overwhelming number of RBCs over white blood cells (WBCs). Leukocyte rich plasma (LRP) was prepared with a WBC-to-RBC ratio on the order of 1:1. The difference between scatter plot of diluted blood and of LRP shows the characteristics

of WBCs (Fig. 3-45). WBCs have higher impedance magnitude for both frequencies than RBCs, but the opacity (the slope of fitted straight line) is similar.

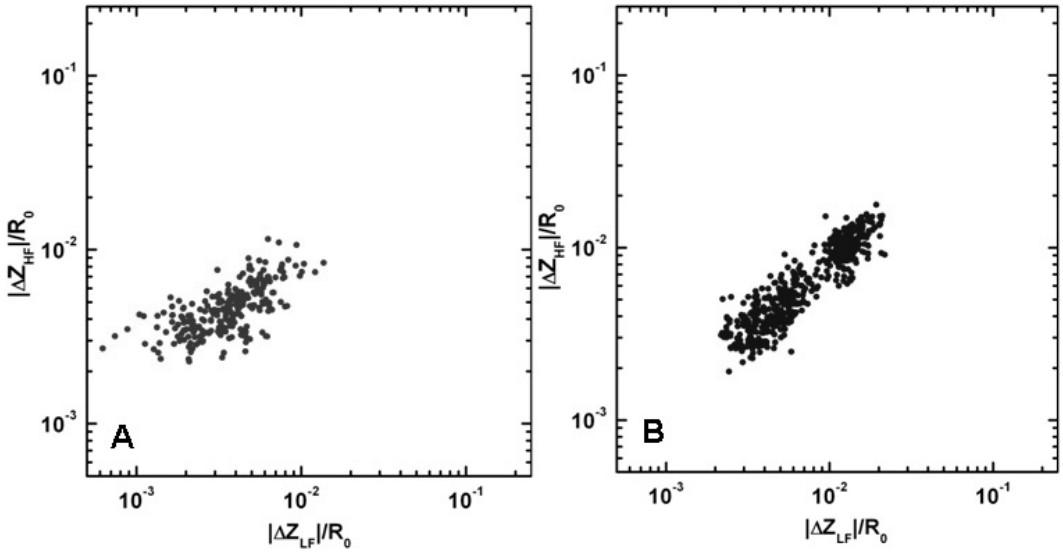

Figure 3-45 Scatter plots of testing with 200 times diluted human whole blood (A) and 1:1 diluted leukocyte-rich plasma (B) in 15 μm channel dimension inductor-induced resonance impedance sensor device I.

3.3.8.3 Tumor cell differentiation using dual-frequency sensing

Two epithelial tumor cell lines (breast adenocarcinoma MCF7, diameter 13.6 μm ± 1.3 μm; urinary bladder carcinoma T24, diameter 16.43 μm ± 1.16 μm) were used as models of tumor cell characterization. Both types of the tumor cells might be circulating tumor cells in the bloodstream. Fig. 3-46 shows scatter plots of each cell line with and without added blood. The diluted blood acted as an internal reference and also as a model system for detecting circulating tumor cells in blood. Both cell lines have a range of impedance values, but the opacity keeps relatively constant. Also they are distinctive

from blood cells, which can be the basis for detection and isolation of circulation tumor cells in the bloodstream.

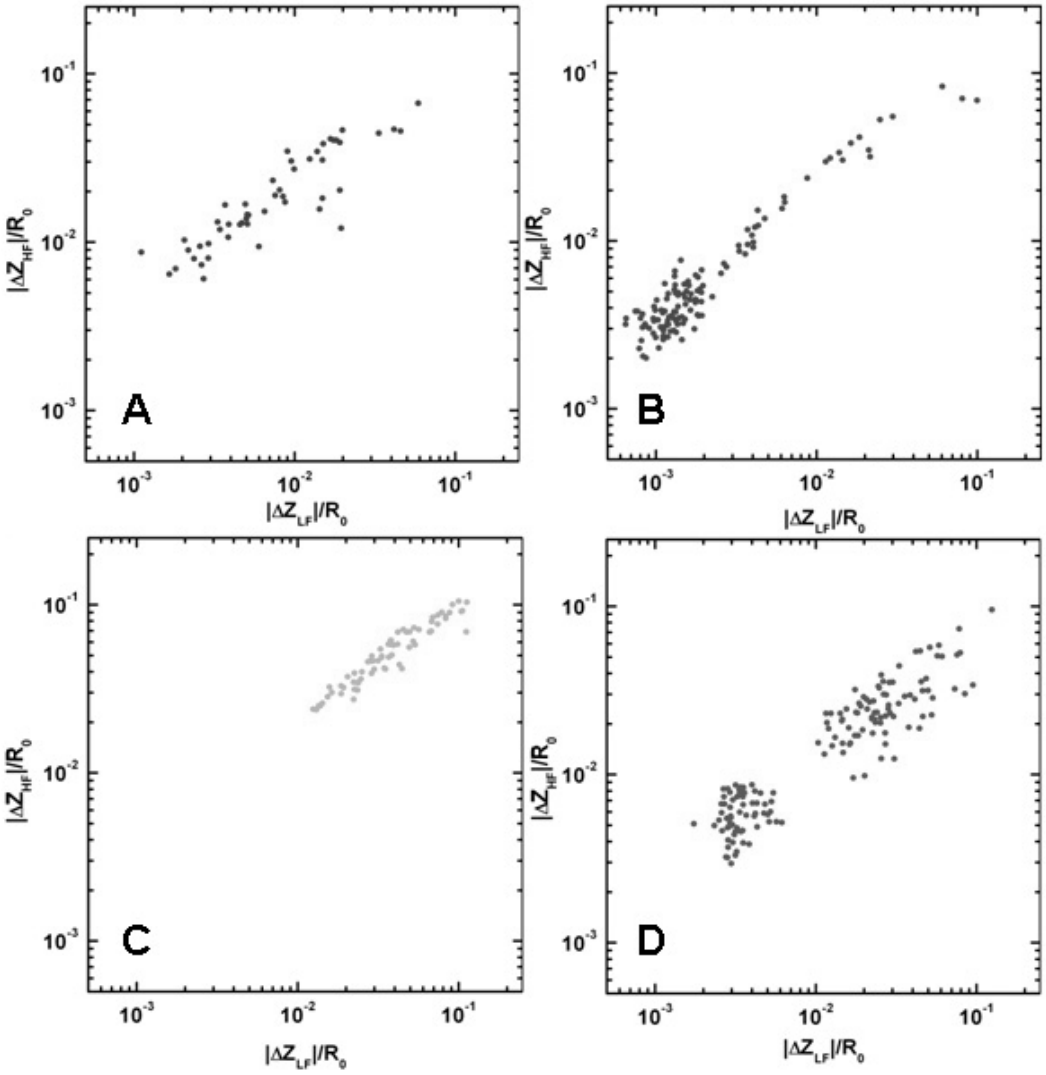

Figure 3-46 Scatter plots of testing with tumor cells spiked in diluted blood. (A) breast cancer cell line MCF7, (B) MCF7 mixed 1:1 with 1000 times diluted human whole blood, (C) bladder cancer cell line T24 and (D) T24 mixed 1:1 with 1000 times diluted human whole blood in 20 μm channel dimension devices.

The approach of inductor-induced resonance sensing can make the AC impedance particle sensing more flexible. Inductors of different inductance values can be connected to different electrode pairs closely placed in the same channel. In this way, the same particle can be probed at different resonant frequencies. For biological cells, cellular structures inside the cell membrane have different characteristics in the RF range (the β dispersion region). This approach can be used for cell identification and characterization.

3.4 Conclusions

To solve the problem of large double-layer impedance of electrodes in micro impedance sensors, two methods were proposed and successfully verified. One uses platinum black electroplating to increase the effective surface area of the electrode. The other includes a parallel inductor in the system, and sensing at the resonance frequency greatly increases the sensitivity.

For platinum black electroplated micro impedance sensors, two types of micro Coulter sensors were designed and fabricated for particle sensing in fluidic flow. One was based on integrated parylene technology. The other one was based on soft lithography. A system model was developed to explain the measurement results, which included the channel impedance, the constant phase element, and the stray capacitance. Platinum black electroplating was performed on the electrode surface so that the sensing zone in the frequency domain could be identified. The lower bound of the sensing zone was limited by the double-layer effect of the electrode-electrolyte interface. The upper bound was limited by the stray capacitance. The devices were calibrated with polystyrene beads of various diameters. We confirmed that the signal magnitude was

determined mainly by the size of the particles at the testing frequency. We demonstrated human erythrocyte and leukocyte sensing by platinum black electroplated micro electrodes with high signal-to-noise ratio. The histograms of the signal magnitude matched well with previous published volume distributions of the erythrocytes and leukocytes. The advantages of downsizing electrodes and the sensing zone in microdevices include increased sensitivity, lowered sample dilution factor, and thus increased system throughput.

The new approach of inductor-induced impedance sensing overcomes the problem of the small double-layer in micro impedance sensing for particles in fluidic flow. Two types of devices were designed and fabricated. One performs sensing at single frequency. The other can sense system impedance change at dual frequencies. Parallel inductors were introduced to induce system resonance. From impedance spectra measurements, a single peak was discovered for each inductance value. The inductor was shown to mainly cancel out the stray capacitance at the resonant frequency. Based on the model we developed, the sensitivity to the channel resistance was the highest at the resonant frequency and one order of magnitude larger than the system without the parallel inductor. The devices were first tested with 5 μm and 10 μm polystyrene beads. Human erythrocyte and leukocyte sensing was then demonstrated with this approach. For the device using single-frequency sensing, the histograms of the signal magnitude matched well with previous published volume distributions of the erythrocytes and leukocytes. For the device using dual-frequency sensing, the scatter plots clearly distinguish between 5 μm and 10 μm beads, as well as leukocytes and erythrocytes. The feasibility of detection of circulating tumor cells in blood was demonstrated by dual-frequency

resonance impedance sensing with blood samples spiked with cultured tumor cells. The advantages of downsizing electrodes and the sensing zone in microdevices include increased sensitivity, lowered sample dilution factor, and thus increased system throughput. The sensing frequency can be flexibly selected by changing the inductance.

3.6 Bibliography

[1] O. F. Schanne and E. Ruiz P-Ceretti, *Impedance Measurements in Biological Cells*. John Wiley & Sons, 1978.

[2] H. P. Schwan, "Linear And Nonlinear Electrode Polarization And Biological-Materials," *Annals Of Biomedical Engineering*, vol. 20, pp. 269–288, 1992.

[3] W. H. Coulter, "Means for counting particles suspended in a fluid," U. S. P. Office, Ed. U.S.A, 1953.

[4] K. Asami, "Characterization of heterogeneous systems by dielectric spectroscopy," *Progress In Polymer Science*, vol. 27, pp. 1617–1659, 2002.

[5] K. Asami, Y. Takahashi, and S. Takashima, "Dielectric properties of mouse lymphocytes and erythrocytes," *Biochim Biophys Acta*, vol. 1010, pp. 49–55, 1989.

[6] A. Irimajiri, Y. Doida, T. Hanai, and A. Inouye, "Passive electrical properties of cultured murine lymphoblast (L5178Y) with reference to its cytoplasmic membrane, nuclear envelope, and intracellular phase," *Journal of Membrane Biology*, vol. 38, pp. 209–32, 1978.

[7] K. Asami and T. Yamaguchi, "Dielectric-Spectroscopy Of Plant-Protoplasts," *Biophysical Journal*, vol. 63, pp. 1493–1499, 1992.

[8] J. H. Nieuwenhuis, F. Kohl, J. Bastemeijer, P. M. Sarro, and M. J. Vellekoop, "Integrated Coulter counter based on 2-dimensional liquid aperture control," *Sensors and actuators. B, Chemical*, vol. 102, 44, 2004.

[9] S. Zheng, M. Liu, H. L. Kasdan, and Y. C. Tai, "Platinum Black Electroplated Impedance Particle Sensor," *Presented at First Annual IEEE International Conference on Nano/Micro Engineered and Molecular Systems (IEEE-NEMS 2006)*, Zhuhai, China, 2006.

[10] D. Satake, H. Ebi, N. Oku, K. Matsuda, H. Takao, M. Ashiki, and M. Ishida, "A sensor for blood cell counter using MEMS technology," *Sensors and actuators. B, Chemical*, vol. 83, 77, 2002.

[11] D. W. Lee, S. Yi, and Y.-H. Cho, "A flow-rate independent cell counter using fixed control volume between double electrical sensing zones," *presented at 18th IEEE International Conference on Micro Electro Mechanical Systems (MEMS 2005)*, Miami Beach, Florida, USA, 2005.

[12] H. G. Chun, T. D. Chung, and H. C. Kim, "Cytometry and velocimetry on a microfluidic chip using polyelectrolytic salt bridges," *Analytical Chemistry*, vol. 77, pp. 2490–2495, 2005.

[13] S. Gawad, K. Cheung, U. Seger, A. Bertsch, and P. Renaud, "Dielectric spectroscopy in a micromachined flow cytometer: theoretical and practical considerations," *Lab On A Chip*, vol. 4, pp. 241–251, 2004.

[14] H. E. Ayliffe, A. B. Frazier, and R. D. Rabbitt, "Electric impedance spectroscopy using microchannels with integrated metal electrodes," *Journal Of Microelectromechanical Systems*, vol. 8, pp. 50–57, 1999.

[15] S. Zheng, M. Liu, M. S. Nandra, and Y.-C. Tai, "Platinum Black Electroplated Impedance Sensors for Human Blood Cell Counting," (*submitted)*.

[16] S. Gawad, L. Schild, and P. Renaud, "Micromachined impedance spectroscopy flow cytometer for cell analysis and particle sizing," *Lab On A Chip*, vol. 1, 76, 2001.

[17] M. P. Maher, J. Pine, J. Wright, and Y. C. Tai, "The neurochip: a new multielectrode device for stimulating and recording from cultured neurons," *Journal Of Neuroscience Methods*, vol. 87, pp. 45–56, 1999.

[18] D. A. Robinson, "The electrical properties of metal electrodes," *Proceedings of IEEE*, vol. 56, 1968.

[19] W. H. Mulder, J. H. Sluyters, T. Pajkossy, and L. Nyikos, "Tafel Current At Fractal Electrodes—Connection With Admittance Spectra," *Journal Of Electroanalytical Chemistry*, vol. 285, pp. 103–115, 1990.

[20] A. J. Bard and L. R. Faulkner, *Electrochemical Methods: Fundamentals and Applications, 2nd Ed.* New York, NY: John Wiley & Sons, Inc., 2000.

[21] J. Xie, Y. N. Miao, J. Shih, Q. He, J. Liu, Y. C. Tai, and T. D. Lee, "An electrochemical pumping system for on-chip gradient generation," *Analytical Chemistry*, vol. 76, pp. 3756–3763, 2004.

[22] S. R. Quake and A. Scherer, "From micro- to nanofabrication with soft materials," *Science*, vol. 290, pp. 1536–1540, 2000.

[23] S. B. McKenzie, *Clinical Laboratory Hematology*. Prentice Hall, 2004.

[24] C.-Y. Shih, W. Li, S. Zheng, and Y.-C. Tai, "A Resonance-Induced Sensitivity Enhancement Method for Conductivity Sensors," *presented at IEEE SENSORS 2006*, Daegu, Korea, 2006.

[25] W. Li, D. C. Rodger, E. Meng, J. D. Weiland, M. S. Humayun, and Y.-C. Tai, "Flexible parylene packaged intraocular coil for retinal prostheses," *presented at the 4th International IEEE-EMBS Special Topic Conference on Microtechnologies in Medicine and Biology (MMB 2006)*, Okinawa, Japan, 2006.

[26] M. B. Reed, *Alternating-current circuit theory*, *2nd ed*. New York: Harper, 1956.

[27] E. C. Gregg and K. D. Steidley, "Electrical Counting And Sizing Of Mammalian Cells In Suspension," *Biophysical Journal*, vol. 5, 393, 1965.

[28] O. A. Saleh and L. L. Sohn, "Quantitative sensing of nanoscale colloids using a microchip Coulter counter," *Review Of Scientific Instruments*, vol. 72, pp. 4449–4451, 2001.

[29] M. Mazumdar and K. L. Kussmaul, "A Study Of Variability Due To Coincident Passage In An Electronic Blood Cell Counter," *Biometrics*, vol. 23, 671, 1967.

CHAPTER 4

LEUKOCYTE DIFFERENTIAL FROM UNDILUTED WHOLE BLOOD

4.1 Introduction

Leukocytes (white blood cells, WBCs) respond to toxic, infectious and inflammatory processes to defend tissues and eliminate disease process or toxic challenges [1]. Accurate and prompt counting and differentiation of leukocytes is critical for differentiating between bacterial and viral infectious disease, recognizing malignant disease such as leukemia and the presence of and staging of HIV, assessing allergic conditions, and monitoring bone marrow function or the body's response to various treatments [2].

4.1.1 Methods of leukocyte differential

Leukocyte differential currently can be performed either manually or by conventional automated blood analyzers. Manual leukocyte differential analysis began over 100 years ago, when Paul Ehrlich stained cell nucleus and cytoplasm granules with aniline dyes developed for the textile industry and found that leukocytes show different colors [3]. Manual blood analysis requires making a blood smear or the use of hemacytometers and then counting by a trained professional. One of the Romanowsky stain (i.e., Giemsa, Jenner, Wright, or Leishman stain) procedures, which are based on cell affinity for neutral, basic, or acidic dyes, is normally used in the procedure for a 5-part differential. It is time consuming, labor intensive, and error prone.

Between the manual blood smear count and automated flow-cytometer-based conventional blood counters, there were also attempts to use a computer-controlled microscope to differentiate leukocytes based on structure and coloration of nucleated blood cells which had been fixed and stained in a blood smear [4–9]. They were largely unsuccessful in practical diagnostic settings due to their inability to improve precision under the requirement of substantial throughput increase, and the inability of algorithmic structural identification of leukocyte subtypes to replace the professional morphologist.

Automated blood counters are usually based on flow cytometry and employ one or a combination of electrical impedance sensing, light scattering measurement, and chemical or immuno staining followed by optical sensing. In electrical impedance sensing, RBCs are removed by lysing reagent saponin, or some more sophisticated lysing reagent including surfactants. During the lysing process, the leukocyte cell volume changes depending on cell type, due to the leakage of cytoplasm contents and cell

nucleus shrinkage in varying amounts [10]. Thus normally 2-part (lymphocytes versus granulocytes) or even 3-part (lymphocytes, neutrophils, and other leukocytes) leukocyte differential can be achieved by simply electrical impedance measurement of particle volume [11−15]. Combining DC and AC impedance, special acidic hemolysis in basophil channel and alkali hemolysis in eosinophil channel, a 5-part leukocyte differential can be achieved [16]. Due to the dynamics of the lysis procedure, dilution, mixing, temperature, and time need to be perfectly controlled, so fully automated instruments are required for reliable 3-part and 5-part differential. Later optical methods based on light scattering and fluorescence staining of organelles, granules, and nuclei becomes an alternative method. Generally, low-angle scattered light contains information on cell size and high-angle scattered light can be used to probe internal composition of the cell. To achieve 5-part differential, eosinophils requires some special stain to change its scattering characteristics from other granulocytes, and basophils need to be counted separately after differential lysis of other leukocytes [1, 10]. The first flow-cytometer-based automated optical leukocyte differential instrument, Hemolog-D by Technicon, uses three different channels: lymphocytes, neutrophils, and eosinophils classified by myeloperoxidase staining; monocytes identified by staining intracellular nonspecific esterase; and basophils identified by Alcian blue staining [17]. Later, Coulter Electronics, Inc., combined electrical impedance and light scattering and developed their VCS technology, which uses DC resistance sensing to measure cell volume; AC impedance sensing to collect information on cell size and internal structure (including chemical composition and nuclear volume); and light scattering for cellular granularity, nuclear lobularity, and cell surface structure [4]. Generally speaking, conventional

automated blood analyzers are bulky, expensive, and mechanically complex. They require larger sample volumes and generate more waste than the systems developed using microdevices. They are usually found only in hospitals or central laboratories, and it normally takes from hours to even days for a patient to get the results.

Micro blood counters promise to provide a point-of-care solution. They cost less and can be more accurate than a manual count. Particle (bead, erythrocyte, and cultured cell) counting has been demonstrated, for example, by electrical impedance sensing [18–21], light scattering detection [22, 23] and fluorescent sensing [21, 24–27] in microsystems. All of these previous studies use diluted samples. Here human leukocyte counting and differentiation with microfabricated devices from undiluted human blood is reported for the first time. Dilution is normally required as one of the sample preparation steps in blood cell counting and differentiation. There are several reasons for this. First dilution prevents the coincidence effect in which multiple cells appear in the detection zone simultaneously. Because of the ratio of erythrocytes to leukocytes is on the order of a thousand to one, for electrical impedance or light scattering detection of leukocytes, a blood sample dilution factor from one hundred to several tens of thousand is typically required to avoid erythrocyte interference. Even for counting leukocytes in samples where leukocytes are specifically fluorescent labeled, a dilution of at least ten times is performed. Secondly, dilution reduces the risk of sample clogging in the flow chamber. This is a major concern for macroscopic blood counters, since the flow chamber is used in continuous mode and removing the clog or replacing the flow chamber can be difficult. The third reason is that the whole blood is diluted during the chemical hemolysis process to remove erythrocytes, especially when electrical impedance or light-scattering detection

is employed. Hemolysis can produce inaccurately high leukocyte counts due to lysis-resistant erythrocytes, and inaccurately low counts because some leukocytes are lysed. Finally in some protocols an additional fixation buffer is required to conserve the properties of leukocytes.

4.1.2 Optical-sensing-based flow cytometers

Although the first automated differential blood counters commercially available were image analyzers that scanned blood smears prepared with either Giemsa's or Wright's staining, modern automated blood analyzers are mainly based on flow cytometers. One difference between them is that blood counters require volume measurement while flow cytometers do not. Also a lot of the flow cytometers have cell sorting capability by electrically and/or mechanically diverting and collecting cells after sensing.

Applications of flow cytometry typically involve using fluorescent probes to stain cellular components or functions. Optical fluorescent sensing was introduced in flow cytometry in the late 1960s [28, 29]. Fluorescent sensing in flow cytometry is more precise than static or scanning cytometry due to the short and uniform sensing time and thus limited photobleaching. It is also more sensitive than absorption measurements because of its dark field nature. Modern flow cytometers can take "snapshots" of single cells with a throughput up to approximately 50,000 cells/second [26, 30]. The measured cellular properties can be morphological, biochemical and functional, such as size, shape, DNA/RNA content, cell surface markers, cell cycle distribution and viability.

With the advance of microfabrication, microdevices have been investigated to replace glass capillary-based flow chambers, integrate compact optics and provide on-

chip sample transport. Glass and silicon [23, 31–34], fused silica or quartz [35, 36], PMMA [22, 37], polyimide [18, 38], plastic Mylar [39], and PDMS [25, 26, 36, 40–44] have been used as building materials for micro flow cytometers. Samples are transported by syringe pump [18, 22, 23, 31, 33, 35, 37–39, 42, 45], compressed air [25, 43–45], vacuum pump [38, 46], or electro-osmotic flow [32]. In most cases liquid 2D or even 3D sheath flow is used, but in some cases air sheath flow [41] or no sheath flow [23, 31] are demonstrated. Optical waveguides and solid-state devices have been integrated in micro flow cytometers [27, 37, 42]. For leukocyte differential in micro devices based on optical sensing, a V-groove microchannel was fabricated by anisotropic wet etching of silicon and 3-part leukocyte differential was demonstrated for diluted blood without sheath flow by 2-parameter light scattering [23].

Currently there are a number of commercially available, general purpose portable flow cytometers, including the Beckman Coulter Cell Lab Quanta™ SC (http://www.beckmancoulter.com), the Partec CyFlow® SL-3 (http://www.partec.de), and the Guava Personal Cell Analysis (PCA) System (http://www.guavatechnologies.com). More related to the work described in this chapter are ultracompact or portable flow-cytometer-based automated hemacytometers commercially available or under development. Beckman Coulter's COULTER® Ac·T™ Series analyzers (http://www.beckmancoulter.com) achieve a 5-part leukocyte differential using electrical impedance sensing, light absorbance after cytochemical staining with Sudan Black B [47] and Chlorazol Black E [48], and differential acidic lysis (for a basophil differential from the rest of the leukocytes). Drew Scientific Excell 22 (www.drew-scientific.com) uses multi-dimensional light scattering and electrical impedance sensing to achieve 5-part

leukocyte differential in one minute. Micronics, Inc., in cooperation with Beckman Coulter, Inc., is in development of a portable flow cytometer, which claims to provide complete blood count using a droplet of whole blood in less than five minutes (www.micronics.net). The plastic devices are fabricated with thin-film laminate-based technology. Leukocyte differential is performed in one of three channels by multi-angle light scattering after RBC lysis. The other two channels are for hemoglobin and RBC, platelet count [39]. Although the above commercial systems are portable, they are still bigger, heavier, use more sample/reagents and generate more waste by at least one order of magnitude than the technology described in this chapter. For leukocyte differential, these systems require RBC lysis and sample dilution.

4.1.3 Acridine orange and other fluorescent dyes for leukocyte differential

To avoid hemolysis, various fluorescent dyes that stain specifically for leukocytes have been used for leukocyte differential. In this way, only leukocytes generate signals and normal erythrocytes do not interfere. Acridine orange was first suggested [49−51] and then later become the first fluorescent stain used to aid leukocyte count in blood counters in addition to light scattering measurement in the early 1960s [52]. Although it was noted that acridine orange could be used to discriminate mononuclear cells from granulocytes, the device was never actually built for leukocyte differentials [53]. Later in early 1970s, researchers from Bio/Physics Systems demonstrated a 3-part differential with acridine orange [54−56], but again it was not commercialized. About the same time, a research group from Block Engineering found a three-dye combination for leukocyte differential: basic dye ethidium bromide stains for DNA; the other two acidic dyes—brilliant sulfaflavine and stilbene disulfonic acid derivative (LN), which have

different pKs—had different affinity for cell proteins of different pKs [57, 58]. So neutrophil granules are stained primarily with LN and eosinophils with sulfaflavine. Later it was showed the dye combination could be simplified to ethidium bromide and sulfaflavine with scattering measurements. Later other dyes were suggested for leukocyte differential, such as oxazine dyes [59−61], basic orange 21 [62], and a polymethine dye [63].

Another group of labeling reagents is the fluorescence labeled monoclonal antibodies [64−72]. The antibody-based labeling reagents are used to solve the problematic counting of monocytes and basophils in manual and automated hemacytometers. Due to the length and the cost of the procedures, they are used mainly in reference methods. For example, a flow cytometric method performing a five-part leukocyte differential based on three-color staining with anti-CD45-fluorescein isothiocyanate (FITC), anti-CD-14-phycoerythrin (PE)/Cy5, and a cocktail of PElabeled anti-CD2, anti-CD16, and anti-HLA-DR antibodies was proposed and evaluated as a reference method [70].

The approach demonstrated here for leukocyte differential is to stain an undiluted whole sample with acridine orange. Acridine orange (3,6-dimethylaminoacridine) belongs to a group of acridine dyes isolated in the late nineteenth century. It is a pH-sensitive fluorescent cationic dye. It is hydrophobic in neutral pH. It has an absorption maximum at 433 nm and fluorescence maximum at 521 nm in ethanol. If a large excess of nucleic acid polymers is added in, its fluorescence emission can increase by up to three fold [73, 74]. It binds strongly to double-stranded DNA by electrostatic attraction and intercalation of the acridine nucleus between base pairs. Upon binding, the

excitation maximum becomes 502 nm and the emission maximum becomes 525 nm (green). It also binds strongly to RNA and single-stranded DNA, with a shifted excitation maximum of 460 nm and an emission maximum of 650 nm (red). Because it is hydrophobic in neutral pH, it can easily diffuse through the cell membrane and cell nucleus membrane to bind to RNA and DNA. In living cells, acridine orange is protonated in the acidic environment of lysosomes, which makes it cationic and prevents it from leaking out of lysosome membranes. The aggregated acridine orange fluoresces orange so that lysosomes can be labeled [75]. When it is used in leukocyte analysis, the cell nucleus is stained green with slightly mixed red because of double stranded DNA and single stranded RNA, while the cell cytoplasm is stained red because of RNA and lysosomes [51]. Leukocyte count can be achieved by using the strong signal from the green fluorescent channel. Differentiation can be achieved by analyzing the signal from the red fluorescence channel since different types of leukocytes have different cytoplasm compositions. Red fluorescence intensity emission of leukocytes is lower than that of non-lymphocytes for samples stained over fifteen minutes. For fresh-stained leukocytes, a three-part differential (lymphocytes, monocytes, and granulocytes) can be achieved by studying the red fluorescent signal of an acridine stained diluted blood sample [54, 56]. But the counting has to be performed quickly since monocyte fluorescence intensity continues to increase, eventually preventing its differentiation from granulocytes. A five part differential of leukocytes (lymphocytes, monocytes, neutrophils, eosinophils, and basophils) has been demonstrated with hypotonic dilution and fresh acridine-orange-stained leukocyte samples [55].

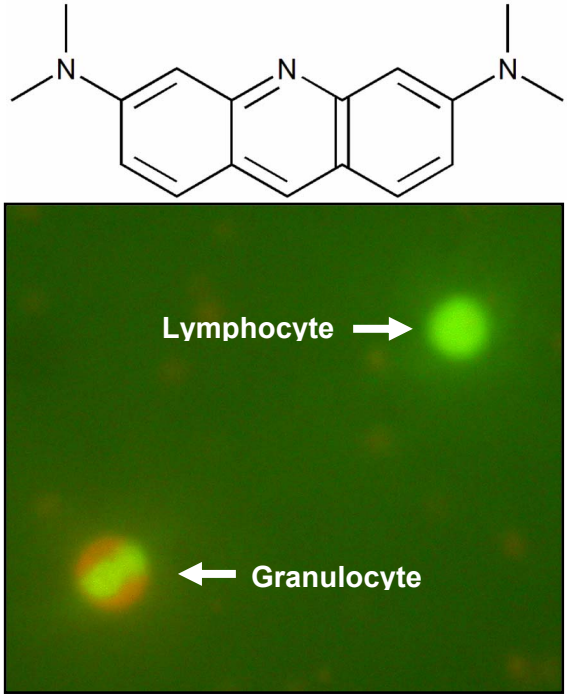

Figure 4-1 *Acridine orange molecular structure (top) and leukocyte staining results with it (bottom).*

In the following sections of this chapter, a method for leukocyte differential and its implementation in microdevices for leukocyte counting and differentiation without sample dilution are described. Leukocytes stained with acridine orange in an undiluted blood sample were counted and differentiated in a micro flow cytometer. The detection zone of the devices is miniaturized so that the average distance between leukocytes is longer and the coincidence effect can be minimized. The device is disposable so that the risk of clogging during device life is very low. Using fluorescent dye acridine orange to stain leukocytes specifically means that hemolysis and fixation are not required. Examining a blood sample without dilution simplifies sample preparation. This is especially attractive for a lab-on-a-chip system, since sample mixing and buffer storage

may complicate the overall system design. It has been demonstrated that acridine orange and anticoagulant can be coated on a device wall [76], so it is possible to apply a blood drop directly onto the device without any sample preparation.

4.2 Device design and fabrication

The device was fabricated using soft lithography [77]. PDMS and glass were chosen as the materials to make the device because of ease of fabrication and the excellent optical properties in the wavelengths used in this study. The channel structure was molded on a 1 cm by 1 cm PDMS block. To accommodate the working distance of the optical lens, the thickness of the PDMS block was controlled to be less than 3 mm. The channel depth was 16 μm.

As in Fig. 4-2, hydrodynamic focusing was adopted to control the particle position in the detection zone. In our design, the ratio of cross-sectional area of sheath flow to core sample flow was ten to one. The channel width of the detection zone was 50 μm. Considering the parallel flow profile, the width of the focused sample flow should be less than 5 μm. A filter structure upstream of the sample flow zone was designed to filter out contaminants, erythrocyte rosettes, and other large particle aggregates to prevent clogging in the detection zone.

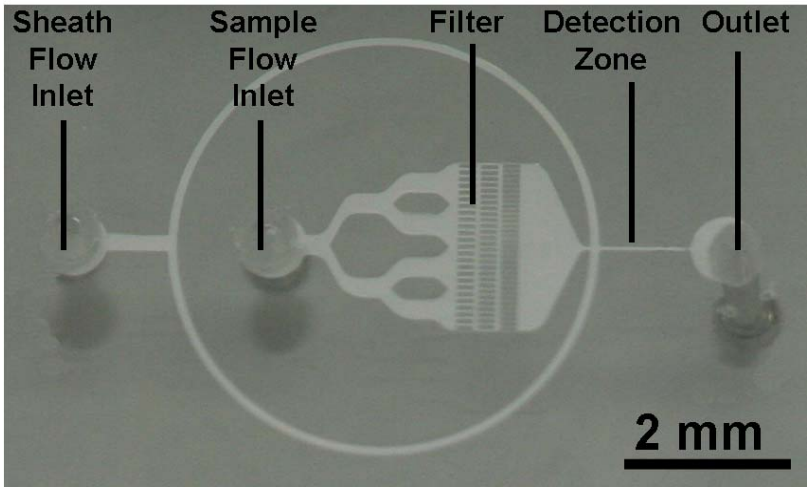

Figure 4-2 *Top view of the fabricated device.*

4.3 Material and testing setup

4.3.1 Materials

PDMS (polydimethylsiloxane) (Sylgard 184) was obtained from Dow Corning, Midland, MI. 5 μm green fluorescent polystyrene beads were purchased from Duke Scientific Corporations, Fremont, CA. Cell nucleus stain acridine orange was obtained from Molecular Probes, Eugene, OR, and dissolved in water to achieve a 10 mg/mL stock solution. Blood diluent Ficoll-Paque Plus was purchased from Amersham Biosciences, Sweden. 10x phosphate buffered saline (PBS) was obtained from Ambion (9625), Austin, TX.

4.3.2 Blood sample preparation and handling

Fresh human blood was obtained from healthy donors and used within three days. EDTA was added to the blood collection tube to prevent coagulation. For acridine orange staining, the stock solution was added to obtain a final dye concentration of 10 μg/mL. Staining results were observed under a fluorescent microscope (Nikon E800,

Japan) with a triple band filter block DAPI-FITC-TRITC, which has excitation filter wavelengths of 385−400 nm, 475−490 nm, and 545−565 nm, and emission filter wavelengths of 450−465 nm, 505−535 nm and 580−620 nm. Images were taken with a cooled CCD camera (RT-KE color 3-shot, Diagnostic Instruments, Sterling Heights, MI). Rough count of leukocytes was made with a hemacytometer (Hausser Scientific, Horsham, PA). When necessary, blood or fluorescent beads were diluted in Ficoll-Paque Plus (specific gravity 1.077 g/mL) to match the specific gravity of the solvent to leukocytes. All fluids were pumped into the devices using syringe pumps (Harvard Apparatus Pico Plus, Holliston, MA).

4.3.3 Optical detection system construction

The optical system was set up on an optical bench. It is a transmitted laser induced fluorescent (LIF) detection system. An Ar laser (National Laser NLC210BL, 488 nm, 15 to 30 mW adjustable, Salt Lake City, UT) was used as the excitation source. An aperture of 50 μm diameter was put in front of the laser output to facilitate the alignment process and lower the illumination intensity. An optional laser-line bandpass filter (bandwidth equal to 1.9 nm with a central wavelength of 488 nm) was used to further purify the laser source. An optional neutral density filter (NDF) was used to attenuate laser excitation. Alternatively, the pinhole and NDF were replaced by two linear glass polarizers (Edmond Optics TECH SPEC, Barrington, NJ) so that the illumination level on the device could be easily adjusted. A long-working-distance microscope objective (USMCO M Plan Apo, 10x, 0.28 NA, Dayton, NV) was used as a condenser lens. Another long-working-distance microscope objective (Bausch & Lomb, 50x, 0.45 NA, Rochester, NY) was used as an objective lens. Three emission filters were

used in our test: 488 nm long pass filter (Chroma HQ500LP, transition width < 4.9 nm, edge steepness = 2.5 nm, Rockingham, VT), a green bandpass filter with central wavelength 525 nm and bandwidth 50 nm (Chroma D525_50m), and a red bandpass filter with central wavelength 650 nm and bandwidth 50 nm (Chroma D650_50m). A broadband non-polarizing hybrid cube beamsplitter (Newport 05BC17MB.1, 400 nm−700 nm, R/T=45%/45%, Irvine, CA) was used to direct light to the photodiode detector and CCD camera simultaneously. The signal was electrically amplified and detected either with a Silicon photodiode receiver module (Electro-Optical Systems, UVS-025-H, Phoenixville, PA) or a photon multiplier tube (PMT, Hamamatsu H5784-20, Japan). The voltage signal was sent to a deep memory oscilloscope (HP 54645A, Palo Alto, CA). When the buffer in the oscilloscope was full, the data was loaded to a computer and analyzed with a Matlab peak-detection program. Video was taken with an analog CCD camera (Hitachi KP-D20B, Japan) at 30 frames per second and then converted to digital format and stored in a computer.

The detection system was constructed on an optic bench. Unlike most traditional fluorescent detection systems, the constructed laser-induced fluorescent system used a transmitted fluorescent configuration instead of a reflective (Epi) configuration. This eliminated the need for dichroic mirrors and made the overall alignment procedure straightforward.

As shown in Fig. 4-3, an Argon laser with 488 nm wavelength was used as the excitation source. The light was limited by either a pin hole and NDF, or alternatively by two linear polarizers. The neutral density filter was normally used in alignment so that the center of laser illumination was easily identified. During experiments, it was

normally removed so that maximal illumination could be achieved. Because of the narrow bandwidth of the laser system, the emission filter is optional. A long-working-distance 10x microscope objective was used as a condenser lens to focus illumination light onto the microdevice detection zone. Four centimeters distance between the condenser lens and the microdevice left enough space for fluidic connections. The device was positioned so that the illumination light went through PDMS first, and then the glass substrate. Transmitted light and fluorescent light then went through a long-working-distance, high-numerical-aperture objective lens. An emission filter was used to filter out transmitted light 488 nm Ar laser. Acridine-orange-stained leukocytes display mainly green fluorescence centered at 525 nm, but also some orange centered at 650 nm, depending on the type of leukocytes. In our testing, both long pass and various band pass filters were used. The long pass filter passed both emission wavelength bands. Band pass filters selected either the band centered at 525 nm or 650 nm. A beamsplitter cube was used to direct 45% of the light to the CCD camera and 45% to photodiode detector. The CCD camera was a good tool for alignment. The photodiode detector and PMT were more sensitive than the CCD camera and had a much faster time response. During testing, the optical system was first roughly aligned on a dummy device with the aid of images from CCD camera. A 10 μm diameter illumination spot on the detection zone could be easily achieved with proper alignment.

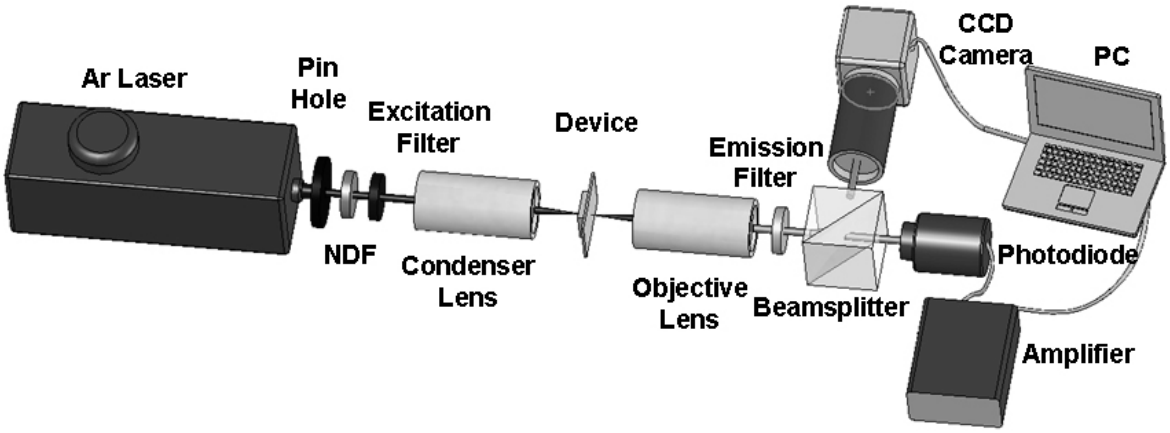

Figure 4-3 *Optical system setup*

4.3.4 Photobleaching time constant measurement

The time constant of photobleaching was characterized by filling the device with acridine-orange-stained whole blood. The channel was scanned by the laser spot and the entire process was recorded with a CCD camera. Whenever a fluorescing leukocyte was observed with fluorescent emission clearly distinct from the background, we stopped moving the laser spot and waited until the leukocyte was photobleached to background level. The images were extracted from the video, converted to 8-bit gray scale images, and analyzed with a Matlab program. The data was fitted to a single time-constant exponential decay.

4.4 Acridine orange staining study

4.4.1 Optimal staining concentration

To achieve a high signal-to-noise ratio, it is important to measure the optimal acridine orange concentration for leukocyte staining. 1 μg/mL range was used for machine counting of leukocytes in ten to twenty-five times diluted blood sample [54].

Because of the autofluoresence of acridine orange and its absorption by erythrocytes and platelets, higher concentrations of acridine orange increased the background noise. Lower concentrations did not provide enough contrast to distinguish leukocytes from background. So there should be an optimal acridine orange concentration to achieve the highest signal-to-noise ratio. To find the optimal concentration of acridine orange for leukocyte staining, a series of whole blood samples were stained with acridine orange of different concentrations (Fig. 4-4). Samples were loaded into a hemacytometer and observed under a microscope. 10 μg/mL (Fig. 4-4D) gave the highest signal-to-noise ratio when viewed using a fluorescent microscope. Lower concentration yielded incomplete staining and longer sensor integration time would be required. Higher concentration increased background fluorescence and thus reduced the signal-to-noise ratio.

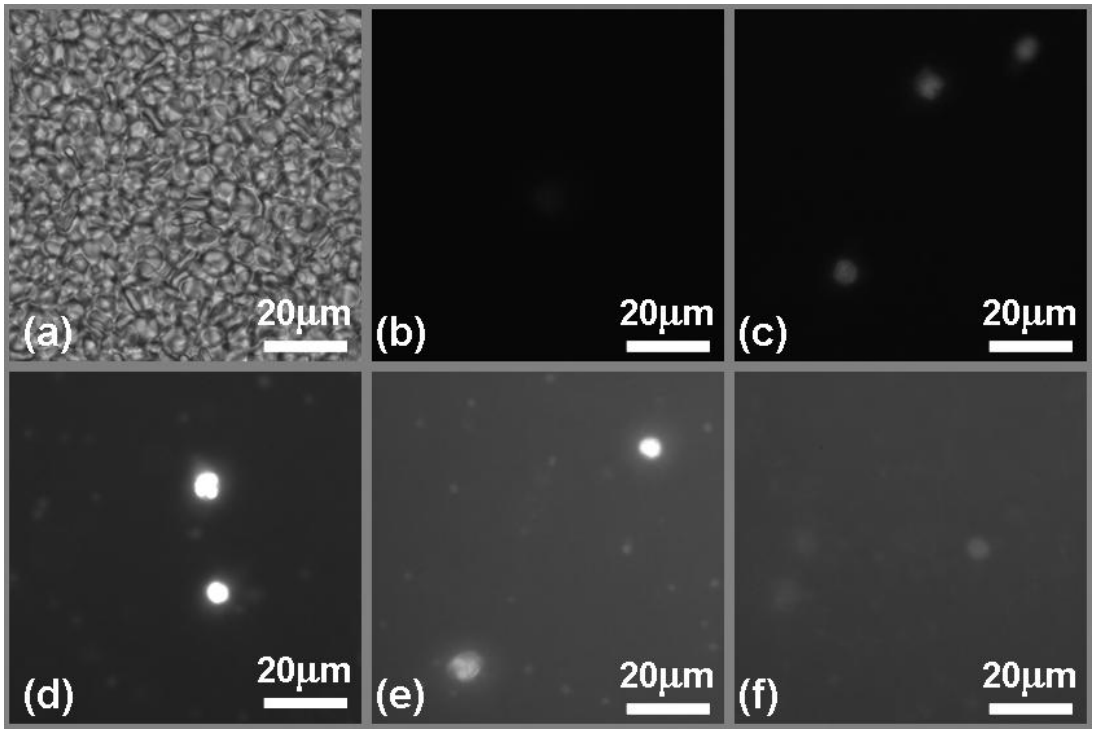

Figure 4-4 *Study of the optimal acridine orange concentration of leukocyte staining in whole blood. All the pictures were taken with fluorescent microscope using a 40x objective with the same settings for camera except the exposure time for the last one was one fifth of the others. (A) Bright field showing the majority erythrocytes. (B)-(F): Epi fluorescent images with acridine orange concentration of 100 ng/mL, 1 μg/mL, 10 μg/mL, 100 μg/mL, and 1 mg/mL.*

Using a fluorescent microscope, background fluorescence was observed for acridine-orange-stained whole blood. This background fluorescence could come from several sources. First, free or nonspecifically bound acridine orange will fluorescence green, although the quantum yield is three times lower [74]. Secondly, erythrocytes are reported to be able to absorb acridine orange and reduce the effective stain concentration for leukocytes [60]. Thirdly, erythrocytes in whole blood have a basal autofluorescence level with Ar laser illumination and 530 nm detection [78]. Aging-related oxidation

stress increases this level. Aged red blood cells produce lipofuscin, which strongly fluorescences red under green excitation and usually appears as small intracellular structures [79]. Another possible reason is the accumulation of acridine orange in platelets, which is related to the low cytosolic pH generated by membrane proton pumps [80]. Using a fluorescent microscope with 40x objective, we observed the background fluorescence bleached faster than leukocyte fluorescence, and it was accompanied by destruction of erythrocytes. It is reported that erythrocytes are destroyed faster than leukocytes because they lack an endomembrane for cell surface repair [81]. Also we noticed that aged blood samples had an elevated background level. These seem to support the idea that at least part of the background fluorescence comes from red blood cells. We also observed small particles (1−2 μm) with orange/red fluorescence that bleached slower than the background. It is unclear to us whether they are platelets or structures of destructed erythrocytes.

The distance between the coverslip and grid surface was 100 μm, so under the field of view there were stacks of erythrocytes as in Fig. 4-4A, but these erythrocytes did not block the fluorescent signal from leukocytes, which suggested that erythrocytes did not absorb much in the excitation and emission wavelengths.

4.4.2 Measurement of photobleaching time constant

The photobleaching effect for acridine-orange-stained leukocytes inside the device was studied. The illumination was set to be the same as that used in testing. One typical testing result is shown in Fig. 4-5. The signal was noisy but can be fitted as a first-order exponential decay with time constant of 6.4 ± 0.7 second. Two more tests confirmed the time constant was between 1 and 10 seconds.

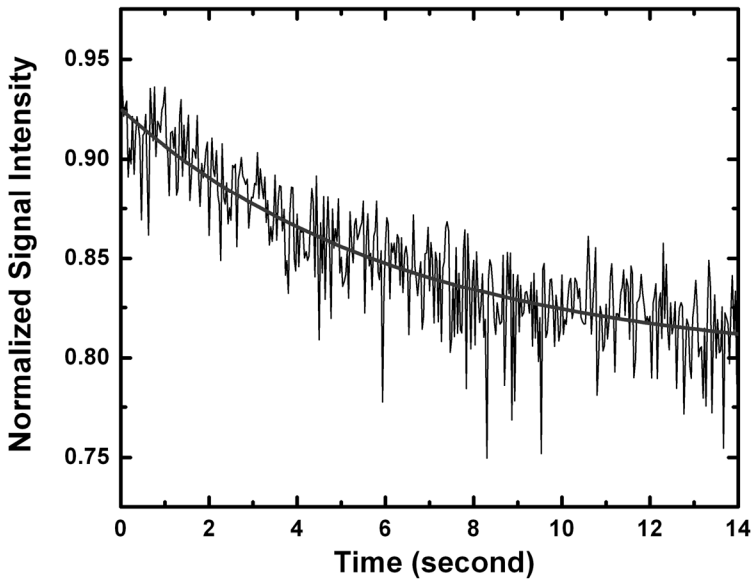

Figure 4-5 *Fluorescent signal bleaching from a single leukocyte in the device. The red line is a single exponential fit to the data.*

For acridine-orange-stained whole blood, photobleaching was observed for both background and leukocytes. The time constant of leukocyte photobleaching is one limitation on the lower bound for the sample flow rate for a given illumination intensity. If the photobleaching time constant is much smaller than the time a typical leukocyte takes to pass the laser focused spot, it is possible that the fluorescence signal from the leukocyte will be bleached even before it reaches the center of the focused spot. The fluorescence change from a single acridine-orange-stained leukocyte inside the channel under laser illumination was measured. The results could be fit by an exponential decay with a single time constant. The time constant fell in the seconds range. The time for one cell to pass the detection zone in our testing was roughly 30 ms for low flow rate and 1ms for high flow rate. So photobleaching was not a problem in our experiments. The measured time constant was on the same order of magnitude as that for samples observed under the 40x objective of the fluorescent microscope.

4.5 System calibration with 5 μm beads

The overall system was calibrated with 5 μm green fluorescent beads. The beads were diluted with Ficoll-Paque Plus and PBS to a final concentration of about 2×10^3 /μl. Sample flow rate was set to be 3 nL/min and sheath flow was 30 nL/min. Fig. 4-6 shows images from the CCD camera. With a focused laser beam as in Fig. 4-6A, the beads created a enlarged light circle as in Fig. 4-6B. Only a single bead normally appeared in each image. With diffused laser illumination as in Fig. 4-6C, the trace of the bead could be identified (Fig. 4-6D). To evaluate the effectiveness of the hydrodynamic focusing, we analyzed the center positions of all 81 bead events in a period of seven minutes. The beads flowed at the center of the channel with a standard deviation of 0.7 μm (Fig. 4-7). Although hydrodynamic focusing adds an additional solution and requires flow control, it provides several benefits. It limits the cross-section area of the detection zone without shrinking the channel diameter, thus the signal-to-noise ratio is improved without increasing the chance of channel clogging. Also the reduction of the cross section of the core flow reduces the coincidence effect. Finally, enclosing the core sample flow with sheath flow minimizes fluorescent dye absorption in the device walls, thus reducing background noise. Fig. 4-8 shows 5 μm bead signals from the photodiode detector. The detector was set at high sensitivity mode. Peaks could be easily identified.

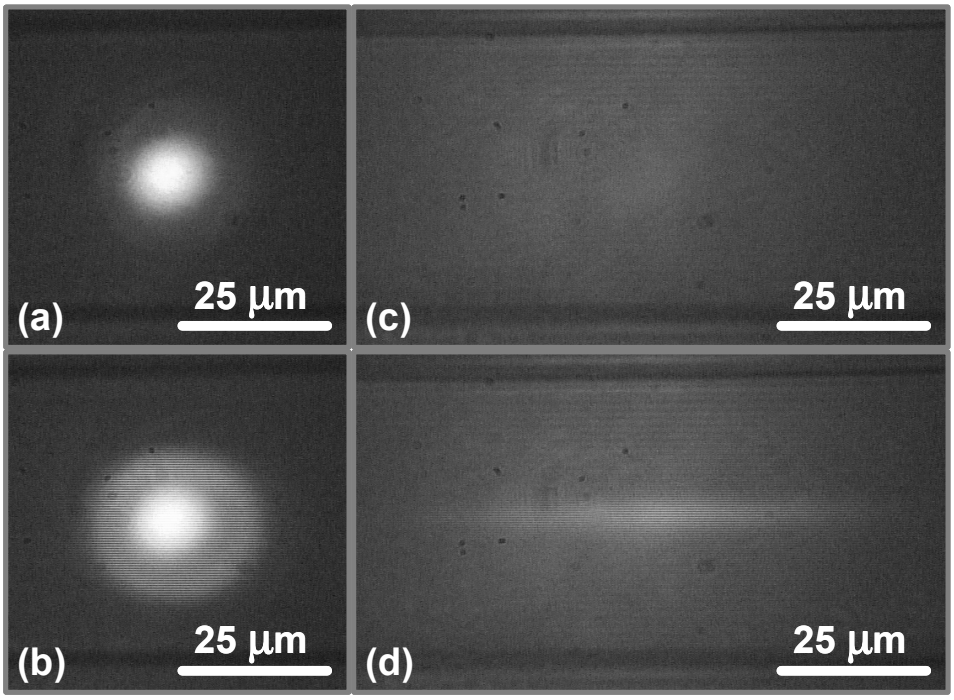

Figure 4-6 *Images of 5 μm beads flow taken by CCD camera with long pass emission filter. (A) and (B) are images of background and a bead with focused laser illumination. The laser spot in (A) shows the position of the focused laser spot. (C) and (D) are images of background and a bead with diffused laser illumination. (D) shows the trace of the bead.*

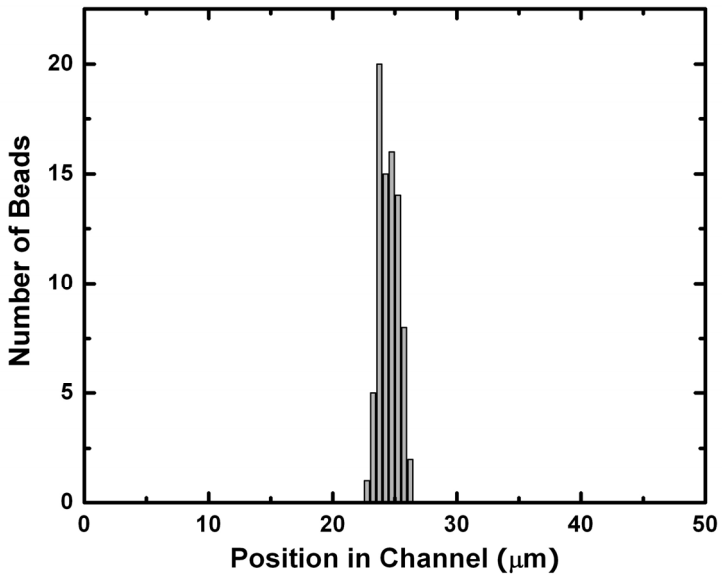

Figure 4-7 *Histogram of centroids of bead images from CCD camera*

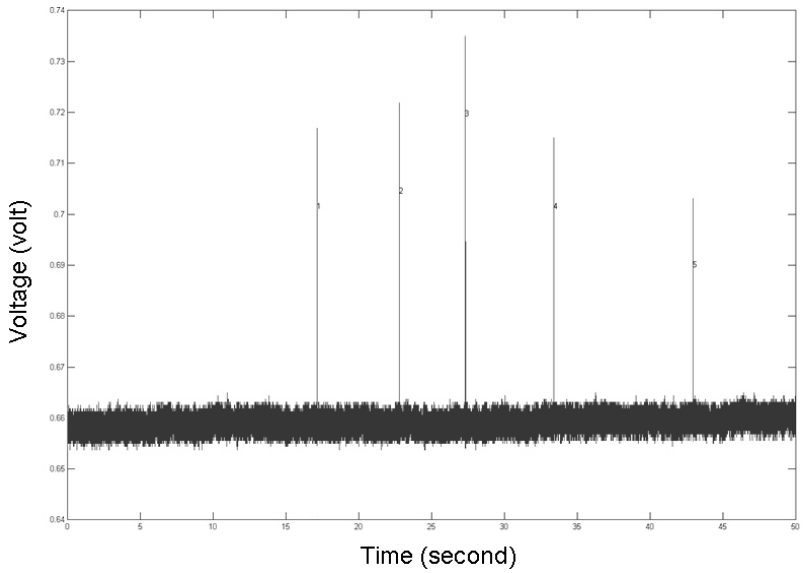

Figure 4-8 *5 μm fluorescent beads detection with photodiode detector with long pass emission filter*

4.6 Testing with undiluted whole blood

To prepare the sample, 1 μl 1 mg/mL acridine orange stock solution was added to 100 μl whole human blood. 10x PBS diluted to 1x with Ficoll Phage Plus was used as a sheath flow solution. When the analog CCD camera was used for video recording, a 3 nL/min sample flow rate and 30 nL/min sheath flow rate were used to match the camera frame rate. For photodiode detection, a 0.1 μL/min sample flow rate and 1 μL/min sheath flow rate were used. The detector was set for low sensitivity mode to decrease its response time. Up to 1 μL/min sample flow and 10 μL/min sheath flow could be used with the PMT detector.

Fig. 4-9 shows images extracted from video taken by the CCD camera. The signal from an acridine-orange-stained leukocyte was not as strong as that from 5 μm

fluorescent beads, but the low flow rate gave the CCD camera enough integration time so that the signal generated by a passing cell could be identified.

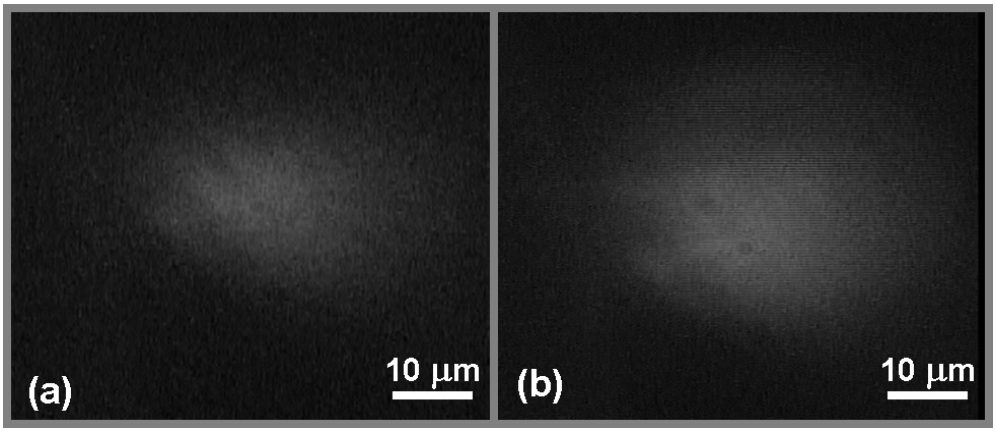

Figure 4-9 *Images extracted from video taken by CCD camera with long pass emission filter. (a) background image showing focused laser beam. (b) signal from a leukocyte.*

For photodiode detection, the expected leukocyte detection rate would be, on average, 4–11 cells per second for a normal individual. Both green and red emission filter was used. Fig.4-10 is a time trace over 50 seconds of an undiluted blood sample stained with acridine orange using a green emission filter. The results from testing on two blood samples were summarized in table I. Manual count by hemacytometer was repeated at least five times with 10:1 diluted samples. The standard deviations only include data variation but do not account for dilution which was normally in the 10–15% range. Each device count was calculated for 50 seconds. Counting was repeated with the same sample loading. Sample one was counted three times and sample two was counted eleven times. With the PMT detector, a throughput of up to about 100 leukocytes per second was achieved.

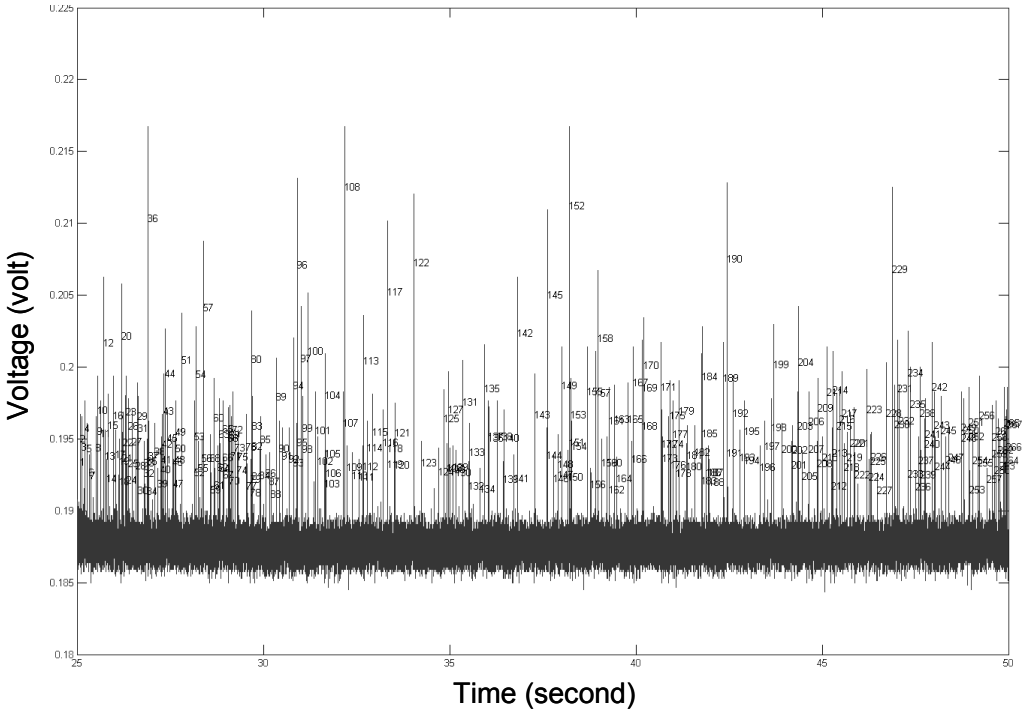

Figure 4-10 *Time trace of amplified photodiode signal of acridine orange stained undiluted whole blood with green emission filter centered at 525 nm. Peaks are labeled.*

For our device count, blood cell sedimentation contributed greatly to the counting error. For whole blood inside a test tube, sedimentation is normally complete in an hour. During testing, after we loaded the device with sample, fine alignment of the optical system was required. Normally we finished this process in ten minutes. Also it took five to ten minutes for the syringe pumps and the fluidic system to form steady hydrodynamically focused flow. On the other hand, the diameters of the syringe needle and tubing for connection were less than 1 mm, so the sedimentation distance for leukocytes was very small. The counts we got normally varied with time. The large count deviation in sample two was partly because the time duration to take eleven counts was about thirty minutes. For this reason, it is beneficial to increase the flow rate so that each count can be completed in a shorter time.

Maximal signal intensity was studied by plotting its histogram. Fig. 4-11 shows the results with 525 nm emission filter. One peak was identified. According to a previous study [56], the lower-intensity portion is contributed mainly by lymphocytes, while the higher-intensity portion is from monocytes. The center region is mostly granulocytes. Fig. 4-12 was the result from the 650 nm emission filter. Two peaks were identified, which agreed well with previous study. The peak at lower intensity is dominated by lymphocytes and the higher-intensity peak is mostly monocytes and granulocytes. The time between start of staining to photodiode recording in our testing was normally longer than fifteen minutes, so the samples were not fresh enough to demonstrate a separate monocyte peak in the 650 nm histogram [55, 56].

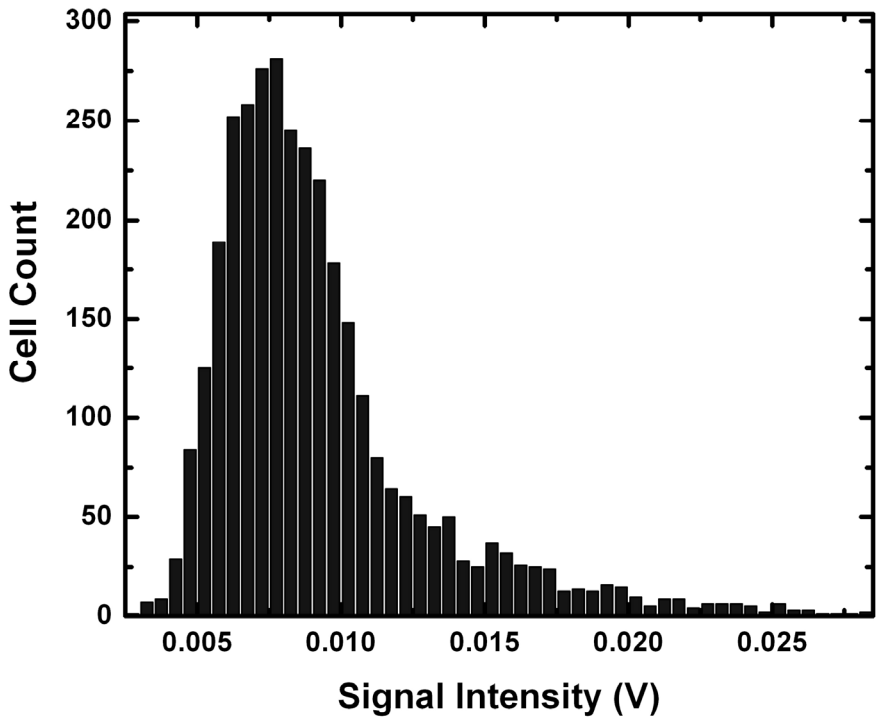

Figure 4-11 *Histogram of signal intensity from photodiode detector with green emission filter centered at 525 nm*

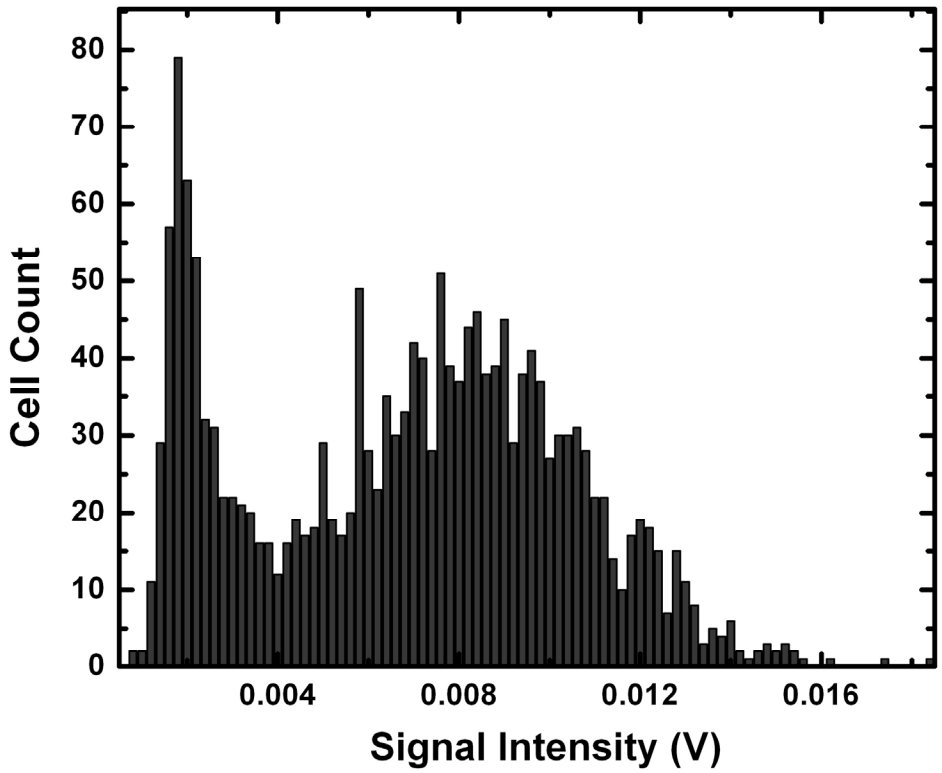

Figure 4-12 *Histogram of signal intensity from photodiode detector with red emission filter centered at 650 nm*

In our testing, the maximal throughput was about a hundred leukocytes per second with the PMT detector. Under the maximal throughput, the total time for counting a minimum of 200 leukocytes was a couple of seconds, which is adequate for our application. The overall system throughput is limited by several factors. First, sample dilution lowers the throughput by increasing total sample volume. In our study, undiluted blood was used. In this way minimal sample volume was used for sensing a certain target number of leukocytes. Secondly, sample throughput is proportional to volume flow rate, but is limited by the maximal pumping rate and response time of the sensing system. In our testing, a 3 nL/min core flow rate was used with CCD camera detection. This is the highest flow rate for optimal signal-to-noise ratio of the analog CCD camera,

because, under this flow rate, a typical leukocyte traveled through the detection zone in 30 milliseconds, which roughly equals the CCD frame acquisition time. A 100 nL/min sample flow rate was used for photodiode detection and 1 μL/min for that of the PMT. These were roughly the highest flow rates we could use for the detection without signal distortion. Under these flow rates, a typical leukocyte flowed by the detection zone in about 1 ms in photodiode detection and 0.1 ms for PMT detection. The time response of the photodiode receiver module under low sensitivity setting was 0.16 ms and that under high sensitivity was 0.6 ms. The time response of the PMT was 16 μs. In our system, these were the limiting factors for higher throughput. By using a detection system with faster time response, it is possible to increase the flow rates and thus the throughput by orders of magnitude. Thirdly, the cross-section area of the core flow in the detection zone is also related to throughput. Given the same volume flow rate, decreasing this area increases the linear flow velocity of the core flow. This requires a faster sensing system, but can reduce coincidence effect by increasing the average distance between cells in the detection zone.

4.7 Conclusion and on-going work

A microfluidic device was fabricated and a LIF-based flow cytometer system was demonstrated for leukocyte counting and differentiation from undiluted whole human blood. Leukocytes were selectively stained with fluorescent dye acridine orange with the optimal final concentration of 10 μg/mL. A Green fluorescent channel centered at 525 nm was used for leukocyte counting, and a red fluorescent channel centered at 650 nm was used for leukocyte differentiation. Maximal throughput of 100 leukocytes per second was achieved. The photobleaching time constant of acridine orange in the current

detection system was measured to be in the seconds range. Leukocyte counting and differential from undiluted blood was enabled by labeling leukocytes specifically and by the microfluidic implementation. Handling blood samples without dilution not only greatly reduced sample/waste volume and processing time, but also eliminated on-chip mixing and buffer storage completely. These advantages are especially attractive for point-of-care devices.

After the successful demonstration of the WBC differential on the optical bench, a detection system based on a modified fluorescent microscope was built at the collaborators' site (Fig. 4-13). High-illumination LED was used for excitation and a minipump was successfully used to manipulate the sample in suction mode. Fluorescent signals from green and red channels were able to be detected simultaneously with two PMTs. A handheld instrument based on the technology discussed in this chapter is under development by Iris International, Inc. (Fig. 4-14).

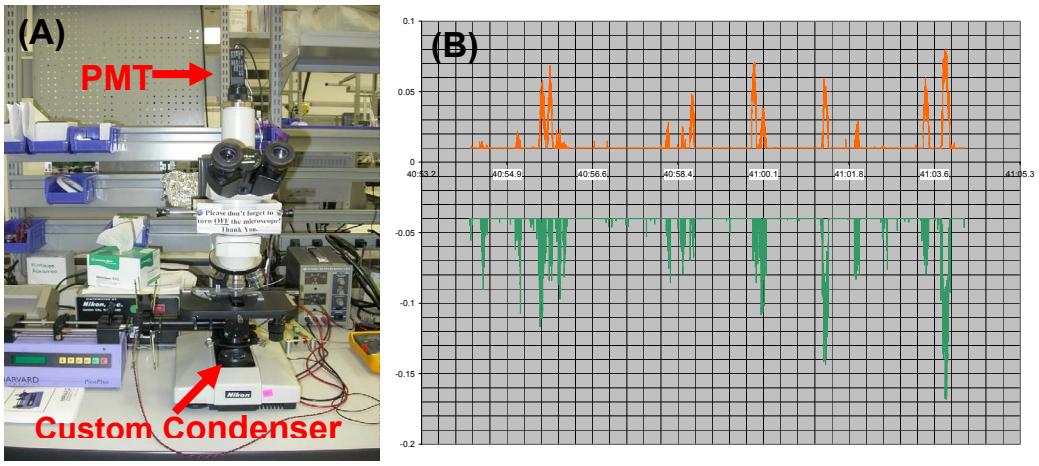

Figure 4-13 *(A) System based on modified microscope. (Courtesy Iris International, Inc.) (B) Detection by red (top) and green (bottom) fluorescence channel simultaneously.*

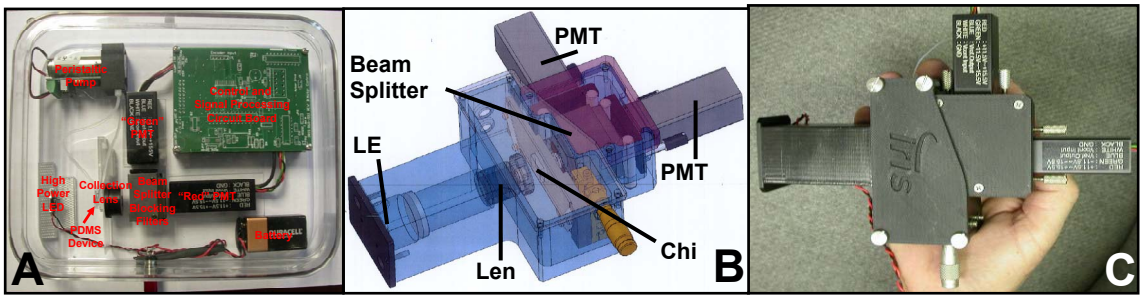

Figure 4-14 *A handheld instrument under development. (Courtesy Iris International, Inc.) (A) Mockup box showing individual components. (B) Mechanical design of the detection box. (C) Assembled detection box.*

4.8 Bibliography

[1] S. B. McKenzie, *Clinical Laboratory Hematology*. Prentice Hall, 2004.

[2] B. Houwen, "The Differential Cell Count," *Laboratory Hematology*, vol. 7, pp. 89–100, 2001.

[3] P. Ehrlich, "Methodologische beitrage zur physiologie und pathologie der versciedenen formen der leukocyten," *Zeitschrift fur Klinische Medizin*, vol. 1, pp. 553–560, 1879.

[4] W. H. Walton, "Automatic Counting Of Microscopic Particles," *Nature*, vol. 169, pp. 518–520, 1952.

[5] B. Swolin, P. Simonsson, S. Backman, I. Lofqvist, I. Bredin, and M. Johnsson, "Differential counting of blood leukocytes using automated microscopy and a decision support system based on artificial neural networks—evaluation of DiffMaster Octavia," *Clinical and Laboratory Haematology*, vol. 25, 139, 2003.

[6] J. M. S. Prewitt and M. Mendelso, "Analysis Of Cell Images," *Annals Of The New York Academy Of Sciences*, vol. 128, pp. 1035ff., 1966.

[7] M. L. Ingram and K. J. Preston, "Automated analysis of blood cells," *Scientific American*, vol. 128, pp. 1035–1053, 1970.

[8] H. M. Shapiro and N. G. Perlmutter, "Personal cytometers: Slow flow or no flow?" *Cytometry Part A*, vol. 69A, pp. 620–630, 2006.

[9] H. M. Shapiro, ""Cellular astronomy"—A foreseeable future in cytometry," *Cytometry Part A*, vol. 60A, pp. 115–124, 2004.

[10] K. Fujimoto, "Principles of Measurement in Hematology Analyzers Manufactured by Sysmex Corporation," *Sysmex Journal International*, vol. 9, 1999.

[11] N. Hughesjo, I. Norley, J. M. S. Young, and J. M. England, "Differential White Cell Counts By Frequency Distribution Analysis Of Cell Volumes," *Journal Of Clinical Pathology*, vol. 27, pp. 623–625, 1974.

[12] T. E. Oberjat, R. M. Zucker, and B. Cassen, "Rapid And Reliable Differential Counts On Dilute Leukocyte Suspensions," *Journal Of Laboratory And Clinical Medicine*, vol. 76, pp. 518ff., 1970.

[13] M. A. Vandilla, M. J. Fulwyler, and I. U. Boone, "Volume Distribution And Separation Of Normal Human Leucocytes," *Proceedings Of The Society For Experimental Biology And Medicine*, vol. 125, pp. 367ff., 1967.

[14] H. Maeda, N. Tatsumi, and A. Furota, "Clinical application of differential leukocyte volume distribution analysis," *Clinical Pathology*, vol. 27, pp. 1117–1200, 1979.

[15] H. Maeda and N. Tatsumi, "Clinical application of differential leukocyte volume distribution analysis (2)," *Clinical Pathology*, vol. 9, pp. 555–558, 1982.

[16] N. Tatsumi, I. Tsuda, A. Furota, and T. Takubo, "Principle of Blood Cell Counter—Development of Electric Impedance Method," *Sysmex Journal International*, vol. 9, pp. 8–20, 1999.

[17] L. Ornstein and H. R. Ansley, "Spectral Matching Of Classical Cytochemistry To Automated Cytology," *Journal Of Histochemistry & Cytochemistry*, vol. 22, pp. 453ff., 1974.

[18] S. Gawad, L. Schild, and P. Renaud, "Micromachined impedance spectroscopy flow cytometer for cell analysis and particle sizing," *Lab On A Chip*, vol. 1, 76, 2001.

[19] D. W. Lee, S. Yi, and Y.-H. Cho, "A flow-rate independent cell counter using fixed control volume between double electrical sensing zones," *presented at 18th IEEE International Conference on Micro Electro Mechanical Systems (MEMS 2005)*, Miami Beach, Florida, USA, 2005.

[20] D. Satake, H. Ebi, N. Oku, K. Matsuda, H. Takao, M. Ashiki, and M. Ishida, "A sensor for blood cell counter using MEMS technology," *Sensors and actuators. B, Chemical*, vol. 83, 77, 2002.

[21] H. Morgan, D. Holmes, and N. G. Green, "High speed simultaneous single particle impedance and fluorescence analysis on a chip," *Current Applied Physics*, vol. 6, pp. 367–370, 2006.

[22] G. B. Lee, C. H. Lin, and S. C. Chang, "Micromachine-based multi-channel flow cytometers for cell/particle counting and sorting," *Journal Of Micromechanics And Microengineering*, vol. 15, pp. 447–454, 2005.

[23] E. Altendorf, D. Zebert, M. Holl, and P. Yager, "Differential blood cell counts obtained using a microchannel based flow cytometer," *presented at International Conference on Solid State Sensors and Actuators (TRANSDUCERS '97)*, Chicago, U.S.A., 1997.

[24] D. Holmes, H. Morgan, and N. G. Green, "High throughput particle analysis: Combining dielectrophoretic particle focussing with confocal optical detection," *Biosensors & Bioelectronics*, vol. 21, pp. 1621–1630, 2006.

[25] S. Y. Yang, S. K. Hsiung, Y. C. Hung, C. M. Chang, T. L. Liao, and G. B. Lee, "A cell counting/sorting system incorporated with a microfabricated flow cytometer chip," *Measurement Science & Technology*, vol. 17, pp. 2001–2009, 2006.

[26] C. Simonnet and A. Groisman, "High-throughput and high-resolution flow cytometry in molded microfluidic devices," *Analytical Chemistry*, vol. 78, pp. 5653–5663, 2006.

[27] S. Niehren, W. Kinzelbach, S. Seeger, and J. Wolfrum, "An All-Solid-State Flow Cytometer For Counting Fluorescent Microspheres," *Analytical Chemistry*, vol. 67, pp. 2666–2671, 1995.

[28] M. A. Vandilla, T. T. Trujillo, P. F. Mullaney, and J. R. Coulter, "Cell Microfluorometry—A Method For Rapid Fluorescence Measurement," *Science*, vol. 163, pp. 1213ff., 1969.

[29] W. Dittrich and W. Gohde, "Impulsfluorometrie bei Einzelzellen in Suspensionen," *Z. Naturforsch*, vol. 24b, 360, 1969.

[30] D. Huh, W. Gu, Y. Kamotani, J. B. Grotberg, and S. Takayama, "Microfluidics for flow cytometric analysis of cells and particles," *Physiological Measurement*, vol. 26, pp. R73–R98, 2005.

[31] L.-K. Chau, T. Osborn, C.-C. Wu, and P. Yager, "Microfabricated silicon flow-cell for optical monitoring of biological fluids," *Analytical Sciences.*, vol. 15, pp. 721–724, 1999.

[32] M. A. McClain, C. T. Culbertson, S. C. Jacobson, and J. M. Ramsey, "Flowcytometry of Escherichia coli on microfluidic devices," *Analytical Chemistry*, pp. 5334–5338, 2001.

[33] R. Miyake, H. Ohki, I. Yamazaki, and T. Takagi, "Investigation of sheath flow chambers for flow cytometers (micro machined flow chamber with low pressure loss)," *JSME International Journal B*, vol. 40, pp. 106–113, 1997.

[34] A. Wolff, I. R. Perch-Nielsen, U. D. Larsen, P. Friis, G. Goranovic, C. R. Poulsen, J. P. Kutter, and P. Telleman, "Integrating advanced functionality in a microfabricated high-throughput fluorescent-activated cell sorter," *Lab On A Chip*, vol. 3, pp. 22─27, 2003.

[35] D. Sobek, A. M. Young, M. L. Gray, and S. D. Senturia, "Microfabricated fused silica flow chambers for flow cytometry," *Proceedings of IEEE*, vol. 2, 1993.

[36] H. W. Bang, H. Y. Yun, W. G. Lee, J. Park, J. Lee, S. Chung, K. Cho, C. Chung, D. C. Han, and J. K. Chang, "Expansion channel for microchip flow cytometers," *Lab On A Chip*, vol. 6, pp. 1381─1383, 2006.

[37] G.-B. Lee, C.-H. Lin, and G.-L. Chang, "Micro flow cytometers with buried SU-8/SOG optical waveguides," *Sensors Actuator A*, vol. 103, pp. 165–170, 2003.

[38] K. Cheung, S. Gawad, and P. Renaud, "Impedance spectroscopy flow cytometry: On-chip label-free cell differentiation," *Cytometry Part A*, vol. 65A, pp. 124─132, 2005.

[39] B. H. Weigl, R. Bardell, T. Schulte, F. Battrell, and J. Hayenga, "Design and rapid prototyping of thin-film laminate-based microfluidic devices," *Biomedical Microdevices*, vol. 3, pp. 267─274, 2001.

[40] S. Chung, S. J. Park, J. K. Kim, C. Chung, D. C. Han, and J. K. Chang, "Plastic microchip flow cytometer based on 2- and 3-dimensional hydrodynamic flow focusing," *Microsystem Technology.*, vol. 9, pp. 525–533, 2003.

[41] D. Huh, Y.-C. Tung, H.-H. Wei, J. B. Grotberg, S. J. Skerlos, K. Kurabayashi, and S. Takayama, "Use of air-liquid two-phase flow in hydrophobic microfluidic channels for disposable flow cytometers," *Biomedical Microdevices*, vol. 4, pp. 141–149, 2002.

[42] Y.-C. Tung, M. Zhang, C.-T. Lin, K. Kurabayashi, and S. J. Skerlos, "PDMS-based opto-fluidic micro flow cytometer with two-color, multi-angle fluorescence detection capability using PIN photodiodes," *Sensors Actuators B*, vol. 98, 2004.

[43] A. Y. Fu, H. P. Chou, C. Spence, F. H. Arnold, and S. R. Quake, "An integrated microfabricated cell sorter," *Analytical Chemistry*, vol. 74, pp. 2451─2457, 2002.

[44] A. Y. Fu, C. Spence, A. Scherer, F. H. Arnold, and S. R. Quake, "A microfabricated fluorescence-activated cell sorter," *Nature Biotechnology*, vol. 17, pp. 1109─1111, 1999.

[45] E. Cabuz, J. Schwichtenberg, B. DeMers, and E. Satren, "Padmanabhan A and Cabuz C 2002 MEMS-based flow controller for flow cytometry," *Proceedings of Hilton Head 2002: Solid-State Sensor, Actuator and Microsystems Workshop*, pp. 110–111, 2002.

[46] S. D. H. Chan, G. Luedke, M. Valer, C. Buhlmann, and T. Preckel, "Cytometric analysis of protein expression and apoptosis in human primary cells with a novel microfluidic chip-based system," *Cytometry A*, vol. 55, pp. 119–25, 2003.

[47] H. L. Sheenan and G. W. Storey, "An improved method of staining leukocyte granules with Sudan Black B," *Journal of Pathology and Bacteriology*, vol. 59, 336, 1947.

[48] L. Kass, "Staining of granulocyte cells by Chlorazol Black E. American," *Journal of Clinical Pathology*, vol. 76, pp. 810─812, 1981.

[49] W. Kosenow, "Die Fluorochromierung mit Acridinorange, eine Methode zur Lebendeobachtung gefarbter Blutzellen," *Acta Haemat*, vol. 7, pp. 217, 1952.

[50] L. M. Schiffer, "Fluorescence microscopy with acridine orange: a study of hemopoietic cells in fixed preparations," *Blood*, vol. 19, 200, 1962.

[51] J. F. Jackson, "Supravital Blood Studies, Using Acridine Orange Fluorescence," *Blood*, vol. 17, pp. 643ff., 1961.

[52] L. Hallermann, R. Thom, and H. Gerhartz, "Elektronische differentialzahlung von granulocyten und lymphocyten nach intravitaler fluochromierung mit acridinorange," *Verh Deutsch Ges Inn Med*, vol. 70, 217, 1964.

[53] H. M. Shapiro, *Practical flow cytometry*, *4th ed.* Hoboken, New Jersey: John Wiley & Sons, Inc., 2003.

[54] L. R. Adams and L. A. Kamentsky, "Machine Characterization Of Human Leukocytes By Acridine Orange Fluorescence," *Acta Cytologica*, vol. 15, pp. 289ff., 1971.

[55] L. R. Adams and L. A. Kamentsky, "Fluorometric Characterization Of 6 Classes Of Human Leukocytes," *Acta Cytologica*, vol. 18, pp. 389─391, 1974.

[56] J. Steinkam, A. Romero, and M. A. Vandilla, "Multiparameter Cell Sorting - Identification Of Human Leukocytes By Acridine-Orange Fluorescence," *Acta Cytologica*, vol. 17, pp. 113–117, 1973.

[57] H. M. Shapiro, E. R. Schildkraut, R. Curbelo, C. W. Laird, R. B. Turner, and T. Hirschfeld, "Combined Blood-Cell Counting And Classification With Fluorochrome Stains And Flow Instrumentation," *Journal Of Histochemistry & Cytochemistry*, vol. 24, pp. 396–411, 1976.

[58] H. M. Shapiro, E. R. Schildkraut, R. Curbelo, R. B. Turner, R. H. Webb, D. C. Brown, and M. J. Block, "Cytomat-R—Computer-Controlled Multiple Laser Source Multiparameter Flow Cytophotometer System," *Journal Of Histochemistry & Cytochemistry*, vol. 25, pp. 836–844, 1977.

[59] I. Giannini and V. Baroncelli, "Composition Suitable for Testing Biological Tissure and/or Liquids, and the Method of Use," in *US Patent 4376820*, 1983.

[60] S. J. Kirchanski and K. Wardwell, "Method for Quantitating and Differentiating White Blood Cells," in *U S Patent 4882284*, 1989.

[61] A. G. J. Tibbe, B. G. de Grooth, J. Greve, P. A. Liberti, G. J. Dolan, and L. Terstappen, "Optical tracking and detection of immunomagnetically selected and aligned cells," *Nature Biotechnology*, vol. 17, pp. 1210–1213, 1999.

[62] L. Kass, "Metachromatic Dye Sorption Means for Differential Determination of Leukocytes," in *US Patent 4400370*, 1983.

[63] L. Kass, "Identification Of Lymphocyte Subpopulations With A Polymethine Dye," *Journal Of Histochemistry & Cytochemistry*, vol. 36, pp. 711–715, 1988.

[64] L. K. Lebeck, L. Chang, W. Chen, L. Clement, R. Hagbloom, B. Hull, B. J. Mast, N. Stewart, and B. Houwen, "White blood cell five-part subpopulation estimations: A flow cytometric based reference method.," *Sysmex Journal International*, vol. 5, pp. 77–84, 1995.

[65] L. K. Lebeck, B. J. Mast, and B. Houwen, "Flow cytometric white blooddifferentials: A proposed alternate reference method.," *Sysmex Journal International*, vol. 3, pp. 61–69, 1993.

[66] W. Goossens, L. Vanhove, and R. L. Verwilghen, "Monocyte Counting—Discrepancies In Results Obtained With Different Automated Instruments," *Journal Of Clinical Pathology*, vol. 44, pp. 224–227, 1991.

[67] W. Hubl, S. Andert, A. Erath, A. Lapin, and P. M. Bayer, "Peripheral-Blood Monocyte Counting - Towards A New Reference Method," *European Journal Of Clinical Chemistry And Clinical Biochemistry*, vol. 33, pp. 839–845, 1995.

[68] W. Hubl, S. Andert, A. Erath, J. Streicher, and P. M. Bayer, "Evaluation of automated basophil counting by using fluorescence-labelled monoclonal antibodies," *Journal Of Clinical Laboratory Analysis*, vol. 10, pp. 177–183, 1996.

[69] W. Hubl, L. Tlustos, A. Erath, S. Andert, and P. M. Bayer, "Proposed reference method for peripheral-blood monocyte counting using fluorescence-labelled monoclonal antibodies," *Cytometry*, vol. 26, pp. 69–74, 1996.

[70] W. Hubl, G. Wolfbauer, S. Andert, G. Thum, J. Streicher, C. Hubner, A. Lapin, and P. M. Bayer, "Toward a new reference method, for the leukocyte five-part differential," *Cytometry*, vol. 30, pp. 72–84, 1997.

[71] L. Terstappen, D. Johnson, R. A. Mickaels, J. Chen, G. Olds, J. T. Hawkins, M. R. Loken, and J. Levin, "Multidimensional Flow Cytometric Blood-Cell Differentiation Without Erythrocyte Lysis," *Blood Cells*, vol. 17, pp. 585─602, 1991.

[72] S. Serke and D. Huhn, "An all leukocyte whole blood lyse method for multiparameter flow-cytometry," *Clinic Laboratory Haematology*, vol. 15, pp. 275–285, 1993.

[73] J. K. Lanyi and J. Lederber, "Fluorescent Method For Detection Of Excreted Ribonuclease Around Bacterial Colonies," *Journal Of Bacteriology*, vol. 92, pp. 1469ff., 1966.

[74] Y. Kubota and R. F. Steiner, "Fluorescence Decay And Quantum Yield Characteristics Of Acridine-Orange And Proflavine Bound To DNA," *Biophysical Chemistry*, vol. 6, pp. 279─289, 1977.

[75] Y. Moriyama, T. Takano, and S. Ohkuma, "Acridine-Orange As A Fluorescent-Probe For Lysosomal Proton Pump," *Journal Of Biochemistry*, vol. 92, pp. 1333─1336, 1982.

[76] R. A. Levine, S. C. Wardlaw, and C. L. Patton, "Detection Of Hematoparasites Using Quantitative Buffy Coat Analysis Tubes," *Parasitology Today*, vol. 5, pp. 132─134, 1989.

[77] S. R. Quake and A. Scherer, "From micro- to nanofabrication with soft materials," *Science*, vol. 290, pp. 1536─1540, 2000.

[78] A. Hammouda and A. Fakeir, "Flow Cytometric Evaluation Of Erythrocyte Response To Oxidant Stress," *Cytometry*, vol. 20, pp. 19─22, 1995.

[79] "Autofluorescence: Causes and Cures," in *www.uhnresearch.ca/facilities/wcif/PDF/Autofluorescence.pdf*.

[80] J. Hofmann, U. Till, B. Hofmann, E. Michel, and M. Quiess, "Use Of Acridine-Orange For Testing Blood-Platelet Integrity," *Acta Biologica Et Medica Germanica*, vol. 38, pp. 1149─1157, 1979.

[81] P. L. McNeil and R. A. Steinhardt, "Plasma membrane disruption: Repair, prevention, adaptation," *Annual Review Of Cell And Developmental Biology*, vol. 19, pp. 697─731, 2003.

CHAPTER 5

CONCLUSIONS

Blood count is the cornerstone of the modern hematology laboratory. Since the discovery of blood composition in the 1850s, it has become one of the most common laboratory tests performed today. The methods for blood count are driven by technology advance. Manual count was the only method available before the mid-1950s and is still in use, especially in developing countries. It has been replaced gradually during the past fifty years by automated blood analyzers, which are faster and more accurate. I believe the next big technological development in blood count will be point-of-care on-chip blood counters, which provide reliable and accurate information even more quickly and cheaply. Such devices can find wide applications in the era of personalized healthcare and medicine.

To demonstrate feasibility and make working prototypes, this thesis aims to explore state-of-the-art microfabrication technologies for making centimeter-size chips with tens-of-micron-size features that can perform blood counts. Three separate have angles been taken. First, two types of micro devices for highly efficient erythrocyte and leukocyte separation are demonstrated. Both the pillar-shaped and the channel-shaped devices separate particles of different sizes based on hydrodynamic separation. Engineering streamline designs inside microdevices are proved to be effective in controlling the critical particle size and the separation profile. The benefits of the channel-shaped devices include continuous and passive separation, small footprint, and fewer requirements on flow control. The second effort was made on erythrocyte and leukocyte count by electrical impedance sensing. Sensitivity improvement of the micro impedance sensors is enabled by solving the small double-layer capacitance problem inherent to this type of device. Platinum black electroplating on electrodes is effective in sensing at low frequency (less than 1MHz). Inductor-induced resonance sensing includes a parallel inductor to nullify system capacitive components at resonance frequency, allowing the optimal sensing frequency to be chosen by the inductance value. The third major contribution of this thesis is the demonstration of a fluorescence-sensing method in a micro flow cytometer format for leukocyte differentials with undiluted blood samples. Acridine orange was chosen as the differential fluorescence dye because of its well-known property as a nucleic acid stain and its differential effects for leukocytes. The most important feature of the method is that it does not require any sample dilution, which differs from conventional automated blood analyzers and makes this approach especially appealing for current microdomain implementation. The reduction of the

coincidence effect is made possible because of minimal interference from the unstained erythrocytes, and by reducing the dimension of the sensing zone with microfabrication.

The successful demonstrations of the devices presented in this thesis enable further investigation into on-chip blood analysis. The separation devices can be optimized to separate blood cells for a wider size range. In this way, for example, platelets can be separated from the erythrocytes and counted separately. In this way, blood cell aggregation and adhesion to device surfaces might be reduced. Also the separation devices can be integrated with electrical impedance sensors, so that the geometric design of the sensing zones can be optimized for particles of different sizes to improve sensitivity. Instead of coplanar electrodes, parallel overlap ones in impedance sensors will improve the scattering caused by particles flowing at different heights inside the channel. Another solution is to use hydrodynamic focusing with sheath flow having different dielectric properties from the cells. For leukocyte differential by fluorescence sensing, 3-part and even 5-part differentials are possible with acridine orange. But to achieve that, full automation is required for reliable results because the staining process itself is time critical and manual sample preparation introduces too many variables. Other cytochemical, fluorescent dyes or labeled antibodies can be explored for better staining performance. The throughput can be improved by at least one to two orders of magnitude by designing a transimpedance amplifier with wider bandwidth for optical detectors. Overall system integration with sample preparation, volume measurement, and fluidic, electrical and optical coupling is another challenge — a common problem that needs to be solved in the whole microfluidics field.

Blood delivers oxygen and nutrients to, and transports metabolic intermediates and wastes from every individual cell in the human body, making it a treasure for disease diagnostics and patient health monitoring. The current parameters for blood count only provide the bulk picture. The under-represented cells inside the bloodstream — which are not included in blood count now — might provide much more significant diagnostic information and/or better treatment. For example, circulating tumor cells, hematopoietic stem cells, and nucleated erythrocytes are all not detectable by conventional blood analyzers either because their extreme low numbers are not statistically significant or because there is no reliable, efficient, and cost-effective way to detect them. Not even mentioned is the promising and challenging field of low abundant plasma protein detection. Over 95% of plasma proteins are at concentrations under the detection limits of the current best immunoassays and they are believed to have extremely high medical values. The technological development of hematology will greatly benefit human health but there is still much to be done. Micro and nano technologies provide a unique opportunity, and on-chip blood count is only the very beginning.